# POLITECNICO DI TORINO

**Master's Degree in Mechanical Engineering - Automation**

Academic year: 2022-2023

Graduation session: July 2023


**Master's Degree Thesis**

# Sizing and study of the regulation system of a mechanical actuator for secondary flight controls in a regional transport aircraft

**Supervisors**

**Prof. MASSIMO SORLI**

**Dr. ANDREA DE MARTIN**

**Dr. ROCCO GENTILE**

**Candidate**

**LORENZA GAETANA VACCARO**

In collaboration with Leonardo S.p.A

# Summary

In recent decades, the continuous evolution of flight control technologies has sparked a growing interest in implementing more electric systems within modern aircraft. This thesis aims to address the crucial issue of electromechanical actuation for secondary flight controls, with the goal of facilitating the transition towards a more electric aircraft configuration.

To provide a comprehensive understanding of the research area, the thesis begins by presenting a general context on flight control design and the ongoing developments in this field. The increasing demand for enhanced performance, efficiency, and reliability has driven the exploration of more electric aircraft concepts. Within this context, the utilization of electromechanical actuators has emerged as a promising avenue for achieving the desired objectives.

The thesis then focuses on examining the applicability and performance characteristics of electromechanical actuators. By analysing various parameters such as power requirements, response time, weight, and reliability, the potential advantages and limitations of electromechanical actuation systems are assessed. This analysis lays the foundation for defining an architecture suitable for the electromechanical actuation system. The research work presented in this thesis was developed in cooperation with Leonardo Labs, with the final purpose of producing a digital twin for a possible Electro-Mechanical actuation system of a fowler flap for a future regional transport aircraft.

In the specific case studied, the flight control surface considered is a fowler flap. The chosen architecture for the electromechanical actuation system involves the implementation of two parallel actuators. This redundant configuration enhances safety and provides fault tolerance, ensuring continued control functionality even in the event of a single actuator failure.

Dimensioning the key components of the electromechanical actuation system is a crucial step towards ensuring optimal performance. By taking into account factors such as actuator size, power supply, and control strategies, a preliminary sizing process is carried out. This process involves evaluating the actuator's ability to meet the required load and displacement demands under different operating conditions.

To gain further insights into the system's behaviour, extensive analyses are conducted under diverse operational scenarios. The effects of temperature variations on the actuator's performance are examined, along with the implications of a fault occurring in one of the parallel actuators. Additionally, considerations are made for the system's startup and shutdown conditions to guarantee its safety and reliability.

In designing the control system, the focus is on determining appropriate gain values for the various control loops in the linear regime. By considering stability requirements and performance objectives, approximate gain values are identified. Furthermore, stability margins are quantified to ensure a robust and stable control system.

To analyse the system's behaviour in a more realistic and complex environment, a high-fidelity model is developed using the Matlab-Simulink® simulation platform. This model incorporates equations available in the literature and enables an in-depth analysis of the system's response in nonlinear regimes. By leveraging this model, the dynamic behaviour of the electromechanical actuation system is evaluated across its entire operating range.

In conclusion, this thesis provides a comprehensive analysis of the electromechanical actuation for secondary flight controls in the context of more electric aircraft. By addressing key aspects such as system architecture, dimensioning, behaviour analysis, control system design, and validation, valuable insights are gained. The results obtained contribute to the ongoing efforts in designing more efficient, reliable, and sustainable flight control systems for future aircraft.

# Table of Contents

# List of Tables

# List of Figures

# Acronyms

**FCS**
Flight Control Systems

**PFCS**
Primary Flight Control Systems

**SFCS**
secondary Flight Control Systems

**FBW**
Fly By Wire

**PBW**
Power By Wire

**EHA**
Electro-Hydrostatic Actuator

**EMA**
Electro-Mechanical Actuator

**HSA**
Hydraulic Servo Actuator

**DC**
Direct Current

**AC**
Alternating Current

**BLDC**

Permanent magnet Brushless DC Motor

**PMSM**

Permanent Magnet Synchronous Motor or Permanent Magnet Brushless AC Motor.

**RVDT**

Rotary Variable Differential Transformer

**FOC**

Field Oriented Control

# Chapter 1

# Introduction

To offer a comprehensive understanding of the topic, the overall aims of flight controls and their function have been described, situated within the broader scope of aircraft flight mechanics.

## 1.1 Flight control system

It is customary when studying the mechanics and control of flight to make the assumption that an aircraft can be viewed as rigid body, described by a set of body axis coordinates as depicted in Figure 1. This rigid body has six independent movements known as degrees-of-freedom, consisting of three translations along the axes and three rotations around them. Specifically, by placing a coordinate system with Euclidean geometry at the aircraft's center of mass, three main axes of rotation can be identified:

- Longitudinal axis, running from the tail to the nose of the aircraft, with positive direction aligned with the flight path. Rotation around this axis is referred to as Roll.
- Vertical axis, originating from the center of gravity and perpendicular to the wings, pointing downwards. The rotation around this axis is known as Yaw.
- Lateral axis, extending from the pilot's left to right, parallel to the wings. The primary rotation around this axis is called Pitch.

The fundamental principles of flight control apply to all types of aircraft, regardless of their complexity or size. During the majority of a flight, an airplane typically travels in a straight, level path with its velocity vector aligned parallel to the earth's surface, following a heading determined by the pilot. If the pilot intends

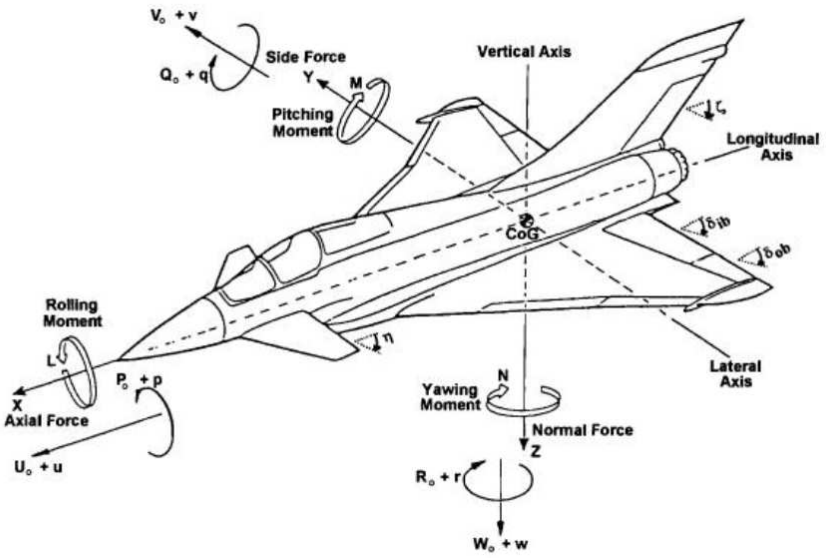


**Figure 1.1:** Body-axis aircraft coordinate system
[1]

to ascend, the flight control system must pivot the aircraft in a nose-up direction around the pitch axis to achieve the desired climb angle. Once the aircraft reaches the desired altitude, it will be maneuvered in a nose-down direction to return to level flight. In most fixed-wing aircraft, if the pilot wants to change the aircraft's direction, a turn must be executed to align it with the new heading. During a turn, the wings are rotated around the roll axis until a particular bank angle is achieved, and a rotation around the yaw axis results in a change of heading. The flight control system of the aircraft enables the pilot to have command over the aircraft during all phases of flight. The system comprises control surfaces that allow for movement in pitch, roll, and yaw. Additional control surfaces are required to regulate the high-lift devices necessary for approach and landing. Because of the immense aerodynamic forces on the flight control surfaces, the flight control system must provide significant physical assistance to the pilot. As a result, the aircraft controls need to have an "artificial feel" that provides the pilot with gradual and well-coordinated controls, making the aircraft safe and enjoyable to handle. [2]

### 1.1.1 Primary flight control system

The pilot controls the six degrees of freedom of the aircraft by manipulating the engine thrust and operating the primary flight control systems (PFCS). More specifically:

- **Pitch control**: To control the aircraft's inclination along the pitch axis, the primary flight control systems utilized are the horizontal stabilizer trimmer (for long-term regulation) and the elevators (for short-term regulation), both located on the horizontal tail.
- **Roll control**: The pilot commands the deflection of both ailerons, located at the wingtip of each wing, to control the aircraft's roll. The ailerons are deflected in opposite directions, with the downwards deflection increasing lift on the up-wing and the upward deflection decreasing lift on the down-wing. Additionally, the spoiler can also be slightly moved to reduce aileron deflection, improving the aircraft's maneuverability. At low airspeeds, the roll control provided by the ailerons is enhanced by differentially using the wing spoilers located on the upper surface of the wing.
- **Yaw control**: The rudder, located on the trailing edge of the vertical stabilizer, is used to control rotations along the vertical axis. Similar to the elevator and ailerons, the rudder is powered by the flight control system. In civil airliners, these controls are connected to the aircraft's yaw dampers, which help to dampen any uncomfortable oscillations known as "Dutch roll" that can occur during flight. These oscillations can be particularly unpleasant for passengers, especially those seated at the rear of the aircraft.

### 1.1.2 Secondary flight control system

Secondary Flight Control Systems (SFCS), together with the PFCS, improves the performance characteristics of an aircraft or relieves the pilot of using excessive control force. Typically, they are intermittently used during the phases of take off, approaching and landing to optimize the aerodynamic configuration and flight characteristics of the aircraft. The high lift system on an aircraft consists of flaperons and leading edge slats which work together to increase lift. During landing approach, the flaperons may be lowered to increase the wing's camber and improve aerodynamics. Leading edge slats are usually extended during takeoff to further increase wing camber and lift, but this may also result in increased drag. However, the high levels of thrust provided by the engines typically help to minimize this drawback.

Secondary flight control systems may consist of wing flaps, leading edge devices, spoilers, and trim systems:

- **Flaps:** Flaps represent the prevailing choice for high-lift mechanisms employed in airplanes. These structures are affixed to the rear edge of the wing and contribute to an augmentation of both lift and drag. The utilization of flaps enables a trade-off between elevated cruising velocities and reduced landing speeds, as they can be deployed as necessary and concealed within the wing's framework when not required. There are four common types of flaps: plain, split, slotted, and fowler flaps.

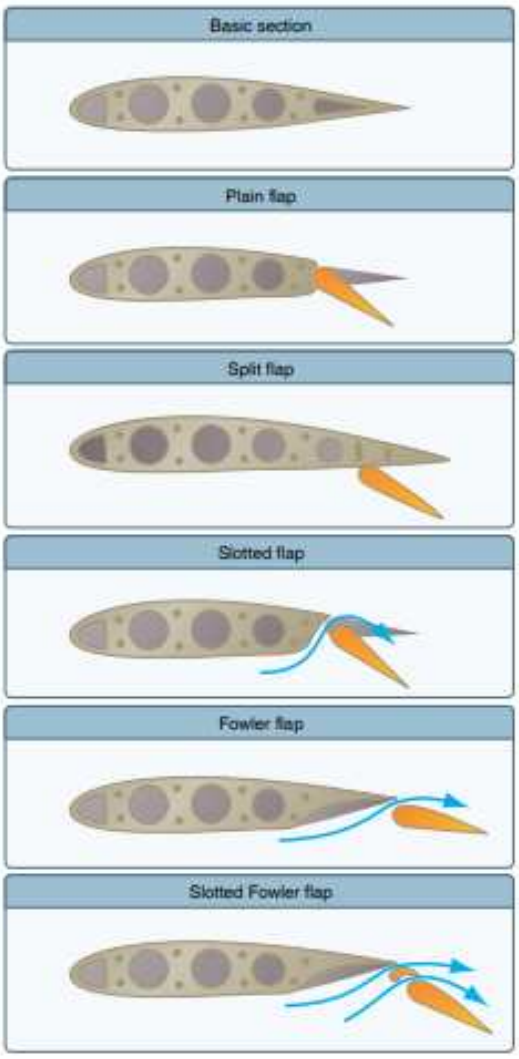


**Figure 1.2:** Five common types of flaps

  - **Plain:** The plain flap is the most basic among the four varieties. It enhances the curvature of the airfoil, leading to a noteworthy elevation in the coefficient of lift at a specific angle of attack. Simultaneously, it substantially amplifies drag and shifts the center of pressure towards the rear of the airfoil, consequently generating a pitching moment that causes the nose of the aircraft to tilt downwards.
  - **Split:** The split flap is deployed from the underside of the airfoil, resulting in a slightly larger lift augmentation compared to the plain flap. However, this configuration generates more drag due to the turbulent airflow pattern produced behind the airfoil. When fully extended, both plain and split flaps generate substantial drag while providing minimal additional lift.
  - **Slotted:** The slotted flap is currently the most widely used type of flap on aircraft. It is utilized in various forms for both small and large aircraft.In the case of small aircraft, the hinge is positioned beneath the lower surface of the flap. When the flap is lowered, a channel is formed between the flap well in the wing and the leading edge of the flap. As the slotted flap is lowered, high-energy air from the lower surface is directed towards the upper surface of the flap through the slot. The high-energy air flowing through the slot accelerates the boundary layer on the upper surface of the flap, postponing the separation of airflow and resulting in a higher lift coefficient. Consequently, the slotted flap yields much greater enhancements in the maximum lift coefficient compared to plain or split flaps. While there are various types of slotted flaps, large aircraft often incorporate double- or even triple-slotted flaps. These configurations allow for the maximum increase in drag without the airflow over the flaps separating and negating the lift they generate.
  - **fowler:** Fowler flaps are a specific type of slotted flap. Unlike other flap designs that primarily alter the wing's camber, Fowler flaps also increase the wing's surface area. Instead of pivoting downwards on a hinge, they slide backwards along tracks. During the initial phase of extension, Fowler flaps generate minimal drag but significantly enhance lift by increasing both the wing's area and camber. Pilots should be mindful that extending the flaps may induce a nose-up or nose-down pitching moment, depending on the aircraft type, necessitating compensation, often through trim adjustments. As the extension continues, the flaps deflect downward. In the final stage of their movement, the flaps predominantly increase drag without a substantial additional boost in lift.

- **Leading Edge Devices:** Leading-edge devices are basically designed to assist the flow in negotiating the sharp turn from the lower surface, around

the leading edge, and back for a short distance on the upper surface, without separating.

- **Spoilers:** Spoilers, which can be found on certain fixed-wing aircraft, are high-drag devices deployed from the wings with the purpose of disrupting the smooth airflow, thereby reducing lift and increasing drag. By deploying spoilers on both wings, the aircraft can descend without gaining excessive speed. Additionally, spoilers are used to assist in reducing the ground roll after landing. By diminishing lift, they transfer weight to the wheels, enhancing the effectiveness of braking.

- **Trim systems:** Trim systems are employed to alleviate the pilot's requirement of exerting constant pressure on the flight controls. These systems typically encompass flight deck controls and small hinged devices affixed to the trailing edge of one or more primary flight control surfaces. Aimed at reducing the pilot's workload, trim systems aerodynamically aid in the movement and positioning of the associated flight control surface. Various types of trim systems are commonly utilized, including trim tabs, balance tabs, antiservo tabs, ground adjustable tabs, and an adjustable stabilizer.

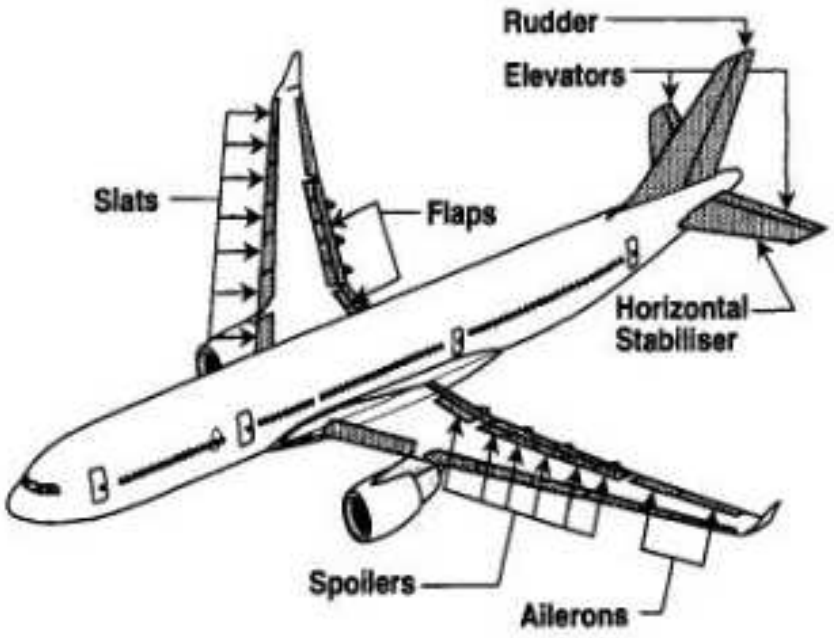


**Figure 1.3:** Example of flight control surfaces - Airbus 330.
[1]

## 1.2 The development of flight controls

The first generation of Flight Control Systems (FCSs) utilized mechanical components such as rods, levers, cables, and pulleys to create a direct link between the pilot's cockpit controls and the control surfaces that maneuver the aircraft. However, as airplanes grew in size and speed, the physical limitations of pilots meant that they could not exert enough force to move the control surfaces against the aerodynamic forces. This led to the development of the second generation of FCSs in the 1960s and early 1970s, which incorporated hydraulic boosters and actuators for flight-critical functions. The mechanical linkages between the pilot's controls and the hydraulic actuators were reduced to signaling only, with artificial feel becoming necessary to indicate the aircraft's speed. The introduction of hydraulically-powered control surfaces led to reduced aerodynamic drag and increased control-surface effectiveness, while also improving the aircraft's control surface flutter characteristics. Basic part-time stabilization functions such as yaw dampers were added to the FCS in response to flight dynamic effects.

Although mechanical links in aircraft flight control systems are simple and reliable, using electrical links involving computers can make signal processing easier. Electrical signaling enables the realization of highly sophisticated functions for improved safety and performance, which are calculated by the flight control computer. In the third generation of aircraft, analogue equipment was increasingly replaced with digital systems. While the transition from reversible to irreversible servo controls was completed, the links between the pilot inputs and the actuators were still mechanical for all flight-critical functions. However, electrical signaling gained importance and was introduced for less critical functions such as roll spoilers, trimming, and slat/flap control on the A310.

The first FCSs were mechanical and analogue, but digital electronic FCSs soon became the new standard with the addition of motion sensors and pressure sensor units. Fly-by-wire, which replaced the direct mechanical links with electrical signaling, allowed pilots to directly control the aircraft's motion. The fourth generation of FCSs is characterized by full-time, full-authority electronic FCSs with a much lower probability of failure, less than one total failure in a billion flying hours, thanks to the use of electronic and hydraulic equipment. The Airbus A320 was the first civil aircraft to feature fly-by-wire technology, introduced in 1987. [1]

In recent decades, the demand for high-performance flight surface control has surged, prompting a desire to substitute the conventional fly-by-wire (FBW) actuation system with the advanced Power By-Wire (PBW) actuation system. An emerging trend in the aeronautical industry is to minimize the usage of hydraulic power sources, whenever feasible, due to the numerous complications and disadvantages associated with their utilization. Consequently, the research focus in the industry has shifted towards incorporating a greater presence of electrical

power sources within aircraft, leading to the concept of the "more electric aircraft" (MEA). The primary objective of this approach is to gradually replace hydraulic components with electric devices, thereby resolving the aforementioned critical issues and bringing forth additional advantages.

# Chapter 2

# Electromechanical actuators for More/All Electric aircraft systems

The electrical actuation system employing PBW actuators, such as electro hydrostatic actuator (EHA) and electromechanical actuator (EMA) shown in Figure 2.1, transports the power in 'wires' between the devices instead of hitherto hydraulic pipeline, which remarkably improves the actuation performance of aircrafts.

Studies have shown that PBW actuators will benefit actuation systems with a series of advantages due to their fault-tolerant capability and exclusion of pipes and fluids:

(a) increased safety and reliability due to the absence of poisonous and flammable hydraulic fluids

(b) reduced weight, volume, and complexity of power transmission paths;

(c) easier maintenance and less costs due to the lack of hydraulic leaks and better diagnostic capability;

(d) higher energy efficiency and better dynamic characteristics.

EHAs are currently used for primary flight controls, while EMAs are employed for secondary flight controls. In Figure 2.1(a), the EHA is a self-contained hydraulic actuator with a pump driven by an electric motor with variable speed. Unlike hydraulic systems, power control is managed by the pump, which adjusts the flow and hydraulic power by changing the pump's speed. The electric motor and pump assemblies control the piston's position, connected to the load, by transferring fluid

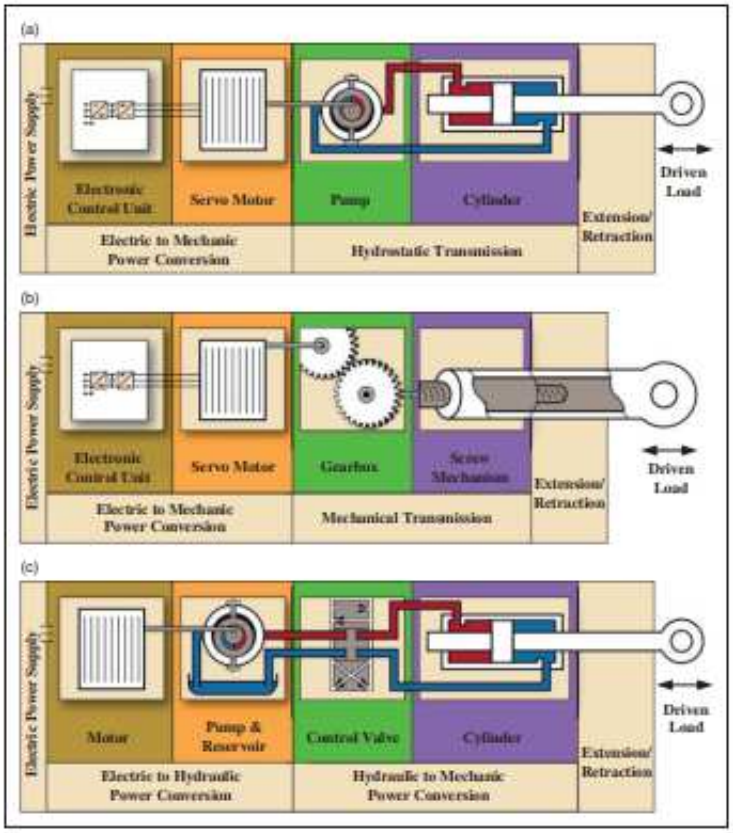


**Figure 2.1:** Power-by-wire actuators and HSA composition. (a) EHA, (b) EMA, and (c) HSA.

back and forth between the cylinder chambers. This eliminates the need for bulky piping systems and external hydraulic sources. On the other hand, EMAs eliminate the use of local hydraulic devices and do not require hydraulic flow to drive the screw rod. This leads to reduced maintenance due to lower energy conversion and offers a leak-free operation. EMAs also provide a weight advantage over EHAs when sized for the same actuation requirements. Despite these advantages, researchers and engineers still face challenges in the development of EMA technologies for future aircraft applications. One primary concern is the lack of accumulated knowledge and experience regarding reliability, potential failures such as jamming, health monitoring, assessment, and thermal management. [3]

Despite extensive research and development efforts, electromechanical actuators (EMAs) are not currently considered mature enough for primary flight controls, mainly due to their susceptibility to jamming, except for low-power applications. It is widely recognized that EMAs for primary flight control applications have

a significant distance to go before they can be widely accepted in aviation as a safe and reliable option. EMAs are more readily accepted by manufacturers for less safety-critical applications such as flaps, slats, spoilers, and trim horizontal stabilizers. These surfaces are considered less prone to catastrophic consequences in the event of jamming, as they are operated intermittently rather than continuously.

## 2.1 Electromechanical actuation systems

Electro-mechanical servo systems belong to a category of controlled actuation devices that utilize electrical energy to transform and modulate power, resulting in mechanical output. In the system diagram shown in Figure 2.2, the acquisition and control electronics (ACE) play a significant role. The ACE manages the input and feedback signals of the system, implements control laws, and sends command signals to the power electronics based on the observed error between the desired and actual values.

The power electronics modulate the electrical power from the source, depending on the command signal received, to supply the actuation system with the necessary power to achieve the desired set signal. The electric motor converts the electrical energy from the source into mechanical energy by interacting the electric and magnetic fields. This interaction generates torque for rotary motors or force for linear motors, acting on the device's rotor. In the case of rotary motors, the rotor is typically not the final output. Mechanical transmission elements, such as gears, are often used to reduce torque requirements or convert rotary motion into linear displacement.

For this application, the preferred motor type is the Brushless Direct Current Motor (BLDC) due to its higher power density and lower maintenance compared to traditional brush motors. Regarding mechanical transmission, a reducer is not always necessary but is preferred for the considered application. The reducer serves to multiply the motor's torque and reduce the output speed to ensure optimal motor operation, avoiding oversizing. Gear train (or ordinary) reducers and planetary reducers are commonly used in the aerospace sector. Gear train reducers are suitable for low transmission ratios, offering simplicity and weight reduction. Planetary reducers are employed for high transmission ratios, providing a compact design with reduced weight. Finally, rotary motion is converted into linear motion using mechanisms that often involve screw-nut techniques with satellite rollers or ball recirculation.

To monitor the system's behavior, an appropriate number of sensors, each with its own measurement chain, are utilized. These sensors contribute to the overall system monitoring and feedback loop.

EMAs can be categorized as either linear or rotary types. In the case of linear

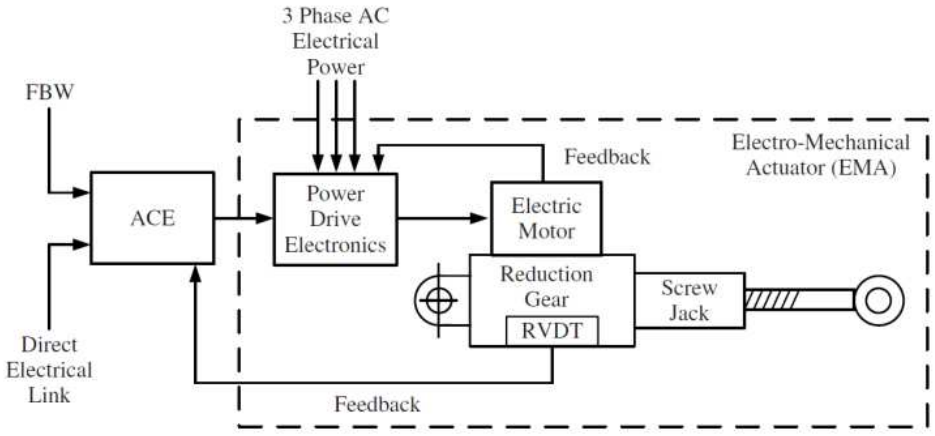


**Figure 2.2:** Electro-mechanical actuator.[2]

EMAs, the rotational motion generated by the motor is converted into linear motion through the use of a mechanical assembly, such as a ball or roller screw mechanism. On the other hand, for rotary EMAs, the motor's rotational speed is typically reduced using a gearbox. This gearbox is then connected to the surface either directly to the hinge line or through a connecting rod assembly. Figure 2.3 illustrates the key components and distinctions between linear and rotary EMAs.

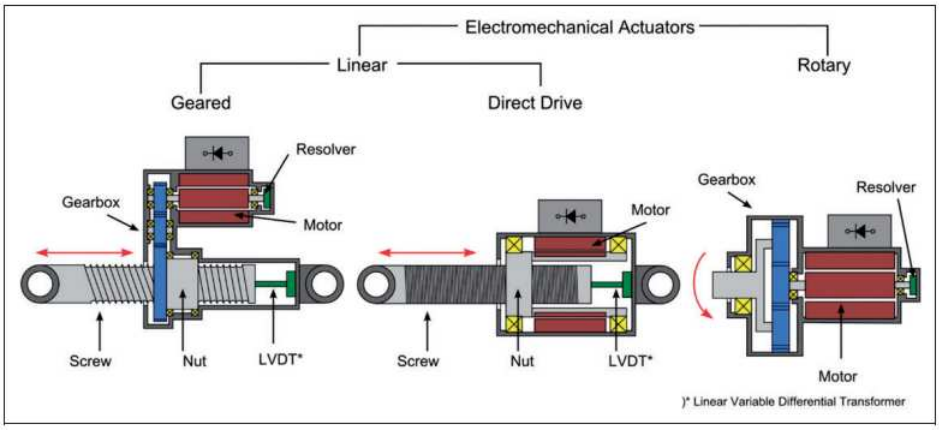


**Figure 2.3:** Classification of different EMA types.

## 2.2 EMA architecture

Electromechanical actuators play a crucial role in the control surfaces of an aircraft, enabling precise control of its flight characteristics. Various configurations of actuators are employed to ensure redundancy and enhance safety. Two common configurations include parallel actuators and active/inactive setups.

In the parallel actuator configuration, two actuators are installed in parallel to control a single flight surface. This arrangement provides redundancy, as both actuators can independently manipulate the surface. In case of a failure or malfunction in one actuator, the other can continue to operate, maintaining control of the surface. This configuration offers increased reliability and fault tolerance.

Another configuration involves utilizing two actuators but activating only one at a time, while keeping the other actuator in a standby or inactive state. This arrangement is often employed to distribute the load and increase the lifespan of the actuators. The active actuator performs the majority of the control surface movement, while the inactive actuator remains in reserve. Periodically, the roles may be switched to evenly distribute wear and tear on the actuators.

In both configurations, the actuators are typically equipped with sensors and feedback mechanisms to provide accurate positioning and control. These sensors continuously monitor the actuator's position, velocity, and force output, enabling precise control of the flight surface. The selection of the appropriate actuator configuration depends on several factors, including the specific aircraft design, safety requirements, weight considerations, and system complexity.

For this application, it has been decided to use the configuration that involves the utilization of two actuators in parallel. Additionally, both actuators are identical, so the sizing of only one actuator is provided. Later, other operating conditions will be considered, which include a single active actuator.

PARALLEL ACTUATORS:

Advantages:

- Redundancy: The use of multiple actuators provides redundancy, ensuring that control of the flight surface can be maintained even if one actuator fails or malfunctions.
- Increased Reliability: The redundancy offered by parallel actuators enhances the overall reliability of the flight control system.
- Fault Tolerance: In the event of an actuator failure, the remaining actuators can compensate and continue to control the flight surface, reducing the impact on aircraft performance and safety.

Disadvantages:

- Increased Weight and Complexity: Installing multiple actuators adds weight and complexity to the aircraft, potentially impacting fuel efficiency and increasing maintenance requirements.
- Higher Cost: The use of additional actuators and associated components increases the cost of the system, including installation, maintenance, and potential repairs.

ACTIVE/INACTIVE ACTUATORS:

Advantages:

- Load Distribution: By periodically switching the active and inactive roles between the actuators, the workload is distributed, reducing wear and tear and prolonging the overall lifespan of the actuators.
- Enhanced Efficiency: The active/inactive configuration optimizes the usage of actuators, allowing one actuator to handle most of the control surface movement while the other remains in standby, resulting in efficient operation.

Disadvantages:

- Reduced Redundancy: Unlike parallel actuators, the active/inactive configuration does not offer immediate redundancy in case of actuator failure. If the active actuator fails, the standby actuator needs to be activated promptly to maintain control.
- Increased Complexity: Implementing an active/inactive configuration requires additional control logic and monitoring systems to ensure smooth switching and coordination between the actuators, adding complexity to the flight control system.

# Chapter 3

# Sizing of components

As starting point , a collection of design requirements was carried out.The sizing specifications have been assumed rescaling conventional values according to the correct geometry of the reference regional aircraft. The operating temperature range of the aircraft was assumed to be from -54°C to +40°C. At the end of this phase, a complete EMA command line was sized. The following subsections describe the components that were chosen for this actuation device, based on the necessary requirements and sizing criteria.

| LOADS | |
|---|---|
| Maximum torque required for actuators $T_N$ | 4810 [Nm] |
| Maximum load acting on the actuator $F_N$ | 5066 [N] |
| STROKE | |
| Advancement time $t_a$ | 10 [s] |
| Linear stroke of the actuator $x_{max}$ | 0.580 [m] |
| Flap angular stroke $\theta_{max}$ | 0.611 [rad] |
| Nominal linear speed $V_n$ | 0.058 [m/s] |

**Table 3.1:** Input parameters

## 3.1 Sizing steps

Before starting the actual sizing, first the elements that compose the system were defined, then the dependencies between these elements were established, and finally, assumptions were made about the unknown data.

The figure 3.1 illustrates an initial sizing flow where all the elements that need to be sized are present and arranged in the order in which the sizing should be performed.Furthermore, it is specified in which parts assumptions need to be made.

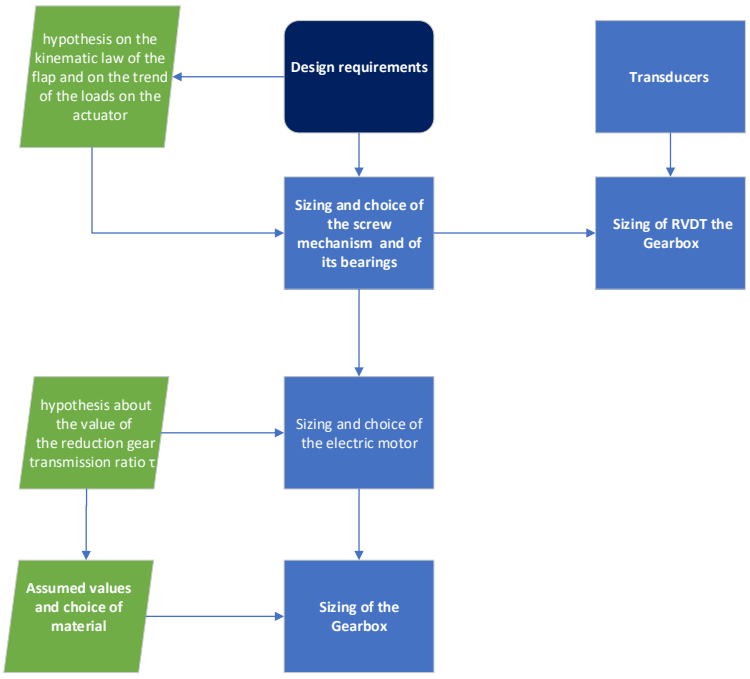


**Figure 3.1:** First sizing flow chart

The figure 3.2 illustrates a more detailed schematic of the sizing phases. Each block has been subdivided into sub-blocks corresponding to the various operations required to size the component. Additionally, the outputs of each block, which serve as inputs to the subsequent blocks, are specified. The assumed values are also detailed. Furthermore, formulas for gearbox verification are presented. Finally, check blocks are included that lead to the end of the sizing process if passed, or back to the assumed values if failed.

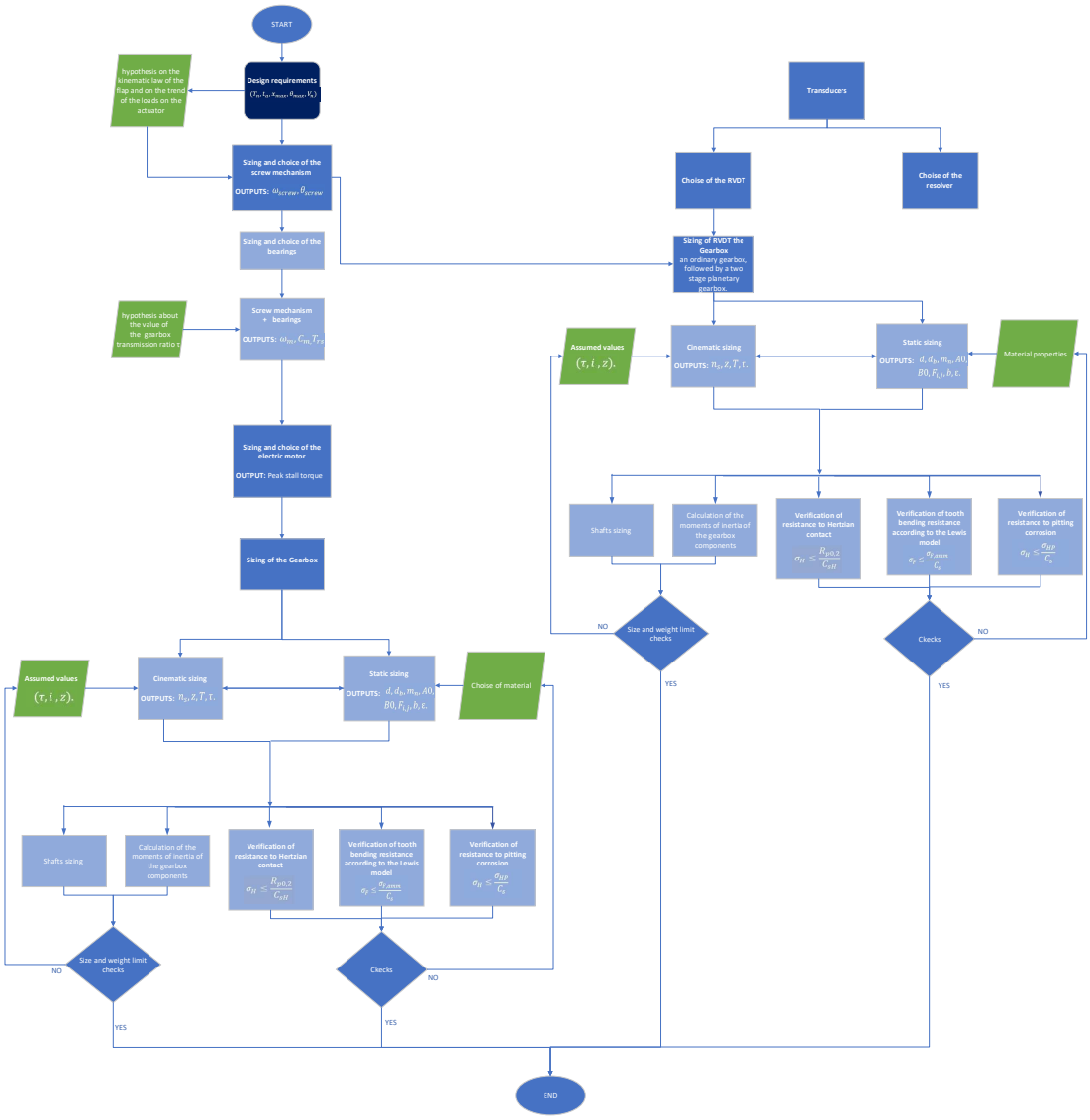


**Figure 3.2:** Intermediate sizing flowchart

Finally, the final sizing diagram shown in figure 3.3 is very similar to the intermediate diagram,but includes more detailed steps. This diagram loses the generality of the previous diagrams and focuses specifically on the conducted sizing process. The assumed values are explicitly stated, and the chosen component types, models, and manufacturers are specified.

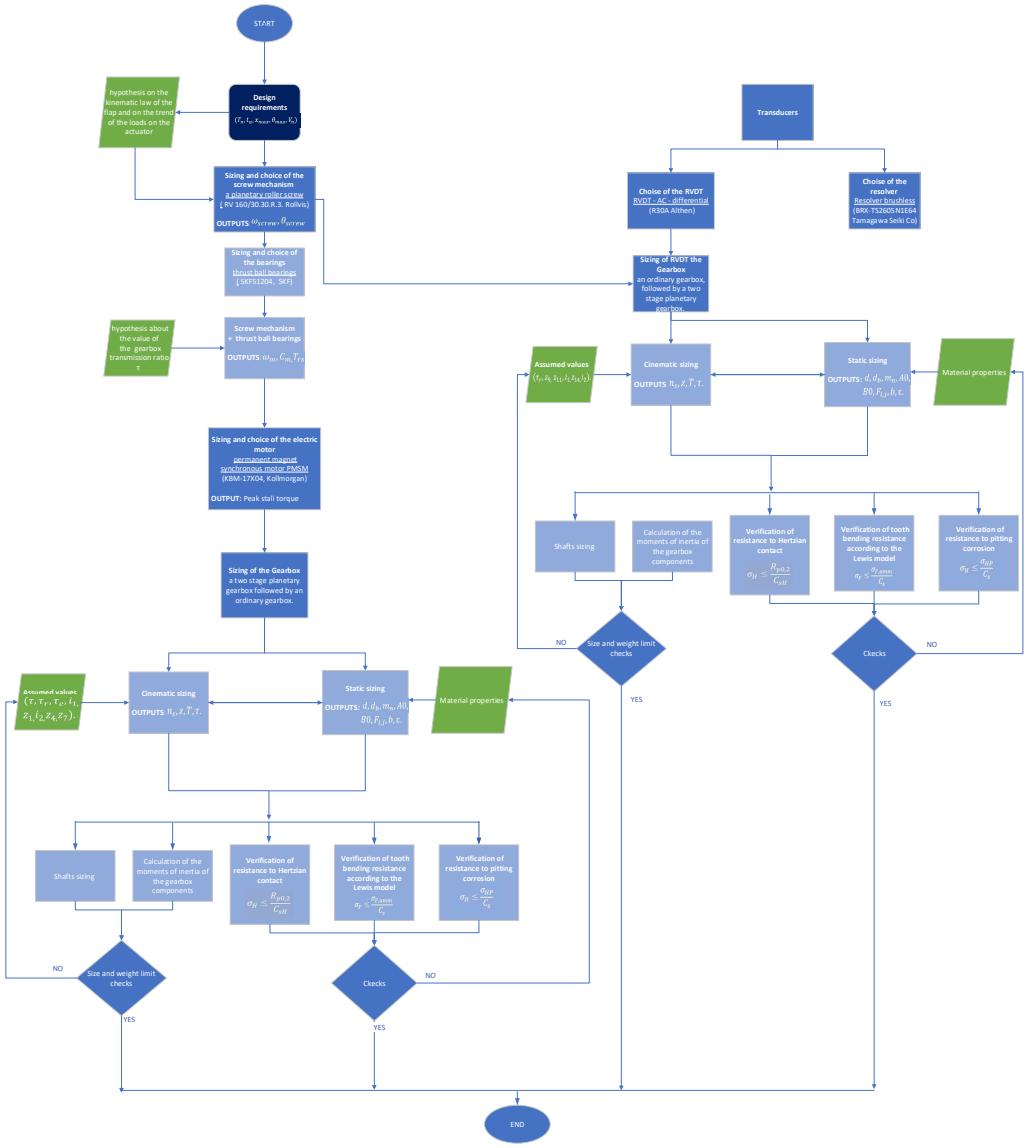


**Figure 3.3:** Final sizing flowchart

## 3.2 The control surface

The EMA, sized in the following paragraphs, is used for secondary flight control, specifically, the control surface in question is a fowler flap (it was described in Chapter 1). The mass of the flap was set equal to 50 kg and it was assumed that the maximum load is in correspondence with its maximum extension. Since the exact x-$\theta$ kinematic law is not known, it was decided to approximate the movement of the flap with a parabolic curve:

$$x = a\theta^2 + b\theta \tag{3.1}$$

- b: it was assumed arbitrarily;
- a: it was calculated with the formula:

$$a = \frac{x_{max} - b\theta_{max}}{\theta_{max}^2} \tag{3.2}$$

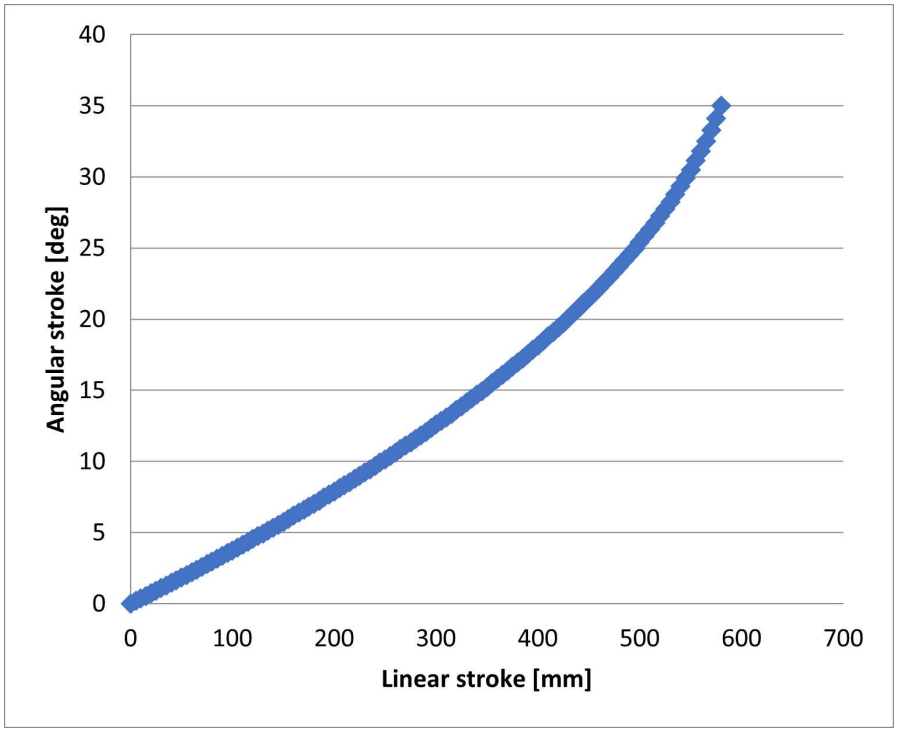


**Figure 3.4:** Kinematic law

Once the kinematic law has been obtained, it is possible to study the trend of the loads on the actuator.

## 3.3 Sizing and choice of the screw mechanism

The screw mechanism is used to convert the rotary motion to linear motion. The goal of this conversion is to change the torque and rotational speed produced by an electric motor into force and linear speed, which can then be used to operate the flight control surface.

It was decided to use a planetary roller screw of the manufacturer Rollvis, specifically the RV 160/30.30.R.3. was chosen.

The application of a preloading force (Fv) was considered to eliminate play and increase stiffness.

$$F_V = \frac{F_{max}}{2.83} \tag{3.3}$$

However, calculations have shown that the effect of both axial and angular backlash on the positioning of the flaps is minimal. As a result, the preload was deemed unnecessary.

Starting from the project specifications and following the formulas in the catalogue [4], the values summarized in Table 3.2 were calculated.

A pitch was chosen that does not require high rotational speeds of the screw, ensuring that the corresponding coefficient of static load C0 is in accordance with the minimum required coefficient of static load ($C0_{min}$).

$$C0_{min} = F_N \cdot CS = 10.13[kN] \tag{3.4}$$

The static safety factor was assumed to be equal to 2.

| Technical Characteristic | |
|---|---|
| Dynamic load capacity Ca | 149.8 [kN] |
| Static load capacity C0 | 197.4 [kN] |
| Geometric parameters | |
| Pitch size p | 30 [mm] |
| Medium diameter $d_0$ | 30[mm] |
| Helix angle $\alpha$ | 0.308 [rad] |
| Diameter of the rollers $d_r$ | 9[mm] |
| Lenght of the rolls $L_r$ | 71 [mm] |
| Screw length L | 870 [mm] |
| Nut diameter $D_1$ | 62 [mm] |
| Output parameters | |
| Lifespan $L_{10}$ | 47242 [millions of revolutions] |
| Lifespan $L_c$ | 2.44 $\cdot 10^9$ [number of runs] |
| Lifespan $L_h$ | 6.79 $\cdot 10^6$ [hours] |
| Permissible critical rotational speed $n_{krzul}$ | 1095.8 $[min^{-1}]$ |
| Approximate screw mass $m_{rs,s}$ | 4.83 [kg] |
| Approximate nut mass $m_{rs,r}$ | 15.79 [kg] |
| Angular stroke $\theta_{screw}$ | 121.5 [rad] |
| Angular speed of the screw $\omega_{screw}$ | 12.15 [rad/s] |
| Angular speed required of the motor $\omega_m$ | 696 [rpm] |
| Torque required at the motor shaft $C_m$ | 5,452 [Nm] |
| Total torque required at the gearbox output $T_{rs}$ | 32.71 [Nm] |

**Table 3.2:** Screw sizing (RV 160/30.30.R.3)

The parameters in table 3.2 have been calculated using the following formulas :

$$\alpha = arctan\left(\frac{P}{\pi \cdot d_0}\right) \tag{3.5}$$

$$L = 1.5 \cdot x_{max} \tag{3.6}$$

$$L_{10} = f_r \cdot \left(\frac{C}{F_m}\right)^3 \tag{3.7}$$

$f_r$ is a reliability factor, while $F_m$ is the medium load.

$$L_c = \left( \frac{L_{10} \cdot 10^6}{\theta_{screw,[giri]}} \right) \tag{3.8}$$

$$L_h = \left( \frac{L_c \cdot t_a}{3600 \cdot \frac{s}{h}} \right) \tag{3.9}$$

$$n_{krzul} = 0.8 \cdot n_{kr} \cdot f_{kr} \tag{3.10}$$

$f_{kr}$ is a correction actor according to the type of bearings

$$n_{kr} = 108 \cdot 10^6 \cdot d_0 \cdot \frac{1}{L^2} \tag{3.11}$$

$$mass_{rs,s} = \pi \cdot L \cdot \left( \frac{d0}{2} \right)^2 \cdot d_{steel} \tag{3.12}$$

$$mass_{rs,r} = \pi \cdot L \cdot \left( \left( \frac{D1}{2} \right)^2 - \left( \frac{d0}{2} \right)^2 \right) \cdot d_{steel} \tag{3.13}$$

$$\theta_{screw} = \frac{x_{max} \cdot 2\pi}{p} \tag{3.14}$$

$$\omega_{screw} = \frac{V_n \cdot 2\pi}{p} \tag{3.15}$$

$$\omega_m = \omega_{screw} \cdot \tau \tag{3.16}$$

$$C_m = \frac{T_{rs}}{\tau} \tag{3.17}$$

$$T_{rs} = T_{rs,n} + T_{rs,tb} \tag{3.18}$$

$$T_{rs,n} = \frac{F_N \cdot p}{2\pi \cdot \eta} \tag{3.19}$$

$$T_{rs,tb} = T_{frs,tb} + T_{rr} \tag{3.20}$$

$$T_{rs,tb} = M_{seal} + M_{sl} \tag{3.21}$$

The angular speed required of the motor $\omega_m$ and torque required at the motor shaft $C_m$ values have been calculated assuming the reduction gear transmission ratio $\tau$ equal to 8.

### 3.3.1 Satellite roller screws compared to ball screws

Satellite roller screws are distinct from ball screws primarily due to their utilization of threaded rollers rather than balls as load transfer elements. The key benefit of satellite roller screws lies in their significantly greater number of contact points, with the thread profile effectively resembling a considerably larger ball diameter.

in terms of load capacity and lifespan, roller screws offer a notable advantage over ball screws. This is primarily due to the utilization of threaded rollers instead of balls, which allows for a higher distribution of load over a greater number of contact points. Consequently, roller screws exhibit higher admissible static and dynamic load capacities, making them more capable of handling heavy loads and ensuring a longer lifespan.

Speed and acceleration capabilities are notable advantages of satellite roller screws. These roller screws can achieve significantly higher rotational speeds and support much greater acceleration compared to other alternatives. Specifically, RV satellite roller screws are designed in a way that eliminates roller recirculation. As a result, they can reach rotation speeds up to twice as fast as ball screws. Additionally, the acceleration achievable with satellite roller screws can reach up to 3g, enabling swift and efficient motion.

The high number of contact points and the geometry of the contacts give a satellite roller screw greater rigidity and shock tolerance than a ball screw [4].

**Figure 3.5:** Satellite roller screws compared to ball screws

### 3.3.2 Sizing and choice of the bearings

When it comes to choosing bearings for screw actuators, several factors should be taken into consideration. Here are some important points:

1. Load Capacity: The bearings must be capable of handling the anticipated load. Consider both the axial and radial loads that will be exerted on the screw actuator during operation.

2. Speed and Efficiency: The chosen bearings should allow for smooth and efficient motion of the screw actuator, minimizing friction and ensuring optimal performance at the desired speed.

3. Precision and Accuracy: If high precision and accuracy are required for the application, select bearings that offer tight tolerances and minimal backlash to ensure precise positioning of the screw actuator.

4. Environment and Conditions: Evaluate the operating environment and conditions such as temperature, moisture, dust, and potential contaminants. Choose bearings that are suitable for these conditions to ensure longevity and reliable performance.

5. Lubrication and Maintenance: Consider the lubrication requirements of the bearings and whether they need periodic maintenance. Some bearings may require regular lubrication, while others may be self-lubricating or maintenance-free.

6. Cost and Availability: Assess the overall cost and availability of the chosen bearings, taking into account factors such as initial purchase cost, maintenance expenses, and the availability of replacements if needed.

Choosing a single-acting thrust ball bearing offers several advantages:

- Cost Efficiency: Single-acting thrust ball bearings are generally more cost-effective compared to double-acting thrust ball bearings or other types of thrust bearings. This can be particularly beneficial if cost is a significant factor in your application.

- Space Optimization: Single-acting thrust ball bearings have a compact design, allowing for space optimization in applications where installation space is limited. They can be an excellent choice when dealing with constrained or tight spaces.

- One-Directional Load: If your application requires handling a unidirectional axial load, a single-acting thrust ball bearing is ideal. These bearings are

specifically designed to support loads in one direction and are not designed to handle bidirectional or reversing loads.

- Simplicity and Ease of Installation: Single-acting thrust ball bearings are relatively straightforward to install and operate. Their design simplicity makes them easy to incorporate into various systems, simplifying the installation process.
- Low Friction: Single-acting thrust ball bearings typically have low friction characteristics, which can contribute to improved efficiency and reduced power consumption in your application.

It has been chosen a single-acting thrust ball bearing with an average diameter equal to the average diameter of the screw (30mm), in order to avoid excessive section variations.It also has a static safety factor greater than the required value (usually $s_{0min}$ =1.5) The SKF51205 bearing has been chosen, and the following table presents the data taken from the catalog [5]

| Dimensions | |
|---|---|
| Bore diameter d | 25 [mm] |
| Outside diameter D | 47 [mm] |
| Height H | 15 [mm] |
| Mass bearing | 0.11 [kg] |
| Performance | |
| Basic dynamic load rating C | 26.5 [kN] |
| Basic static load rating $C_0$ | 50 [kN] |
| Reference speed | 5300 [rpm] |
| Limiting speed | 7500 [rpm] |
| Minimum load factor A | 0.015 |
| Fatigue load limit Pu | 1.86 [kN] |

**Table 3.3:** Thrust ball bearings sizing (SKF51205)

To ensure the correct functioning of the device it is necessary to ensure a minimum load equal to:

$$F_{am} = A \cdot \left(\frac{n}{1000}\right)^2 = 2.02 \cdot 10^{-4}[kN] \tag{3.22}$$

Subsequently, the static safety factor was verified, which is equal to the static load coefficient divided by the equivalent static load on the bearing (in this case, equal to the maximum load acting on the actuator and and it also corresponds to the Equivalent dynamic load on the bearing, P)

$$s_0 = \frac{C_0}{P_0} = 9.87 \tag{3.23}$$

Afterward, the duration of the bearing was calculated using the SKF formula in accordance with ISO standards. This formula takes into account the lubricant conditions and contamination level, which reflect the operating conditions of the application.

$$L_{nm} = a_1 \cdot a_{skf} \cdot (\frac{C}{P})^p = 69.13 \; millionrounds \tag{3.24}$$

where:

- $a_1$: relative duration correction factor to reliability. Considering a reliability of 99 % it is equal to 0.21
- $a_{skf}$: SKF life correction factor. It is found through graphs as a function of the values of k and $\eta_c \cdot P_u/P$ where $\eta_c$ takes into account the level of contamination of the bearing and in normal working conditions is equal to 0.5, while k is a viscosity ratio, which takes into account the lubrication conditions, it has been assumed equal to 2. In our case the SKF factor is equal to 2.3.
- p is an exponent of the duration formula which for ball bearings is equal to 3.

In rolling bearings, friction is a determining factor in terms of internal heat development and therefore the operating temperature. The magnitude of friction depends on the load and several other factors, the most important of which are the type and dimensions of the bearing, its rotational speed, and the properties and quantity of lubricant.

In a bearing, the total resistance to rotation is caused by the rolling and sliding friction existing in the contacts between the raceways and rolling elements, in the contact areas between these elements and the cage, and on the guiding surfaces of the rolling elements or the cage. It is also influenced by the friction in the lubricant and the sliding friction of the sealing elements, if provided.

The frictional moment can be calculated with sufficient precision, using a constant coefficient of friction µ, with the following formula:

$$M = 0.5 \cdot \mu \cdot F \cdot d = 1.19 * 10^{-1} Nm \tag{3.25}$$

where:

- $\mu$ constant coefficient of friction of the bearing, which in the case of thrust ball bearings is equal to 0.0013;
- F is equivalent dynamic load on the bearing;
- d is the average diameter.

The new SKF calculation methods allow a more precise determination of the moment of friction that occurs in rolling bearings SKF according to the formula

$$M = M_{rr} + M_{sl} + M_{seal} + M_{drag} \tag{3.26}$$

**Rolling frictional moment**

$$M_{rr} = \Psi_{ish} \Psi_{rs} G_{rr} \cdot (\nu n)^{0.6} \tag{3.27}$$

where:

- $\Psi_{ish}$: heating reduction factor due to shear phenomena;
- $\Psi_{rs}$: reduction factor of the phenomenon of fill/shortage;
- $G_{rr}$: variable that depends on the type of bearing, the average diameter of the bearing, and the loads;
- $\nu$: rotational speed [rpm];
- n: kinematic viscosity of the lubricant at operating temperature $[mm^2/s]$.

**Sliding frictional moment**

$$M_{seal} = G_{sl} \mu_{sl} \tag{3.28}$$

where:

- $G_{sl}$: variable that depends on the type of bearing, the average diameter of the bearing, and the loads;
- $\mu sl$: sliding friction coefficient

**Seals drag torque**

$$M_{seal} = K_{S1} d_s^b + K_{s2} \tag{3.29}$$

where:

- $K_{s1}$: constant that depends on the type of bearing;
- $d_s$: opposite seal surface diameter;
- b: exponent which depends on the type of bearing and seals;
- $K_{s2}$: constant that depends on the type of bearing and seals.

**Friction torque due to drag losses**

$$M_{drag} = V_M K_{ball} d_m^5 n^2 \tag{3.30}$$

where:

- $V_M$: variable according to the oil level;
- $K_{ball}$:constant relating to ball bearings;
- $d_m$:mean bearing diameter [mm];
- n: rotation speed [rpm].

The following table shows the calculated values:

| | |
|---|---|
| Rolling frictional moment $M_{rr}$ | $3.83 \cdot 10^{-4}$ [Nm] |
| Sliding frictional moment $M_{sl}$ | 0.0167 [Nm] |
| Seals drag torque $M_{seal}$ | 0.0057 [Nm] |
| Friction torque due to drag losses $M_{drag}$ | $1.01 \cdot 10^{-6}$ [Nm] |

**Table 3.4:** moments of friction on the bearing

## 3.4 Sizing of the Gearbox

Thanks to their reliability and high power transmission capabilities, gear wheels have been the primary means of mechanical power transmission since the early days of aviation. Currently, most aircraft gears are used for two purposes: power transmission from the main engine shaft to various aircraft systems and reduction of the transmission ratio for flight control surfaces.

For the first task, power is typically extracted from the main engine shaft using bevel gears (or occasionally, when space permits, cylindrical gears). Then, with a series of cylindrical gears, the power is distributed to various users. For the second task, due to limited space, the use of epicyclic (planetary) reducers is very common.

Introducing a reduction system between the engine and the roller screw offers several advantages over direct drive solutions. The use of a reducer reduces weight and ensures radial balance of the system, thereby reducing loads on the supports. Additionally, since the torque output from the engine is multiplied and the input speed to the screw is reduced, the use of a reducer improves performance and avoids oversizing of the electric motor, as the motor tends to work better with higher speeds and lower torque.

However, at the same time, the introduction of an additional mechanism that can have a high number of contacting bodies (such as an epicyclic reducer) increases dissipations due to friction and decreases the reliability of the system.

**Types of reducers**

Gearboxes used to transmit motion between two parallel axes can be catalogued into three basic categories:

- *ordinary gearboxes* An gearing system is referred to as ordinary if the axes of all the gear wheels that constitute it are fixed. To achieve high transmission ratios, it is necessary to apply a large number of gear wheels with increasing sizes, resulting in progressively larger increases in terms of size and mass. This type of reducer is therefore not suitable for the application described in this thesis: in the aerospace servo system context, transmission ratios must be high while ensuring minimized weight and size.

- *planetary gearboxes* Epicyclic reducers, which are also composed of multiple chains of gear wheels, differ from ordinary reducers in that the shafts of some wheels (satellites) are not fixed but instead mobile. One of the primary applications of epicyclic gearing is found in high reduction ratio reducers. In fact, they allow for significantly smaller dimensions compared to ordinary reducers, while maintaining the same reduction ratio.

- *harmonic gearboxes* Harmonic drive reducers employ a flexible and deformable cylindrical toothed element (flexspline) that engages with a circular spline and an elliptical structure equipped with rolling bearings (wave generator). This unique mechanism enables high gear reduction ratios with zero backlash and high torque output. Harmonic drive reducers are known for their compactness, precision, and low-weight characteristics, making them suitable for aerospace applications. The harmonic gearboxes are able to transfer higher torque values than theepicycloidal thanks to the large number of teeth in contact, while an advantage of the latterwith respect to the harmonics can be identified in the lower inertia, thus making themparticularly suitable for requiring high dynamics, as in the case of the servoactuators.

The main purpose of the gearbox is transforming the servo motor's high speed and low torque to low velocity and high torque of a screw mechanism. For this application it was decided to use a two stage planetary gearbox followed by an ordinary gearbox.

The sizing of the gearbox began with static and dynamic sizing, followed by the verification of resistance to Hertzian contact, the Verification of tooth bending resistance and the verification of resistance to pitting corrosion. It concluded with the sizing of the shafts and the calculation of the mass and the moments of inertia the gearbox components.

The main characteristics of the chosen material are shown in the Table 3.5.

| Material:40NiCrMo7 | |
|---|---|
| Tensile strength $R_m$ | 1950 [MPa] |
| Yield point Rp0,2 | 1640[MPa] |
| Fatigue limit load $\sigma_{D-1}$ | 480 [Mpa] |
| Young's modulus E | 210000[Mpa] |
| Maximum contact pressure$\sigma_{H,lim}$ | 1270 [Mpa] |
| Density $\rho$ | 7850 $[kg/m^3]$ |

**Table 3.5:** Material properties

### 3.4.1 Static and dynamic sizing

The sizing starts with an assumption regarding the gear ratios and the number of teeth of some gears. This is followed by the assumption about gear ratio (carried stopped), which allows for the calculation of the transmission ratios of the first and second stages according to the following formulas:

$$\tau 1 = (1 - i_1) \tag{3.31}$$

$$\tau 2 = (1 - i_2) \tag{3.32}$$

| Assumed parameters | |
|---|---|
| The planetary gearbox transmission ratio $\tau$e | 18 |
| The ordinary gearbox transmission ratio $\tau$r | 1 |
| First stage gear ratio (carried stopped) i1 | -5 |
| Second stage gear ratio(carried stopped) i2 | -2 |
| Number of teeth on sun gear (first stage) z1 | 28 |
| Number of teeth on sun gear (second stage) z4 | 60 |
| Number of teeth on pinion z7 | 35 |

**Table 3.6:** Calculation assumptions

Subsequently, it was decided to use 3 satellites, ensuring that this number remains below the maximum allowable number of satellites.

$$n_{s,max} = |\frac{\pi}{arctan(\frac{z_3+2}{z_3+z_1})}| = 5 \tag{3.33}$$

The sizing of the first stage continues according to the following formulas:

$$z_3 = i_1 \cdot z_1 \tag{3.34}$$

$$d_1 = m_n \cdot z_1 \tag{3.35}$$

$$d_3 = m_n \cdot z_3 \tag{3.36}$$

$$d_2 = \frac{d_3}{2} - \frac{d_1}{2} \tag{3.37}$$

$$z_2 = \frac{d_2}{m_n} \tag{3.38}$$

$$d_b = d \cdot cos(\alpha) \tag{3.39}$$

To determine the wheel modulus, the Lewis method was employed.

$$m_{n,Lw} = \sqrt[3]{\frac{y_{Lw} \cdot 2T_1}{n_s \cdot \lambda \cdot \sigma_{amm} \cdot z_1}} = 4.2 \cdot 10^{-1} \tag{3.40}$$

where:

- $y_{Lw}$ is the Lewis factor, its value is tabulated according to the number of teeth and the pressure angle;
- $n_s$ is the number of satellites;
- $\lambda = \frac{b}{m} = 20$ (hypothesis);
- $\sigma_{amm} = \frac{R_{p0.2}}{C_{s,st,min}}$

Once these values are known, it is possible to calculate the tooth band width and the maximum effective static stress acting on the tooth:

$$b = \lambda \cdot m_n \tag{3.41}$$

$$\sigma_{max} = \frac{2T_1 \cdot y_{Lw}}{n_s \cdot \lambda \cdot z_1 \cdot m_n^3} \tag{3.42}$$

Finally the contact ratio was calculated with the following formulas:

$$\epsilon = \frac{AB}{p_b} \tag{3.43}$$

where:

- AB is the contact segment length

  $AB = \sqrt{AO_2^2 - r_{b2}^2} + \sqrt{BO_1^2 - r_{b1}^2} - (AO_2 + BO_1)sin(\alpha)$

  $AO_2 = r_2 + addendum = r_2 + m_n; \;\; BO_1 = r_1 + addendum = r_1 + m_n$

- $p_b$ is the basic step $p_b = m_n \pi cos(\alpha)$

Using a similar approach, the sizing of the second stage and the ordinary gearing was determined. All sizing results are summarised in Table 3.7

| Sizing results | | | | | | | | | | | |
|---|---|---|---|---|---|---|---|---|---|---|---|
| z1 | 28 | d1 | 28[mm] | d1b | 26.3[mm] | z5 | 30 | d5 | 45[mm] | d5b | 42.3 [mm] |
| z2 | 56 | d2 | 56[mm] | d2b | 52.6[mm] | z6 | 120 | d6 | 180[mm] | d6b | 169.1[mm] |
| z3 | 140 | d3 | 140[mm] | d3b | 131.6[mm] | z7 | 35 | d7 | 88[mm] | d7b | 82.2[mm] |
| z4 | 60 | d4 | 90[mm] | d4b | 84.6[mm] | z8 | 35 | d8 | 88[mm] | d8b | 82.2[mm] |
| normal modulus of the first stage wheels $m_{n1st}$ | | | | | | | | 1 [mm] | | | |
| normal modulus of the second stage wheels $m_{n2st}$ | | | | | | | | 1.5 [mm] | | | |
| normal modulus of the ordinary gearbox wheels $m_n$ | | | | | | | | 2.5 [mm] | | | |
| Face width b1=b2=b3 | | | | | | | | 20 [mm] | | | |
| Face width b4=b5=b6 | | | | | | | | 30 [mm] | | | |
| Face width b7=b8 | | | | | | | | 50 [mm] | | | |
| First stage gear ratio $\tau 1$ | | | | | | | | 6 | | | |
| Second stage gear ratio $\tau 2$ | | | | | | | | 3 | | | |
| Contact ratio $\epsilon_{1/2}$ | | | | | | | | 1.47 | | | |
| Contact ratio $\epsilon_{2/3}$ | | | | | | | | 1.60 | | | |
| Contact ratio $\epsilon_{4/5}$ | | | | | | | | 1.49 | | | |
| Contact ratio $\epsilon_{5/6}$ | | | | | | | | 1.53 | | | |
| Contact ratio $\epsilon_{7/8}$ | | | | | | | | 1.45 | | | |

**Table 3.7:** Gearbox sizing

As regards the torques acting on the wheels, the torque T1 acting on the first stage solar was assumed equal to Peak stall Torque of the electric motor. The torque acting on the second stage solar and the torque acting on the pinion have been calculated withe the formulas below:

$$T4 = T1 \cdot \tau_1 \tag{3.44}$$

$$T7 = T1 \cdot \tau_e \tag{3.45}$$

### 3.4.2 Verification of resistance to Hertzian contact

It is necessary to ensure that the specific contact pressures, that is, the Hertzian stresses that occur locally during meshing, are lower than the allowable stress of the material. Excessive specific contact pressure would lead to surface deterioration of the tooth, which is unacceptable for proper gear operation. From the perspective of Hertzian contact, straight teeth meshing can be considered as two cylinders in contact along a generatrix with a length equal to the tooth face width, b.

$$\sigma_H = 0.629 \cdot 0.418s\sqrt{\frac{\frac{F_t}{cos\alpha}E(\frac{1}{R_1}+\frac{1}{R_2})\frac{1}{sin\alpha}}{b}} \leq \frac{Rp0{,}2}{Cs_H} \tag{3.46}$$

$F_t$ is the tangential force acting on the tooth,assuming that all three satellites are in contact, it is calculated as:

$$F_t = \frac{2T}{d \cdot n_s} \tag{3.47}$$

it has been verified that the safety factor $C_{SH}$ is greater than 1.5 for each pair of meshing wheels.

### 3.4.3 Verification of tooth bending resistance

For the verification of toothed wheels in bending the Standard ISO 6336-3 procedure was followed.

$$\sigma_F \leq \sigma_{F,amm} \tag{3.48}$$

where:

- $\sigma_F$ is the stress equivalent to the tooth root;

$$\sigma_F = \frac{F_t}{b \cdot m_n} \cdot y_{fs} \cdot y_\epsilon \cdot y_\beta \cdot (K_A \cdot K_V \cdot K_{F\beta} \cdot K_{F\alpha}) \tag{3.49}$$

- $\sigma_{F,amm}$ is the admissible stress.

$$\sigma_{F,amm} = \frac{\sigma_{D-1} \cdot y_{st} \cdot y_{NT} \cdot y_{\delta relT} \cdot y_{RrelT} \cdot y_x}{S_{Fmin}} \tag{3.50}$$

The factors appearing in the formulas take into account the tooth shape, tooth thickness, testing conditions, sensitivity to pitting, and surface roughness. They have been calculated according to the regulations. In this case as well, it has been verified that the safety factor for all gears in the reducer is greater than 1.5.

### 3.4.4 Verification of resistance to pitting corrosion

The pitting fatigue resistance condition is:

$$\sigma_H \leq \sigma_{HP} \tag{3.51}$$

where:

- $\sigma_H$ is the contact stress

$$\sigma_H = Z_H \cdot Z_E \cdot Z_\epsilon \cdot \sqrt{\frac{F_t}{d \cdot b} \frac{u+1}{u}} \cdot \sqrt{K_A \cdot K_V \cdot K_{F\beta} \cdot K_{F\alpha}} \tag{3.52}$$

- $\sigma_{HP}$ is the admissible contact stress.

$$\sigma_{HP} = \frac{\sigma_{H,lim} \cdot z_N}{S_H} \cdot z_L \cdot z_R \cdot z_V \cdot z_w \cdot z_X \tag{3.53}$$

The factors appearing in the formulas take into account the load distribution, material elasticity, gear ratio, contact ratio, dimensions, hardness, surface roughness, speed, and lubricant. They have been calculated according to the regulations. In this case as well, it has been verified that the safety factor for all gears in the reducer is greater than 1.5.

### 3.4.5 Sizing of the shafts

One proceeds with shafts sizing, which involves selecting a shaft diameter that is larger than the minimum required diameter and estimating its length.

$$D_{min} = \left( \frac{32}{\pi \sigma_{amm}} \sqrt{M_f^2 + M_t^2} \right)^{1/3} \tag{3.54}$$

In the case of the primary stage solar gear shaft, the carrier/secondary stage solar shaft , the output shaft and the roller screw shaft,the moment in the equation corresponds to the transmitted torque. However, when it comes to the moment on the satellite shaft, it is calculated as the sum of the inertia actions under stationary conditions $F_i$ and the force acting due to gear engagement R.

$$F_i = m \cdot \Omega_p^2 \cdot \frac{r_1 + r_2}{2} \tag{3.55}$$

$$R = 2F_t \tag{3.56}$$

The following table shows the results found.

| Outputs of shafts sizing | |
|---|---|
| Solar shaft diameter (first stage) | 12 [mm] |
| Solar shaft length (first stage) | 40 [mm] |
| Planet shaft diameter (first stage) | 11 [mm] |
| Planet shaft length (first stage) | 8 [mm] |
| Carrier shaft diameter | 23 [mm] |
| Carrier shaft length | 30 [mm] |
| Planet shaft diameter (second stage) | 14 [mm] |
| Planet shaft length (second stage) | 15 [mm] |
| Output shaft diameter | 33[mm] |
| Output shaft length | 30 [mm] |
| Screw shaft diameter | 33 [mm] |
| Screw shaft length | 50 [mm] |

**Table 3.8:** Geometric parameters

### 3.4.6 Calculation of the masses and the moments of inertia the gearbox components.

Finally, as the last step of the gearbox sizing, the masses and moments of inertia of all its components have been calculated. For mass calculations, the components are considered as cylinders, and the density $\rho$ is assumed to be 7850 kg/$m^3$. Specifically, the gears are treated as cylinders with a diameter equal to the pitch diameter and a height equal to the face width.

$$m = \pi \cdot L \cdot \left(\frac{d}{2}\right)^2 \cdot \rho \tag{3.57}$$

Since all bodies are considered as cylinders, the following formula applies:

$$I_z = m\frac{r^2}{2} \tag{3.58}$$

The inertia of the carrier is instead calculated using the following formula:

$$J_p = \frac{2\pi k n_s}{256 t_1^2}\rho b d_1^2 (d_1 + d_3)^2 \tag{3.59}$$

The following table shows the values of the masses and of the moments of inertia of all components of the gearbox.

| Mass of components | |
|---|---|
| Mass of the first stage solar shaft | 0.036 [kg] |
| Mass of the first stage solar | 0.097 [kg] |
| Mass of the first stage planets | 0.387 [kg] |
| Mass of the carrier shaft | 0.098 [kg] |
| Mass of the second stage solar | 1.498 [kg] |
| Mass of the second stage planets | 0.375 [kg] |
| Mass of the output shaft | 0.201 [kg] |
| Mass of the pinion | 2.360 [kg] |
| Mass of the gear | 2.360 [kg] |
| Mass of the connecting shaft | 0.336 [kg] |
| Total mass of the gearbox | 9.269 [kg] |
| Inertia of components | |
| Inertia of the first stage solar shaft | $6.39 \cdot 10^{-7}$ [kg$m^2$] |
| Inertia of the first stage solar | $9.47 \cdot 10^{-6}$ [kg$m^2$] |
| Inertia of the first stage planets | $1.52 \cdot 10^{-4}$ [kg$m^2$] |
| Inertia of the first stage carrier | $1.60 \cdot 10^{-4}$ [kg$m^2$] |
| Inertia of the carrier shaft | $6.47 \cdot 10^{-6}$ [kg$m^2$] |
| Inertia of the second stage solar | $1.52 \cdot 10^{-3}$ [kg$m^2$] |
| Inertia of the second stage planets | $9.48 \cdot 10^{-5}$ [kg$m^2$] |
| Inertia of the second stage carrier | $6.40 \cdot 10^{-3}$ [kg$m^2$] |
| Inertia of the output shaft | $2.74 \cdot 10^{-5}$ [kg$m^2$] |
| Inertia of the pinion | $2.26 \cdot 10^{-3}$ [kg$m^2$] |
| Inertia of the gear | $4.57 \cdot 10^{-5}$ [kg$m^2$] |
| Inertia of the connecting shaft | $2.26 \cdot 10^{-3}$ [kg$m^2$] |

**Table 3.9:** Mass and inertia of the gearbox components.

## 3.5 Sizing and choice of the electric motor

Servo systems utilize different types of electric motors to convert electrical power into mechanical power. These motors can be classified based on the type of electrical power they use (direct current, DC, or alternating current, AC) and the technology responsible for power conversion. DC motors can further be categorized as motors with brushes and brushless DC motors. Motors with brushes can be divided into separately excited, excited series, or permanent magnet motors. On the other hand, AC motors can be classified as synchronous motors (brushless AC, reluctance variation, or stepper type) or asynchronous induction motors, which can be further divided into wound rotor or squirrel-cage motors.

The most commonly used motor classes in servo systems are DC motors with brushes and brushless motors (DC or AC). DC motors with brushes operate based on the interaction between a stationary magnetic field generated by alternating salient poles at the stator and electrical windings integrated into the rotor. These windings are connected to the power supply through a collector and brush system, ensuring that the current circulating in the windings maintains a consistent polarity with the magnetic field generated by the stator, regardless of the rotor's position. This principle allows for continuous relative movement between the motor elements. Stator pole pairs are obtained through electric windings or permanent magnets, with the use of permanent magnet motors being preferred in servo systems due to their compactness and reduced susceptibility to short-circuit phenomena.

Despite their simplicity, DC motors with brushes have several drawbacks due to the brush and collector system required for their operation. Brushes experience wear and tear, degrade over time, can generate sparks near flammable materials, and increase the motor's axial size, making them unsuitable for applications with space limitations. Therefore, high-performance servo systems often employ brushless motors, which use suitable power electronics to switch currents according to the rotor's position, eliminating the need for brushes and collectors. Brushless motors only have electrical windings on the stator, while permanent magnets are attached to the rotor, resulting in extremely compact and lightweight motors. The absence of a commutator reduces the motor's length, providing higher rotor stiffness for increased speed required in servo applications. Heat conduction through the motor frame is also improved, allowing for higher electric loading, specific torque, and efficiency.

In the context of flight control applications, compact motors with high power density and acceleration capacity are required, which is why brushless motors are often chosen. These motors offer the desired characteristics for flight control systems

Brushless motors can further be classified based on the waveform of their current or back electromotive forces (back EMF): sinusoidal and trapezoidal. The

trapezoidal type is known as a permanent magnet Brushless DC (BLDC) motor, while the sinusoidal type is referred to as a Permanent Magnet Synchronous Motor (PMSM) or Permanent Magnet Brushless AC Motor.

Brushless DC Motors, also known as BLDC motors, are motors that operate with multiple phases. While conceptually similar to permanent magnet synchronous machines, they differ in flux distributions and back-emf profiles. The "DC" in their name refers to the control strategy employed, known as trapezoidal control. These motors are fed with direct currents, and at any given moment, only two phases are active, with each phase having a 120-degree phase difference relative to the others. Changes in the current state occur every 60 degrees. Each winding occupies 60 electrical degrees along the inner periphery of the stator, offset by 120 electrical degrees, corresponding to the number of polar pairs detectable on the rotor. The back electromotive forces generated by these motors exhibit a trapezoidal behavior, influenced by the spatial distribution of the magnetic induction vector B( $\theta_{el}$) generated by the permanent magnets integrated into the rotor.

Although called "brushless DC motors," this motor class requires a three-phase inverter to manage the power supply to each winding based on the rotor's angular position. Unlike a permanent magnet synchronous motor (PMSM), where the stator flux position varies continuously, a brushless DC motor commutates the stator flux position every 60 degrees. To accurately switch the current at the right moment, a Hall effect sensor is commonly used in BLDC motors to determine the rotor's position.

Brushless AC Motors (BLAC), or Permanent Magnet Synchronous Motors (PMSM), represent a high-performance motor class and can be seen as an evolution of brushless DC motors. The stator windings in BLAC motors are wound to approximate a sinusoidal spatial distribution. To generate a constant torque with rotor rotation, the stator's magnetic field must synchronize with the rotor. These motors employ three-phase windings, fed with balanced currents, to generate a rotating magnetic field. In sinusoidal brushless motors, the induced electromotive force (emf) in each winding phase should be a sinusoidal function of the rotor angle. Current transducers determine the instantaneous position of the stator magnetomotive force, while a resolver mounted on the motor shaft provides the rotor's angular position, serving as both a position and speed sensor.

While the power electronics used in both BLDC motors and PMSMs are the same (consisting of Pulse Width Modulation [PWM] and an inverter), the control strategies differ. Various techniques can be employed to control PMSMs, with the most popular being Field Oriented Control (FOC) and Direct Torque Control (DTC). Both methods decouple torque control from flux control during transient and steady-state conditions, but they differ in their time response. DTC offers a quicker response for torque step transients compared to FOC, while both control strategies track speed step variations in a similar manner. However, DTC is characterized by

higher flux, current, and torque ripple, resulting in increased audible noise at low speeds. In terms of steady-state behavior, FOC is considered superior to DTC, and it enables performance improvements by acting on both current and speed control loops. BLDC motors offer reliability and a simple and cost-effective control strategy compared to PMSMs, which require complex vector control methods. However, BLDC motors have lower power density, efficiency, and torque regularity. They exhibit significant torque ripple during phase commutation when an active switch changes. In this thesis, a PMSM motor with FOC control has been selected, despite the need for more advanced control techniques, due to the critical importance of torque density and delivery accuracy in this specific application. The chosen motor consists of three phases that are nominally electrically identical. These phases allow for the introduction of three magnetic axes, denoted as a, b, and c, with a 120° electrical offset between them, corresponding to the three phases (a, b, c). However, in this initial stage of sizing and linear modeling, it has been decided to treat the motor as a single-phase model. The complete three-phase model of the motor will be discussed later in the text. The motor was chosen to provide the required torque for the screw mechanism and to be capable of reaching the necessary speed within a suitable time interval. It has been decided to opt for one of the frameless KBM motors from the manufacturer Kollmorgen. The suitable models from the KBM series are brushless motors designed to provide high performance, long durability, extremely smooth rotation with minimal cogging, a wide range of operating speeds, and rapid acceleration. Specifically, the KBM-17X04 model with D-240 Vac winding has been chosen. All its characteristics,obtained from Kollmorgan catalog [6],are summarised in Table 3.10.

| KBM-17X04 model with D winding-240 Vac | |
|---|---|
| Motor Resistance Rm | 0.94 [Ω] |
| Motor Inductance Lm | 0.0038 [H] |
| Torque Sensitivity kt | 0.661 [Nm/Arms] |
| Back EMF constant ke [1] | 69.28[Vrms/krpm] |
| Thermal Resistance Rth | 0.65 [°C/W] |
| Continuous Stall Torque at 25°C amb. Tscont | 5.9 [Nm] |
| Continuous current Ic | 9.56 [Arms] |
| Peak Stall Torque Tmax | 24 [Nm] |
| Peak Current ip | 44 [Arms] |
| Speed at Rated Power | 5000 [rpm] |
| Maximum Mechanical Speed $\omega_{max}$ | 6000 [rpm] |
| Viscous Damping $c_m$ | $1.89 \cdot 10^{-4}$ [Nms/rad] |
| Max Static Friction Torque $T_{fr}$ | 0.165 [Nm] |
| Number of poles | 10 |
| Electric motor drive efficiency $\eta_{md}$ | 0.9 |
| Weight $m_r$ | 3.62 [kg] |
| Inertia $J_m$ | $2.4 \cdot 10^{-4}$ $[kgm^2]$ |

**Table 3.10:** : Characteristics of the motor chosen.

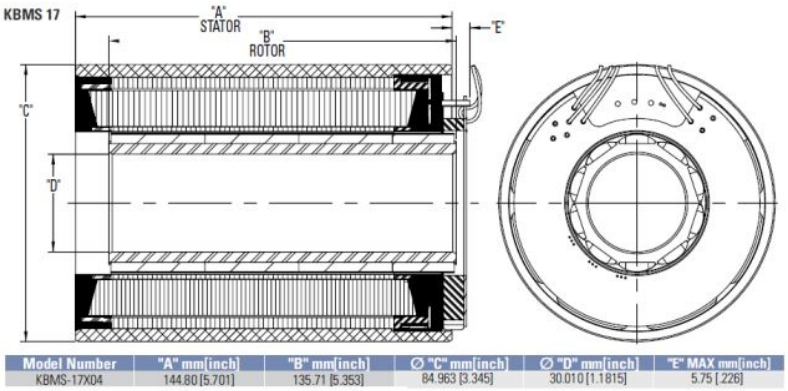


**Figure 3.6:** Dimensions of the Kollmorgen motor KBM 17x04 model **[6].**

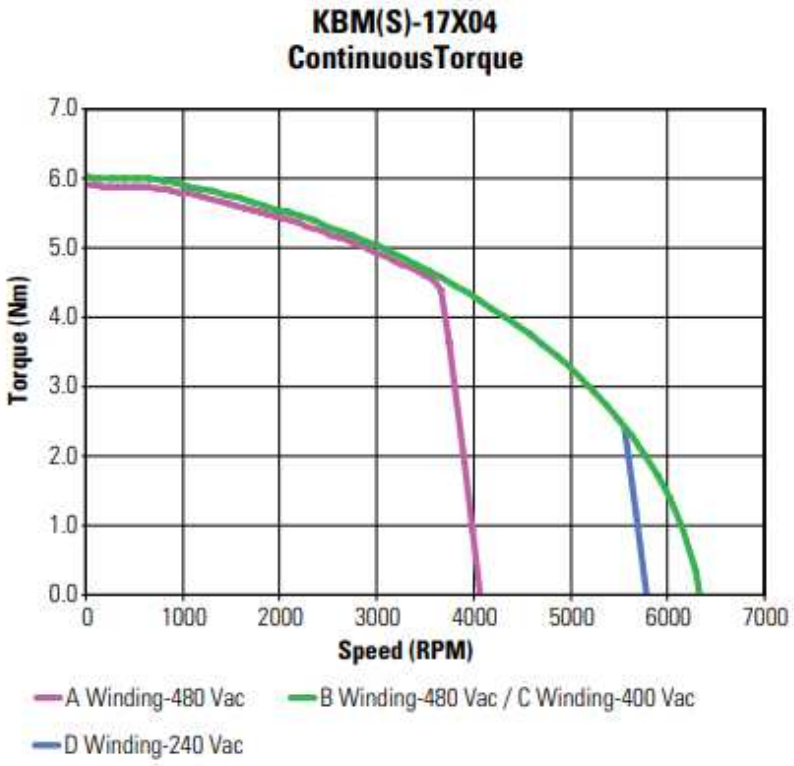


**Figure 3.7:** KBM 17 performance curve [6].

## 3.6 Transducers

In addition to the elements already discussed, the system requires an appropriate number of sensors to monitor the system's behaviour. The physical quantities to be measured by sensors are the angular position of the screw, the rotational speed of the motor and the current flowing in the stator windings. As far as current is concerned, a current sensor is required, i.e. a device that detects the electric current in the windings and generates a signal proportional to it. For reading the screw angular position a RVDT was used . A resolver is used instead to read the angular position of the motor and its relative angular velocity.

[1]Table 3.10 shows the back EMF constant value for all phases and no longer for the individual phase as was stated in the catalogue. To do this, it was necessary to multiply the value in the catalogue by 3

*Resolver*

A resolver is a type of rotary electrical transformer in which the energy flowing through its windings varies sinusoidally as the shaft rotates. It comprises a primary winding, known as the reference winding, and two secondary windings, the SIN and COS windings. The reference winding is located in the resolver's rotor, while the SIN and COS windings are situated in the stator, mechanically displaced 90 degrees from each other. In a brushless resolver, energy is supplied to the reference winding through a rotary transformer, eliminating the need for brushes and slip rings, thereby enhancing reliability. In resolver operation, the shaft angle ($\theta$) can be determined by measuring the signals induced in the secondary windings after injecting an AC voltage signal (Vr) into the primary winding. When the primary winding is excited by an AC voltage (Vr) through a rotary transformer, the induced voltages in the secondary windings vary depending on the rotor shaft angle $\theta$. These induced voltages exhibit variations corresponding to the sine and cosine of the rotor angle, respectively. By employing an arctangent function on these signals, the absolute angle $\theta$ of the rotor connected to the shaft can be determined. To facilitate resolver excitation and convert the resolver's angular analog signals into a digital format for ease of use by digital controllers, a resolver-to-digital converter is commonly employed. This converter simplifies the resolver's operation and allows for seamless integration with digital systems. Resolvers are robust devices capable of providing reliable performance even in high-temperature, vibration, and contaminated environments. However, they are more expensive than other alternatives and require complex excitation and signal processing circuits, which can be susceptible to noise.

In this specific case, a brushless resolver from Tamagawa Seiki Co was chosen, and its characteristics are provided below.

| Resolver brushless, BRX-TS2605N1E64 size 08 Tamagawa Seiki Co. manufacturer [7] | |
|---|---|
| Input voltage | 7 [Vrms] |
| Input frequency | 10 [kHz] |
| Residual voltage | 20 [mVrms] |
| Transformation ratio | 0.50 ± 5 % |
| Electrical error | ± 10° |
| Phase shift | +10° |
| Input impedance | 140 $\omega$ ± 20 % |
| Output impedance | 120 $\omega$ ± 20 % |

**Table 3.11:** Resolver parameters.

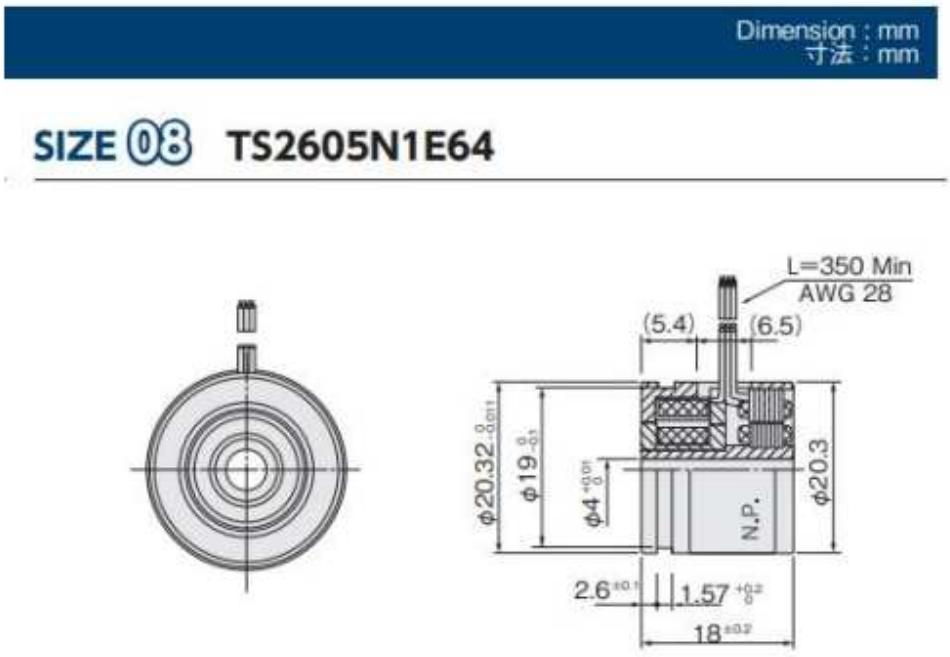


**Figure 3.8:** Dimensions of the Resolver brushless, BRX-TS2605N1E64 [7].

*RVDT*

An RVDT, which stands for Rotary Variable Differential Transformer, is a type of sensor used to measure angular position. It operates based on the principle of electromagnetic induction and consists of a primary winding and two secondary windings.

The primary winding is excited with an AC voltage signal, generating a magnetic field. The secondary windings are located on either side of the primary winding and are connected in series opposition. As the rotary shaft connected to the RVDT rotates, it causes a change in the magnetic coupling between the primary and secondary windings.

The relative position of the shaft with respect to the RVDT determines the voltage induced in the secondary windings. When the shaft is in the null or zero position, the induced voltages in the two secondary windings are equal and opposite, resulting in a net voltage of zero. As the shaft rotates away from the null position, the induced voltages in the secondary windings become unequal, producing a net voltage output proportional to the angular displacement.

By measuring the amplitude and phase of the output voltage, the angular position of the shaft can be determined. This measurement is typically performed using signal conditioning circuits and analog-to-digital converters to convert the analog voltage into a digital format for further processing by control systems or microcontrollers.

RVDTs are widely used in various applications that require accurate and reliable angular position measurement. They offer advantages such as high precision, linearity, and repeatability. RVDTs are particularly suitable for applications where a continuous rotation range needs to be measured and where high immunity to environmental factors such as temperature, vibration, and electromagnetic interference is required.

Overall, the RVDT provides a robust and effective means of measuring angular position in a wide range of industrial and scientific applications

The following tables and figures show the chosen RVDT and its parameters.

| RVDT - AC - differential, R30A Althen manufacturer [8] | |
|---|---|
| Angular range | ± 30° |
| Non linearity | 0.25 % |
| Output at range ends | 87 [mV/V] |
| Sensitivity | 2.9 [mv/V/degree] |
| Input voltage | 3 [VRMS] |
| Input frequency | 10 [kHz] |

**Table 3.12:** RVDT parameters.

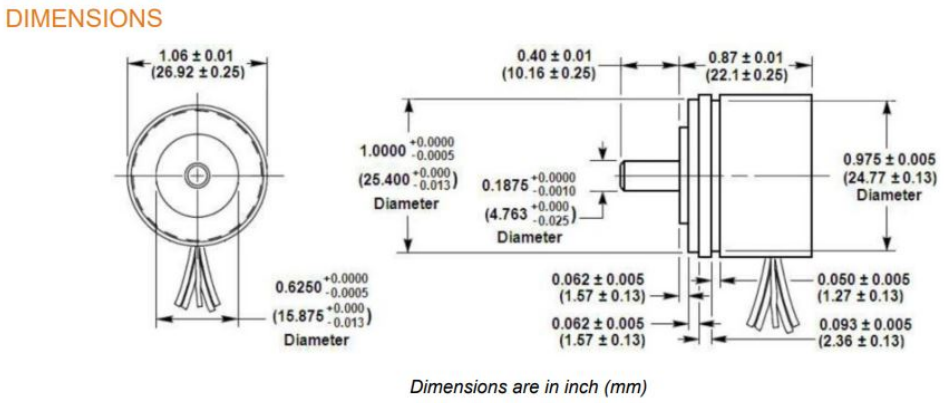


**Figure 3.9:** Dimensions of the RVDT - AC - differential, R30A [8].

### 3.6.1 Sizing of the Gearbox (RVDT)

Using a reducer in conjunction with an RVDT can have several advantages. Firstly, it can help increase the resolution of measurements. Sometimes, the rotation we want to measure may be happening really fast or covering a wide range. In such cases, employing a reducer allows us to reduce the rotational speed, enabling the RVDT to provide more precise measurements of the angle or rotation. Secondly, a reducer allows us to adjust the speed to better match the RVDT's specifications. Sometimes, the rotational speed of the object we want to measure may be either too high or too low for the RVDT to work optimally. By incorporating a reducer, we can fine-tune the rotational speed to ensure that the RVDT operates within its desired range, resulting in better functioning and more accurate measurements. It's important to keep in mind that using a reducer may introduce certain considerations. For instance, there might be an increase in friction, which can affect the overall performance, or there could be some loss of precision. In summary, by utilizing a reducer alongside an RVDT, we can achieve higher resolution, increased torque, and adjust the rotational speed to optimize measurements.

Similarly to what has been done previously, the RVDT gearbox was sized. In this case, the used structure is composed of an ordinary gearbox, followed by a two stage planetary gearbox.

The chosen material is the 40NiCrMo7 and its properties are summarized in table 3.5.

The formulas ,the verifications and the sizing steps are the same as in the previous case; therefore, only the obtained results will be provided.

| Assumed parameters | |
|---|---|
| First stage gear ratio (carried stopped) i1 | -6.25 |
| Second stage gear ratio(carried stopped) i2 | -15 |
| Number of teeth on pinion z9 | 40 |
| Number of teeth on sun gear (first stage) z11 | 40 |
| Number of teeth on sun gear (second stage) z14 | 18 |

**Table 3.13:** Assumed Parameters RVDT gearbox

The transmission ratio $\tau$ required was calculated using the equation:

$$\tau = \frac{360 \cdot \theta_{screw}}{span} \qquad where\ span = 2 \cdot angular\ range \tag{3.60}$$

The transmission ratio of the ordinary gearbox $\tau_r$ was assumed equal to 1.5 , so the planetary gearbox transmission ratio $\tau_e$ can be defined as:

$$\tau_e = \frac{\tau}{\tau_r} \tag{3.61}$$

According to Equations from 3.4.1 to 3.4.1 the sizing results summarized in Table 3.14 have been estimated.

| Sizing results | | | | | | | | | | | |
|---|---|---|---|---|---|---|---|---|---|---|---|
| z9 | 40 | d9 | 20[mm] | d9b | 18.8[mm] | z13 | 250 | d13 | 75[mm] | d13b | 70.5 [mm] |
| z10 | 60 | d2 | 30[mm] | d2b | 28.2[mm] | z14 | 18 | d14 | 5.4[mm] | d14b | 5.1[mm] |
| z11 | 40 | d11 | 12[mm] | d11b | 11.3[mm] | z15 | 126 | d15 | 37.8[mm] | d7b | 35.5[mm] |
| z12 | 105 | d12 | 31.5[mm] | d12b | 29.6[mm] | z16 | 270 | d16 | 81[mm] | d8b | 76.1[mm] |
| normal modulus of the ordinary gearbox wheels $m_n$ | | | | | | | | | 0.5 [mm] | | |
| normal modulus of the first stage wheels $m_{n1st}$ | | | | | | | | | 0.3 [mm] | | |
| normal modulus of the second stage wheels $m_{n2st}$ | | | | | | | | | 0.3 [mm] | | |
| Face width b9=b10 | | | | | | | | | 5 [mm] | | |
| Face width b11=b12=b13 | | | | | | | | | 3 [mm] | | |
| Face width b14=b15=b16 | | | | | | | | | 3 mm] | | |
| First stage gear ratio $\tau 1$ | | | | | | | | | 7.25 | | |
| Second stage gear ratio $\tau 2$ | | | | | | | | | 16 | | |
| Contact ratio $\epsilon_{9/10}$ | | | | | | | | | 1.52 | | |
| Contact ratio $\epsilon_{11/12}$ | | | | | | | | | 1.55 | | |
| Contact ratio $\epsilon_{12/13}$ | | | | | | | | | 1.66 | | |
| Contact ratio $\epsilon_{14/15}$ | | | | | | | | | 1.47 | | |
| Contact ratio $\epsilon_{15/16}$ | | | | | | | | | 1.67 | | |

**Table 3.14:** Gearbox RVDT sizing

As regards the torques acting on the wheels, the torque T9 acting on pinion was assumed equal to:

$$T9 = \frac{friction\ torque\ RVDT}{\tau} \tag{3.62}$$

The torque acting on the first stage solar and the torque acting on the second stage solar have been calculated withe the formulas below:

$$T11 = T9 \cdot \tau_r \tag{3.63}$$

$$T4 = T11 \cdot \tau_1 \tag{3.64}$$

## 3.7 The main outputs of the preliminary sizing

The following table shows the masses of all components

| Mass of components | |
|---|---|
| Mass of the screw mechanism | 20.62 [kg] |
| Mass of the thrust ball bearings | 0.11 [kg] |
| Mass of the gearbox | 8.808 [kg] |
| Mass of the electric motor | 3.720 [kg] |
| Mass of the RVDT reducer | 0.197 [kg] |
| Mass of the transducers | 0.066 [kg] |
| Total mass of the actuator | 33.52 [kg] |

**Table 3.15:** Mass of components

At the end of these preliminary calculations, which allowed the definition of all the geometric, according to Equations from 3.65 to 3.71 the approximate [2] volumes of main components have been estimated.

$$V_{screw\ mechanism} = V_{screw} + V_{nut} \tag{3.65}$$

$$V_{screw} = \pi \cdot L \cdot \left(\frac{d0}{2}\right)^2 \tag{3.66}$$

$$V_{nut} = \pi \cdot L \cdot \left(\left(\frac{D1}{2}\right)^2 - \left(\frac{d0}{2}\right)^2\right) \tag{3.67}$$

$$V_{resolver} = V_{bearings} = \pi \cdot L \cdot \left(\left(\frac{D}{2}\right)^2 - \left(\frac{d}{2}\right)^2\right) \tag{3.68}$$

$$V_{RVDT\ gearbox} = V_{gearbox} = \sum_{i=1}^{n} V_{shaft} + \sum_{i=1}^{m} V_{gear} \tag{3.69}$$

$$V_{RVDT} = V_{gear} = V_{shaft} = \pi \cdot L \cdot \left(\frac{D}{2}\right)^2 \tag{3.70}$$

$$V_{elctric\ motor} = \pi \cdot A \cdot \left(\left(\frac{C}{2}\right)^2 - \left(\frac{D}{2}\right)^2\right) \tag{3.71}$$

[2]The components are approximated with simple geometric figures

| Volume of components | |
|---|---|
| Volume of the screw mechanism | $2.63 \cdot 10^3$ $[cm^3]$ |
| Volume of the thrust ball bearings | $1.87 \cdot 10^1$ $[cm^3]$ |
| Volume of the gearbox | $1.12 \cdot 10^3$ $[cm^3]$ |
| Volume of the electric motor | $7.19 \cdot 10^2$ $[cm^3]$ |
| Volume of the RVDT reducer | $1.91 \cdot 10^1$ $[cm^3]$ |
| Volume of the transducers | $1.63 \cdot 10^1$ $[cm^3]$ |

**Table 3.16:** Volume of components

# Chapter 4

# Study of the behavior of the system for different operating conditions

After completing the design process, the behavior of the system was studied under different operating conditions, specifically varying temperature and the number of actuators in operation. For each analyzed condition, a thermal verification was performed by calculating the temperature rise, and the electrical power absorbed by the flap was calculated.

- **CASE 1** : *Operation under normal conditions-both actuators working-[40°C]*

  In the case where both actuators are functioning, the axial load on each actuator is equal to half of the maximum applied load. Therefore, the electrical power absorbed by the flap is calculated by summing up the electrical power absorbed by the two actuators. Here, we provide the calculation for a single actuator, as the same procedure applies to the other one. The electrical power absorbed is equal to the electrical power required by the motor divided by its efficiency.

$$W_{flap} = W_{tot1} + W_{tot2} \tag{4.1}$$

$$W_{tot} = \frac{W}{\eta_{md}} \tag{4.2}$$

$$W = V_M i \tag{4.3}$$

$$V_M = Ri + k_e \omega_M \tag{4.4}$$

$$i = T_{em}/k_t \tag{4.5}$$

· Required electromagnetic torque:

$$T_{em} = T_{g,in1} + c_m\omega_m + T_{fms} \tag{4.6}$$

$$\omega_m = \omega_{rs} \cdot \tau \tag{4.7}$$

$$\omega_{rs} = \frac{2\pi V_N}{p} \tag{4.8}$$

· Torque required at first stage input

$$T_{g,in1} = \frac{T_{g,in2}}{\eta_{1/p} \cdot \tau_1} + T_{drag,g,1} + c_{g,1} \cdot (\omega_{rs}\tau)^2 \tag{4.9}$$

where:

- $\eta_{md}$, R, $k_e$, $k_t$, $c_m$, $T_{fms}$; These are parameters of the selected electric motor (as shown in the table 3.10).
- The values of the various transmission ratios $\tau$ are derived from the sizing of the reduction chain.

Regarding the calculation of the required output and input torques for the two stages of the reducer, it is necessary to refer to the calculation of its dissipative contributions.

· Torque required at first stage input:

$$T_{g,in1} = \frac{T_{g,in2}}{\eta_{1/p} \cdot \tau_1} + T_{drag,g,1} + c_{g,1} \cdot (\omega_{rs}\tau_{tot})^2 \tag{4.10}$$

· Torque required at second stage input:

$$T_{g,in2} = \frac{T_{g,out2}}{\eta_{2/p} \cdot \tau_2} + T_{drag,g,2} + c_{g,2} \cdot (\omega_{rs}\tau_2)^2 \tag{4.11}$$

· Torque required at second stage output:

$$T_{g,out2} = \frac{T_{rs} + T_{in,RVDT}}{\eta_{6/7} \cdot \tau_{6/7}} + T_{drag,3} + c_{g,3} \cdot (\omega_{rs}\tau_{6/7})^2 \tag{4.12}$$

· Screw input torque:

$$T_{rs} = \frac{F_N p}{2\pi\eta_{dr}} T_{rs,p} \tag{4.13}$$

· Total passive linear actuator torque:

$$T_{rs,p} = T_V + T_{seal} + T_{tb,drag} + c_{tb} \cdot \omega_{rs} \tag{4.14}$$

· Torque required by RVDT:

$$T_{in,RVDT} = \frac{T}{\eta_{g,rvdt}} + T_{d,gear} + c_s \cdot \omega_{rs} \tag{4.15}$$

Below are the formulas for calculating the dissipative contributions of the reducer for the first stage:

· Direct meshing efficiency:

$$\eta_{1/p} = r_{1/p}\left[1 + \left(\frac{1}{r_{1/p}} - 1\right)\eta_{1/3}\right] \tag{4.16}$$

· Speed Ratio:

$$r_{1/p} = \frac{1}{1 - i_1} \tag{4.17}$$

· Direct efficiency 1->3:

$$\eta_{1/3} = \eta_{1/2} \cdot \eta_{2/3} \tag{4.18}$$

· Direct efficiency 1->3:

$$\eta_{1,2} = 1 - k_f \cdot \left(\frac{1}{z_1} + \frac{1}{z_2}\right) \tag{4.19}$$

$k_f$ is loss factor between 0.20 and 0.35.

· Drag torque (reported to motor shaft):

$$T_{drag,g,1} = k_{TL} m z_1 + k_{TL} m z_2 \left(\frac{z_1}{z_2}\right) \cdot n_s \tag{4.20}$$

$k_{TL}$ is mechanical loss factor usually between $5 \cdot 10^{-4}$ and $2 \cdot 10^{-3}$ .

· Coefficient of losses related to speed:

$$c_s = k_s \left(d_1^2 + n_s \left(\frac{z_1}{z_2}\right)^3 d_2^2\right) \tag{4.21}$$

$k_s$ is a speed-related losses parameter usually between $2 \cdot 10^{-10}$ and $5 \cdot 10^{-3}$ .

Finally, a thermal verification is conducted by checking the temperature rise.

$$\Delta T = \frac{W_j t_{op}}{m_r c} \tag{4.22}$$

· Heat power:

$$W_j = Ri^2 \tag{4.23}$$

$t_{op}$ is the advancement time,that is a sizing specification, $m_r$ is the mass of the motor ,while c is the specific heat of copper.

The formulas for the subsequently analyzed cases remain the same as those just presented, with only the operating conditions being different.

- **CASE 2**:*Operation under normal conditions-only one working actuator-[40°C]*

  In this case, only one actuator is considered to be operational. The only difference from the previous case is the calculation of the axial load on the actuator.

  Axial load T = nominal torque + reverse torque of the other actuator + $c_s\ \omega_m^2$

- **CASE 3** : *Operation at low temperatures-both actuators working-[-54°C]*

  In the third analyzed case, both actuators are considered to be operational. However, a utilization temperature of -54°C is taken into account to verify the functioning at low temperatures. The calculation of the axial load on the actuator remains the same as in the first case. However, all the values of the dissipative contributions change since they depend on the temperature.

- **CASE 4** : *Operation at low temperatures- only one working actuator-[-54°C]*

  Finally, another case is considered where only one actuator is operational, and the operating temperature is set to -54 °C.In this case, the calculation of the axial load on the actuator remains the same as in the second case, while the dissipative parameters are the same as in the third case.

The following table presents the most significant findings from the study of the four examined cases:

| | CASE 1<br>40°C<br>2act | CASE 2<br>40°C<br>1act | CASE 3<br>-54°C<br>2act | CASE4<br>-54°C<br>1act |
|---|---|---|---|---|
| Supply voltage [V] | 105.16 | 108.72 | 105.2 | 109.51 |
| Temperature increase [°C] | 0.06 | 0.3 | 0.09 | 0.56 |
| Electrical power absorbed per flap [W] | 674.40 | 780.38 | 1050.79 | 2712.37 |

**Table 4.1:** Study of the behavior of the system for different operating conditions

Based on the obtained values, it is evident that Case 4 is the worst. Additionally, it is noticeable that transitioning from two functioning actuators to only one increases all three reported parameters. Furthermore, it is clear that decreasing the temperature results in a significant increase in the electrical power absorbed per flap. However, in all cases, the chosen motor is capable of providing the supply voltage.

## 4.1 Verification of reversibility conditions

The maximum torque that does not cause system reversibility is calculated by varying the force on the actuator until achieving zero torque on the motor (up to the fourth decimal place). It is an iterative process that follows the following logical flow:

1. The value of the load acting on the actuator is assumed.
2. The electromagnetic torque on the motor is calculated based on the assumed load.

$$T_{em} = T_M - T_{fms} \tag{4.24}$$

· Torque required at the motor shaft:

$$T_M = \frac{T_P - Td, gear, RVDT}{\tau_e} \cdot \eta_{g,rv} - Td, gear \tag{4.25}$$

where:

· Torque input to the nut:

$$T_P = \frac{F_n \cdot p}{2 \cdot \pi} \cdot \eta_{rv} - Mbe \tag{4.26}$$

Mbe is the resultant of the passive torques on the screw.

3. Return to step 1 until the value of $T_{em}$ is zero.

Below are the values of the reversibility torque found for the two considered temperatures.

In addition, the maximum tolerable torque has been calculated based on the maximum linear displacement and the maximum angular displacement.

$$C_{max} = \frac{F_N \cdot x_{max}}{\theta_{max}} \tag{4.27}$$

| | 40°C | -54°C |
|---|---|---|
| Reversibility torque $F_N$ [N] | 4173 | 5783 |
| Maximum tolerable torque $C_{max}$ [Nm] | 3962 | 5491 |

**Table 4.2:** Reversibility torque

## 4.2 Check of the stop and start conditions

In this phase, it is verified if the system has enough margin, in terms of engine torque, to move or stop everything downstream under the worst possible conditions. In both cases, the inertial load of the equivalent moving mass is added to the normal load on the actuator.

**Stop conditions**

For the stopping phase, when a deceleration is desired, we consider the worst-case conditions, where friction does not assist in stopping. In this case, we consider the condition of maximum efficiency.

An interval of deceleration $\delta_t$ (0.05 s) is hypothesized, based on which, knowing the motor angular velocity $\omega_m$ (equation 4.7) and linear velocity of the actuator v from the design specifications, the motor angular deceleration $\alpha$ and linear deceleration of the actuator $a$ are calculated.

$$\alpha = \frac{\omega_m}{\delta_t} = 4373[rad/s^2] \tag{4.28}$$

$$a = \frac{v}{\delta_t} = 11600[m/s^2] \tag{4.29}$$

Given the accelerations, it is possible to calculate the motor's inertia torque $T_{M,i}$, the inertia torque of the rotating parts referred to the motor shaft $T_i$, and the inertia force acting on the actuator $F_i$.

$$T_{M,i} = J_m \cdot \alpha \tag{4.30}$$

$$T_i = (J_{rs} + J_{gear} + J_{rvdt}) \cdot \alpha \tag{4.31}$$

$$F_i = m_{eq} \cdot a \tag{4.32}$$

As for the axial load on the actuator $F_N$, it is the sum of half of the maximum applied load and the newly calculated inertia force $F_i$. Once the inertia force has been calculated, the calculation procedure is similar to the one described in Case 1 analyzed at the beginning of Chapter 4.

$$W_{tot} = \frac{W}{\eta_{md}} \tag{4.33}$$

$$W = V_M i \tag{4.34}$$

$$V_M = Ri \tag{4.35}$$

$$i = T_{em}/k_t \tag{4.36}$$

· Required electromagnetic torque:

$$T_{em} = T_m - 1.3 \cdot T_{M,i} \tag{4.37}$$

· Torque required at the motor shaft:

$$T_m = \frac{T_{in}}{\tau} \cdot \eta_{g,rv} - T_{drag,} + T_{M,i} + T_i \tag{4.38}$$

· Input torque to the reducer:

$$T_{in} = T_p - T_{in,RVDT} \tag{4.39}$$

· Screw input torque:

$$T_p = F_N \frac{p}{2\pi} \cdot \eta_{rs} - M_{be} \tag{4.40}$$

where $M_{be}$ is the resulting passive roller screw torques.

· Torque required by RVDT:

$$T_{in,RVDT} = \frac{T}{\eta_{g,rvdt}} + T_{d,gear} \tag{4.41}$$

Finally, a thermal verification is conducted by checking the temperature rise.

$$\Delta T = \frac{W_j \delta_t}{m_r c} \tag{4.42}$$

· Heat power:

$$W_j = Ri^2 \tag{4.43}$$

**Start conditions**

For startup, the worst possible condition is at low temperatures, as friction is very high and efficiencies are greatly reduced, resulting in the loss of a significant portion of engine torque to friction.

Similarly to what was done in the case of stopping, one starts by assuming a range of acceleration. Next, the angular acceleration and linear acceleration are

calculated. Once these values are determined, the inertia forces and moments can be computed. The calculation of the axial force on the actuator is also the same.

The calculation proceeds in a similar manner to the previous case with some modifications, including the consideration that the operation is carried out at the minimum operating temperature of -54 °C.

Below are the formulas that vary compared to the previous case:

· Required electromagnetic torque:

$$T_{em} = T_m + T_{fms} \tag{4.44}$$

where $T_{fms}$ is the breakaway torque of the electric motor.

· Torque required at the motor shaft:

$$T_m = \frac{T_{in}}{\tau}\frac{1}{\eta_{g,d}} + T_{drag,} + T_{M,i} + T_i \tag{4.45}$$

· Input torque to the reducer:

$$T_{in} = T_p + T_{in,RVDT} \tag{4.46}$$

· Screw input torque:

$$T_p = F_N \frac{p}{2\pi} \cdot \eta_{rs} + M_{be} \tag{4.47}$$

In both cases, the required electrical power for each actuator has been calculated, along with the supply voltage, phase current, and temperature rise.

| | STOP | START |
|---|---|---|
| Supply voltage [V] | 3.25 | 21.55 |
| Phase current [A] | 4.64 | 30.79 |
| Temperature increase [°C] | 0.0005 | 0.0232 |
| Electrical power absorbed for flap [W] | 16.75 | 737.05 |

**Table 4.3:** Study of the behavior of the system stop and start conditions

Based on the obtained results, it is observed that in both cases, the temperature rise is not significant, and the motor meets the required supply voltage. Furthermore, it is noted that in the starting case, the phase current increases significantly but remains below the motor's maximum tolerated voltage.

# Chapter 5

# Linearised model for dynamic response

Up to this point, the sizing of an electro-mechanical actuator's architecture and components in a stable condition has been completed. The upcoming chapters will focus on the modeling of the actuator and the examination of its performance in a dynamic state.

When dealing with an actual system, it is advantageous to possess a mathematical representation that depicts its dynamic behavior. This is beneficial during the system's design phase for performance analysis and control purposes. Although real systems are generally non-linear, it is possible to describe them using a linear model that holds true under specific conditions. Hence, a non-linear system can be approximated as a linear system by employing linearization around an operating point. While modern computational tools enable numerical solutions of non-linear equations to obtain the system's complete dynamics, linear approximation remains a valuable approach. Utilizing a linearized model allows for the determination of suitable initial values for controller gains and immediate insights into the system.

Consequently, it was decided to initially develop a linearized model in the Excel® environment, followed by a high-fidelity model in the Matlab-Simulink® environment. Finally, a comparison will be made among the achieved results upon concluding the analysis.

## 5.1 Linear Modeling of Key System Components

A linear system is characterized by a transfer function that establishes a relationship between the system's input and output based on its own characteristics. To construct the linearized model, we derived mathematical equations that describe the behavior of each component in the system. Typically, ordinary differential equations with constant coefficients are used to analyze the dynamic response of linear systems in the time domain. However, the study of linear systems is often conducted in the frequency domain, where differential equations are transformed into algebraic equations. This transformation is achieved using various types of transforms, with the Laplace transform being commonly employed for system analysis. The Laplace transform is a linear operator that associates a function of a real variable (e.g., time) with a function of a complex variable known as "s." Once the desired algebraic equations are obtained, block diagrams and transfer functions of the system can be formulated. The transfer function represents the ratio of the output transform to the input transform, assuming zero initial conditions, and provides insights into the system's dynamic characteristics. Bode diagrams are used to graphically represent the transfer functions, showcasing the frequency response of linear time-invariant systems. To ensure stability, the controller gains were adjusted for each control loop.

The modeling process began by focusing on the main components of the system. We started with equations describing the electric motor's operation, which is the component closest to the pilot's control signal.

The linearized model considered a single-phase electric motor and referred to the equivalent circuit presented in Figure 5.1.

By solving the equivalent armature circuit, it is possible to derive the equation representing the electrical dynamics of the motor:

$$V_a = Ri + L\frac{di}{dt} + e_{in} \tag{5.1}$$

$$e_{in} = k_e\omega \tag{5.2}$$

where i is the current flowing in the windings, $k_e$ the voltage constant, $e_{in}$ the back-electromotive force, $\omega$ the angular velocity of the motor shaft and finally R and L the equivalent resistance and inductance of the motor respectively.

Then, to obtain the expression of the torque transmitted to the motor shaft, the Lorentz's law is invoked, which allows to write the equation:

$$T_m = k_t i \tag{5.3}$$

in which $k_t$ is the torque constant.

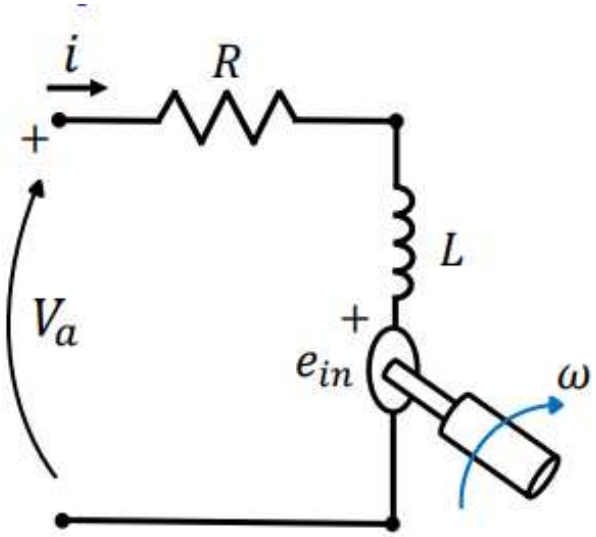


**Figure 5.1:** Equivalent circuit of the single-phase model of the electric motor

The motor's constitutive equations then make explicit the relationship between the supply voltage commanded by the control $V_a$ and the torque developed by the device $T_m$. By employing the Laplace transform on Equations (5.1) and (5.3), one can derive the set of equations that describe the motor's dynamics within a linear field.

$$\begin{cases} \overline{V_a} = (R + Ls)\bar{i} + k_e\overline{\omega} \\ \overline{T_m} = k_e\bar{i} \end{cases} \tag{5.4}$$

The relationship between the quantities relating to the screw mechanism and those relating to the electric motor is obtained by writing the equilibrium equation for the electric motor-screw transmission shaft.

$$T_m - T_r - I_m\dot{\omega} - \gamma\omega = 0 \tag{5.5}$$

where $\gamma$ is the motor viscous coefficient, $I_m$is the motor inertia and $T_r$ is the screw torque.

The Laplace transform applied to Equation (5.5) gives the algebraic equation which can be used to describe the dynamics of the transmission shaft in a linear field:

$$\overline{T_m} = \overline{T_r} + (I_m s + \gamma)\overline{\omega} \tag{5.6}$$

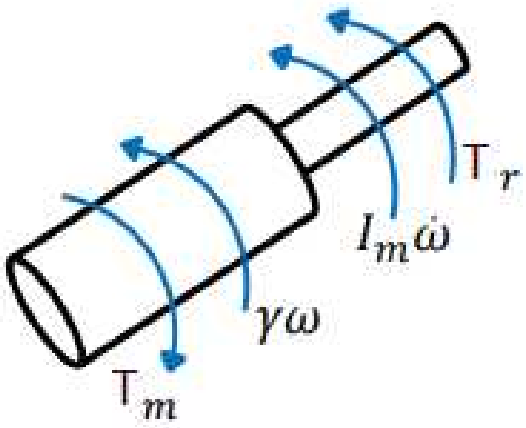


**Figure 5.2:** Equilibrium of the motor-screw transmission shaft

The kinematic relationship between the screw and nut contact yields the correlation between rotational and linear translation.

$$x = \frac{P}{2\pi}\theta \tag{5.7}$$

In the hypothesis that the motion reducer is not present, the resisting torque $T_r$ becomes the driving force of the screw. Assuming the neglect of the torsional stiffness of the screw and the distributed mass of the screw, the efficiency of the screw/nut system can be expressed as follows:

$$\eta = \frac{Pu}{Pe} = \frac{F_e\dot{x}}{C_r\omega} \tag{5.8}$$

$F_e$ is the external force acting on the nut in opposition to its velocity $\dot{x}$. Therefore, the resisting torque imposed by the external force disturbance $F_e$ can be derived using the following relationship:

$$T_r = \frac{P}{2\pi\eta}F_e \tag{5.9}$$

Having acquired a comprehensive understanding of the frequency domain equations pertaining to each component within the system, it becomes feasible to construct the block diagram. Nonetheless, for enhanced clarity, the follow equations present the restructured system of equations in a more convenient format, facilitating the visualization of the block diagram for the position-controlled electromechanical servo system, as illustrated in Figure 5.3.

$$\bar{i} = \frac{\frac{\overline{V_a}}{R} - \frac{k_e}{R}\overline{\omega}}{\frac{L}{r}s + 1} \tag{5.10}$$

$$\overline{T_m} = k_t \bar{i} \tag{5.11}$$

$$\overline{\omega} = \frac{\frac{\overline{T_m} - \overline{T_r}}{\gamma}}{\frac{I_m}{\gamma}s + 1} \tag{5.12}$$

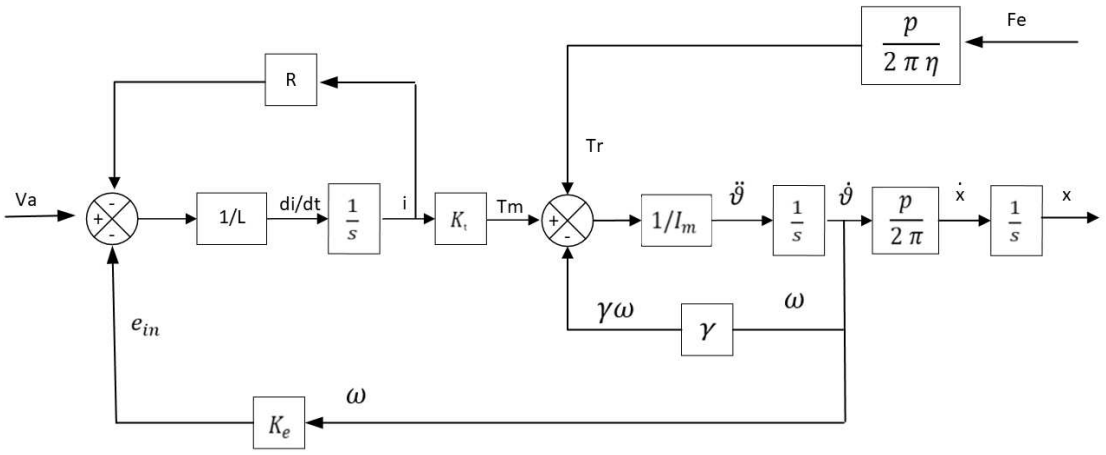


**Figure 5.3:** Block diagram of the actuation system without sensors and regulation system

## 5.2 Architecture of the control electronics and sensors used

The functioning of the system necessitates the presence of control electronics responsible for managing the control loops. Its main role involves handling the set and feedback signals originating from the system, as well as executing the control laws.

This electro-mechanical system incorporates three control loops, which consequently require the same number of physical quantities to be measured by sensors.The transmitters described in this thesis work were represented as a black box in both the linear and non-linear models. Specifically, the current transmitter was modeled as a zero-order system, the resolver was modeled as a first-order system, while the RVDT was modeled as a second-order system. Care was taken to select a bandwidth that was greater than the frequency of the measured phenomenon to prevent undesired attenuation in the frequency response. For each transmitter, a cut-off frequency ten times higher than the frequency of the measured phenomenon was chosen. Additionally, a typical value for the damping factor was selected for the RVDT. The values of these models are reported in the table

| Parameters of transmitters models | |
|---|---|
| Current gain $H_A$ | 1 [V/A] |
| Resolver gain $H_{RES}$ | 1 [V/(rad/s)] |
| Resolver time constant $t_H$ | 0.00008 [s/rad] |
| RVDT gain $H_L$ | 0.705 [V/rad] |
| RVDT natural pulse $\sigma_H$ | 1257 [rad/s] |
| RVDT damping factor $\zeta$ | 1 |

**Table 5.1:** Values of the current control loop parameters

The measured variable obtained from the sensors is then fed into the respective controller. The regulator, also known as the controller, is a component of the servo system that determines the behavior of the process or controlled variable. The control law is embedded within the regulator, with the objective of minimizing the error ($e$) between the desired variable ($set$) and the measured variable ($feedback$). This error represents the input variable for the compensator, which subsequently generates a reference signal ($Rif$) at the output.

In this specific case, three control loops have been implemented. Beginning from the outermost loop and progressing towards the innermost loop, we have:

- Position control loop: focusing on the position of the actuator;
- Speed control loop: targeting the rotational speed of the motor-screw;

- Current control loop: regulating the current flowing within the stator windings.

The compensated error resulting from the outermost loop becomes the control signal for the immediately innermost loop. This control strategy is known as nested loops control and offers various advantages, primarily the ability to respond to external disturbances by acting upon the innermost and faster dynamics of the servo system.

However, it's crucial to highlight that for effective nested-loop control, each control loop's bandwidth must increase from the outer loops towards the innermost loop. If the dynamics of the innermost loop were slower than those of the outermost loop, the system's response speed would be limited compared to its full potential.

A proportional-integral (PI) controller has been employed for each control loop. In this case, the control variable derived from the error between the set and feedback signals is determined by the sum of two components (as depicted in Figure 5.4):

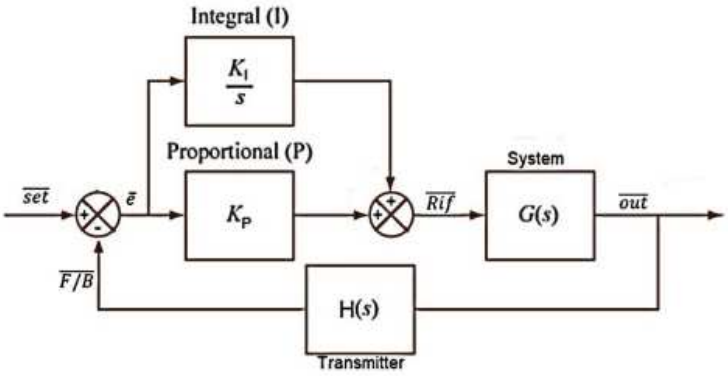


**Figure 5.4:** Scheme of a PI controller

- Proportional contribution: the reference is proportional to the error between the set and feedback signals;
- Integral contribution: the reference is proportional to the integral of the error, allowing for the elimination of steady-state error.

The inclusion of derivative action was deemed unnecessary and could potentially introduce instability, hence it was not considered.

Following these explanations, the complete block diagram, depicted in Figure 5.5, illustrates the various blocks of the system, with the control and transmitter blocks.

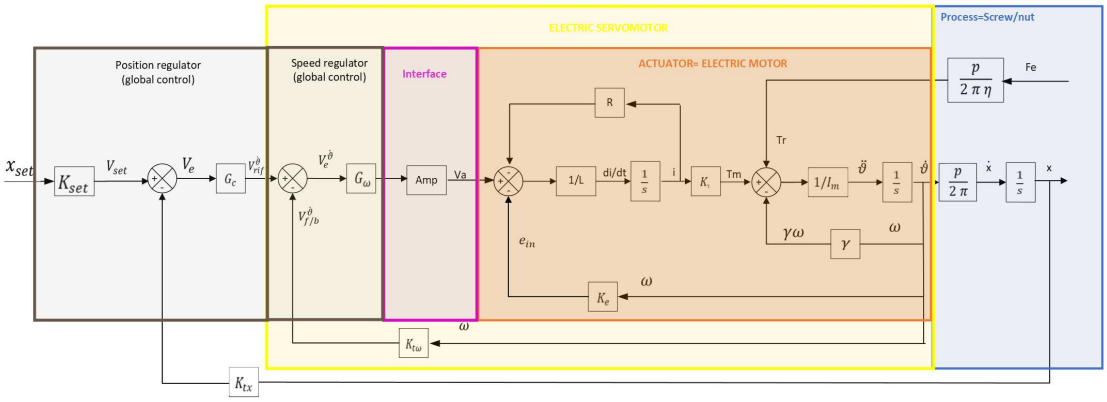


**Figure 5.5:** Complete block diagram of the actuation system

## 5.3 Simplification of the block diagram, related transfer functions and corresponding Bode diagrams

After analyzing the complete block diagram, we proceeded to individually examine and simplify the three distinct loops in order to derive the closed-loop and open-loop transfer functions for each loop [9] . By calculating these transfer functions, we were able to assess the dynamic performance of the system. We evaluated the system's performance by observing the modulus and phase frequency response curves of the three control loops, and then adjusted the controller gain values to achieve the optimal outcome. Next, we will present the Bode diagrams of the closed-loop transfer functions, as well as the Bode diagrams of the open-loop transfer functions. From the former, we can draw conclusions about the attenuation and phase shifting that occurs within the control loop. On the other hand, the stability of the different loops can be assessed by examining the latter diagrams.

In the design process and subsequent discussions, we began by stabilizing the innermost loop and then proceeded to analyze the next loop outward, continuing in this manner until we reached the outermost loop. This sequential approach is implemented because if an inner loop is unstable, all the outer loops containing it will also be unstable.

### 5.3.1 Current control loop

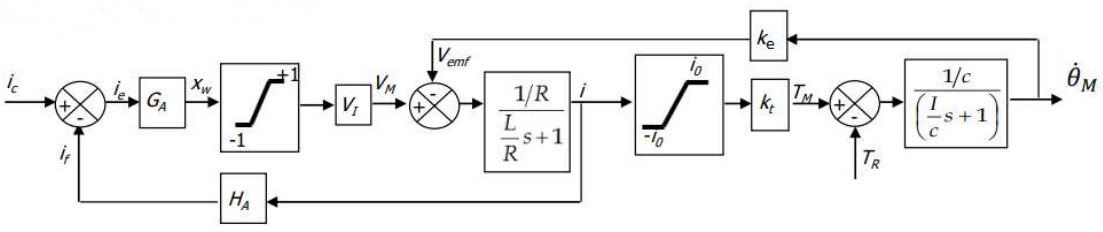


**Figure 5.6:** Current control loop

Variables:

- i: Motor current
- $i_c$: Motor current command
- $i_f$: Motor current feedback
- $i_e$: Motor current error
- $T_M$: Motor torque
- $T_R$: Load torque reflected to motor shaft
- $V_{emf}$: EMF voltage
- $V_M$: Motor voltage
- $x_w$: PWM duty
- $\dot{\theta}_M$: Motor angular speed

Parameters:

- c: Total viscous losses reflected to motor shaft
- $H_A$: Current loop feedback gain
- $i_0$: Maximum current
- $I$: Total inertia (motor axis)
- $k_t$: Motor torque constant
- $k_e$: Motor speed constant
- L: Motor inductance
- R: Motor resistence
- $V_I$: Supply voltage
- $\tau_\epsilon$= L/R: Motor electrical time constant

The following table shows the values of the control loop parameters:

| Current control loop parameters | |
|---|---|
| c | $3.6 \cdot 10^{-4}$ [Nms/rad] |
| $H_A$ | 1 |
| $i_0$ | 13.52 [A] |
| I | $4.78 \cdot 10^{-4}$ [kg$m^2$] |
| $k_t[Nm/A] = k_e[Vs/rad]$ | 0.47 |
| R | $3.8 \cdot 10^{-}3$ [H] |
| L | 0.99 [$\Omega$] |
| $V_I$ | 28 [V] |
| $\tau_e$ | $3.82 \cdot 10^{-3}$ [s] |

**Table 5.2:** Values of the current control loop parameters

By solving the block diagram, the open-loop transfer function $G_{ol.I}$ can be obtained:

$$G_{ol,I} = \frac{i_f}{i_e} = G_A H_A V_i \frac{1/R}{\tau_e s + 1} \tag{5.13}$$

Closing the current loop results in the closed loop transfer function:

$$G_{cl,I} = \frac{G_A V_i \frac{1/R}{\tau_e s+1}}{1 + G_A H_A V_i \frac{1/R}{\tau_e s+1}} \tag{5.14}$$

The block diagram is being simplified and the result is obtained as follows:

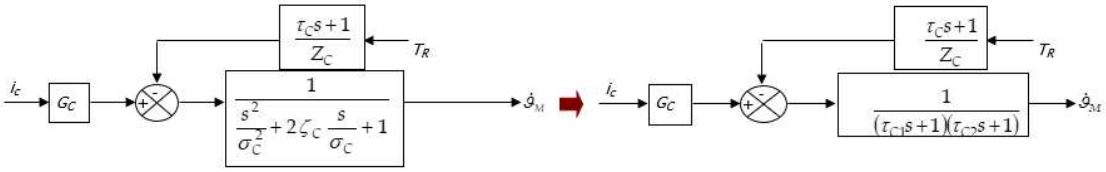


**Figure 5.7:** Current control loop simplified

where:

- $R_e = G_A H_A V_I$=5.60 [Ω]
- $R_C = R + R_E$=6.60 [Ω]
- $d_C = k_t^2 + cR_C = k_t k_e + cR_C = 2.21 \cdot 10^{-1} [kgm^4/s^4A^2]$
- $G_C = k_t G_A V_I / d_C = 11.8 [rad/sA]$
- $Z_C = d_C / R_C = 3.35 \cdot 10^{-2} [Nm/(rad/s)]$
- $t_c = L/R_e = 6.79 \cdot 10^{-4} [s]$
- $\sigma_c = \sqrt{\frac{d_c}{LI}} = 348.7 [rad/s]$
- $\zeta_c = \frac{\sigma_c}{2} \frac{cL+IR_C}{d_C} = 2.490$
- $\tau_{c1} = \frac{\zeta_c + \sqrt{\zeta_C^2 - 1}}{\sigma_C}$ =0.014 [s/rad]
- $\tau_{c1} = \frac{\zeta_c - \sqrt{\zeta_C^2 - 1}}{\sigma_C}$=6.01 $\cdot 10^{-4} [s/rad]$

The open-loop/closed-loop frequency response of the current loop are shown in Figure 5.8 and Figure 5.9.

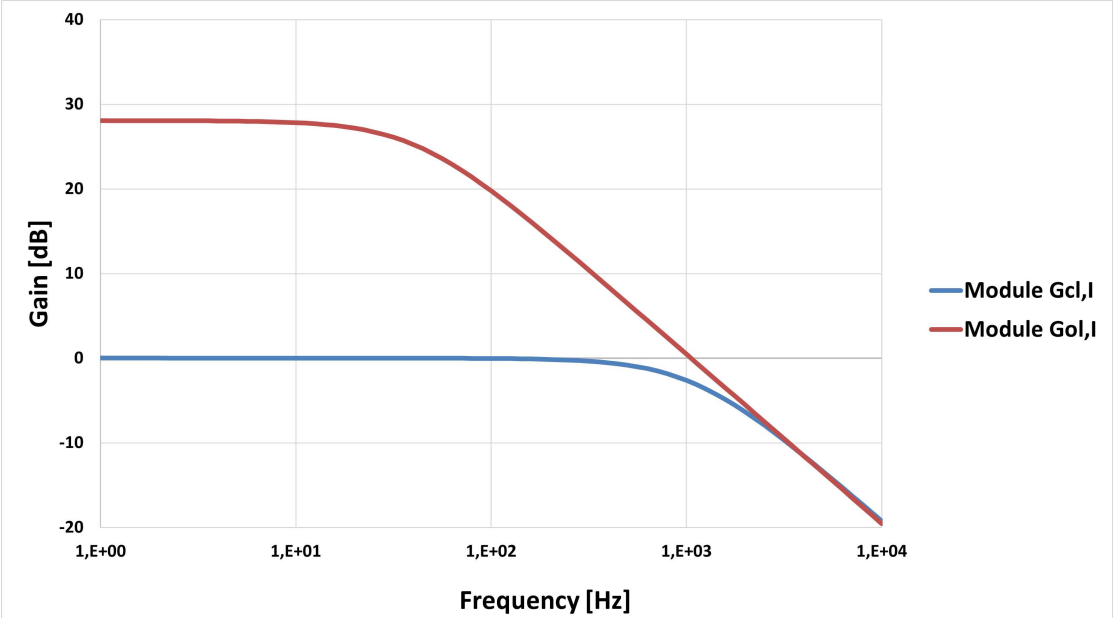


**Figure 5.8:** Frequency response of the current loop-GAIN

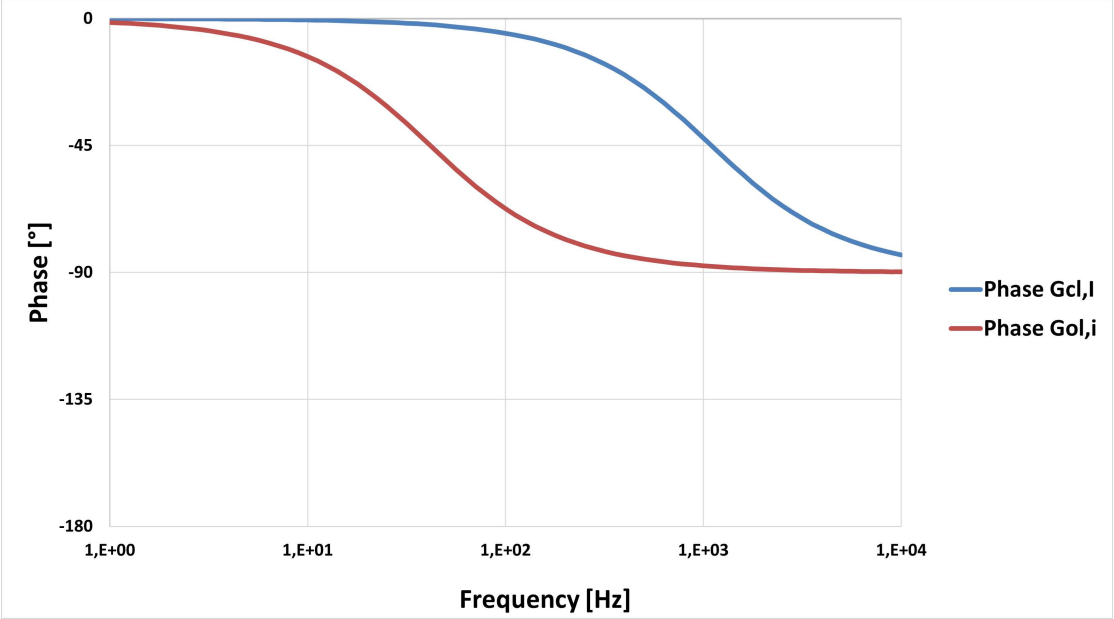


**Figure 5.9:** Frequency response of the current loop-PHASE

In this case, a proportional control has been considered. These findings were obtained through an iterative process aimed at determining the optimal value for the proportional gain ($G_A$) of the controllers. Eventually, a value of 0.900 was set for $G_A$, resulting in satisfactory performance for the control loop, as evidenced by the closed-loop frequency response diagrams. Additionally, the stability of the system was assessed based on the open-loop transfer function graphs.

Since the open-loop transfer function has a single finite pole, indicating a first-order overall system, the phase curve approaches -90° asymptotically but does not surpass it. Consequently, the gain margin ($G_m$) in this case is infinite. The gain margin is defined as the difference between the magnitude of the open-loop transfer function at the critical frequency and the frequency where the phase is -180°. On the other hand, the phase margin ($\Phi_m$), which represents the difference between the critical phase and the argument of the open-loop transfer function at the critical frequency, is equal to 90°.

The phase and gain margins serve as indicators of instability safety. A higher value for these margins implies a more robust system. Typically, acceptable values for ensuring stability are:

$$\Phi_m > 60^\circ \tag{5.15}$$

$$G_m = (7 - 8)dB \tag{5.16}$$

As a result, the analysed current control loop largely respects these limits.

### 5.3.2 Speed control loop

By inserting the block diagram shown in Figure 5.7 and isolating the speed loop, we can derive the block diagram shown in Figure 5.8. Since the transfer function does not naturally have one or more poles at the origin, it is necessary to introduce an integrative contribution in the controller to ensure steady-state accuracy.

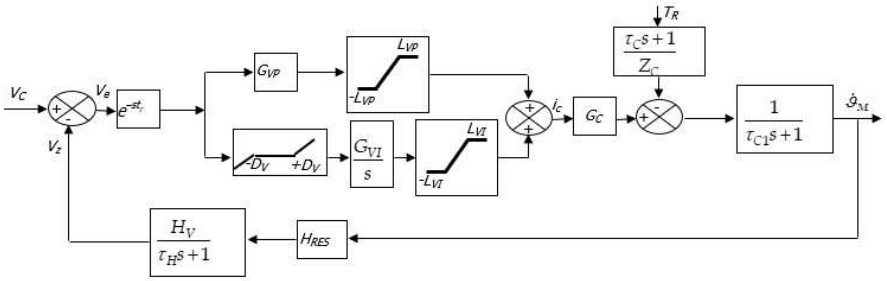


**Figure 5.10:** Speed control loop

Variables:

- $i_c$: Motor current command
- $T_R$: Load torque reflected to motor shaft
- $V_C$: Speed command
- $V_e$: Speed error
- $V_z$: Speed feedback
- $\dot{\theta}_M$: Motor angular speed

Parameters:

- $G_{VI}$: Speed loop integrator gain
- $G_{VP}$: Speed loop proportional gain
- $H_V$: Feedback gain
- $H_{RES}$: Resolver gain
- $L_{VI}$: Speed loop integrator path saturation
- $L_{VP}$: Speed loop proportional path saturation
- $\tau_H$: Feedback filter time constant
- $D_V$: Integrator dead band
- f: Microprocessor recursion rate
- $t_c$: Microprocessor computation time
- $t_r = 1/2f + t_c$: Transport delay

In sizing, only the dominant time constant of the motor is considered. The system has a maximum speed of:

$$\omega_m = 219rad/S = 34.8Hz \tag{5.17}$$

It follows that in order to avoid undersampling, it is advisable to work with a measurement system characterized by a dynamics higher by at least one decade.

$$300Hz = 1885rad/s \tag{5.18}$$

It follows that the time constant of the demodulator filter must be equal to: $5.31 \cdot 10^{-4}s/rad$ In this way, the position signal (later derived to obtain velocity) of the shaft is read accurately, and the carrier of the resolver is suppressed. The sampling frequency of the microprocessor can be assumed to be f=10kHz, considering a computation time of $\tau_c$=10$\mu$s. Consequentially:

$$t_r = \frac{1}{2f} + t_c = 6 \cdot 10^{-5}[s] \tag{5.19}$$

$H_V$(Feedback gain) and $H_{RES}$ (Resolver gain) are set equal to 1, while $\tau_H$ (Feedback filter time constant) has been assumed equal to $8 \cdot 10^{-5}[s/rad]$

Simplifying, the following diagram is obtained, from which it is possible to derive the open-loop transfer function.

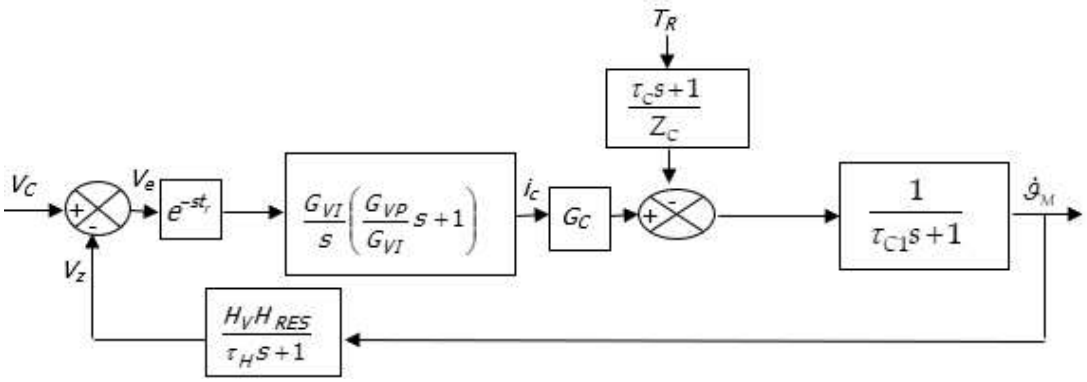


**Figure 5.11:** Speed control loop simplified

$$G_{ol,\omega} = \frac{V_Z}{V_e} = \frac{G_{VI}G_C H_V H_{RES}\left(\frac{G_{VP}}{G_{VI}}s+1\right)e^{-st}}{s(\tau_{C1}s+1)(\tau_H s+1)} \tag{5.20}$$

As the open-loop transfer function does not inherently possess one or more poles at the origin, it was imperative to incorporate an integral component into the controller to ensure precise tracking at the steady state. Closing the speed loop allows us to determine the closed-loop transfer function:

$$G_{cl,\omega} = \frac{\dot{\theta}_M}{\frac{V_C}{H_V H_{RES}}} = \frac{b_{v2}s^2 + b_{v1}s + 1}{a_{v3}s^3 + a_{v2}s^2 + av1s + 1} \tag{5.21}$$

Where the coefficients have the following values:

$$b_{v2} = \frac{G_{VP}}{G_{VI}}\tau_H \tag{5.22}$$

$$b_{v1} = \frac{G_{VP}}{G_{VI}} + \tau_H \tag{5.23}$$

$$a_{v3} = \frac{\tau_{C1}\tau_H}{H_V H_{RES} G_{VI} G_C} \tag{5.24}$$

$$a_{v2} = \frac{\tau_{C1} + \tau_H}{H_V H_{RES} G_{VI} G_C} \tag{5.25}$$

$$a_{v3} = \frac{G_{VP}}{G_{VI}} + \frac{1}{H_V H_{RES} G_{VI} G_C} \tag{5.26}$$

Similarly, it is possible to determine the dynamic stiffness of the speed loop as follows:

$$K_{R,\omega} = \frac{T_R}{\theta_m} = \frac{Z_V(a_{v3}s^3 + a_{v2}s^2 + av1s + 1)}{s(c_{v2}s^2 + c_{v1}s + 1)} \tag{5.27}$$

where:

$$c_{v2} = \tau_C\tau_H \tag{5.28}$$

$$c_{v2} = \tau_C + \tau_H \tag{5.29}$$

$$Z_V = Z_C H_V H_{RES} G_{VI} G_C \tag{5.30}$$

Figures 5.12 and 5.13 show the frequency responses of the speed loop in open and closed loop. Figure 5.14 shows the dynamic stiffness.

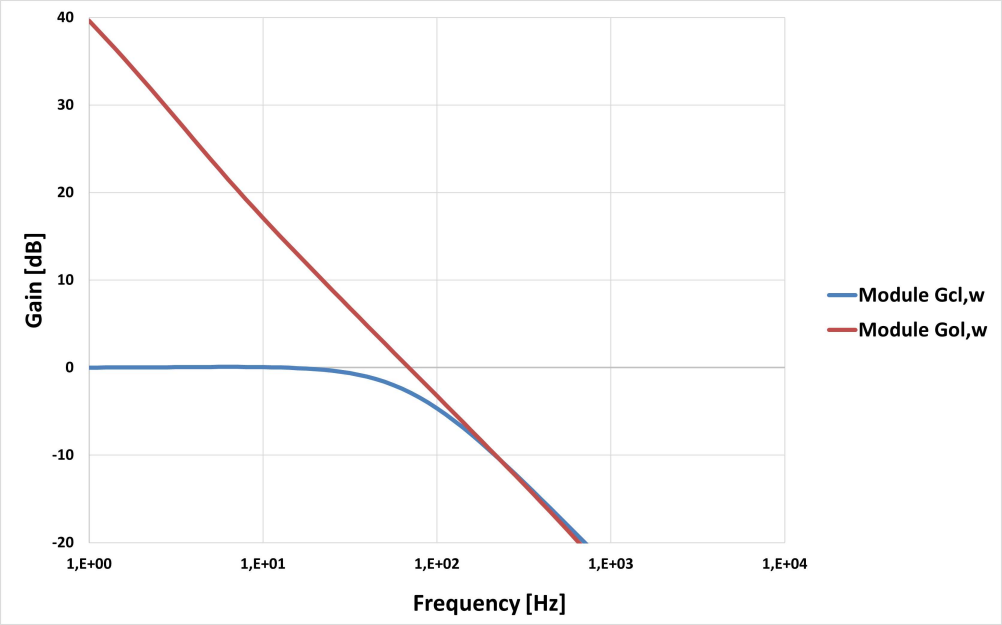


**Figure 5.12:** Frequency response of the speed loop-GAIN

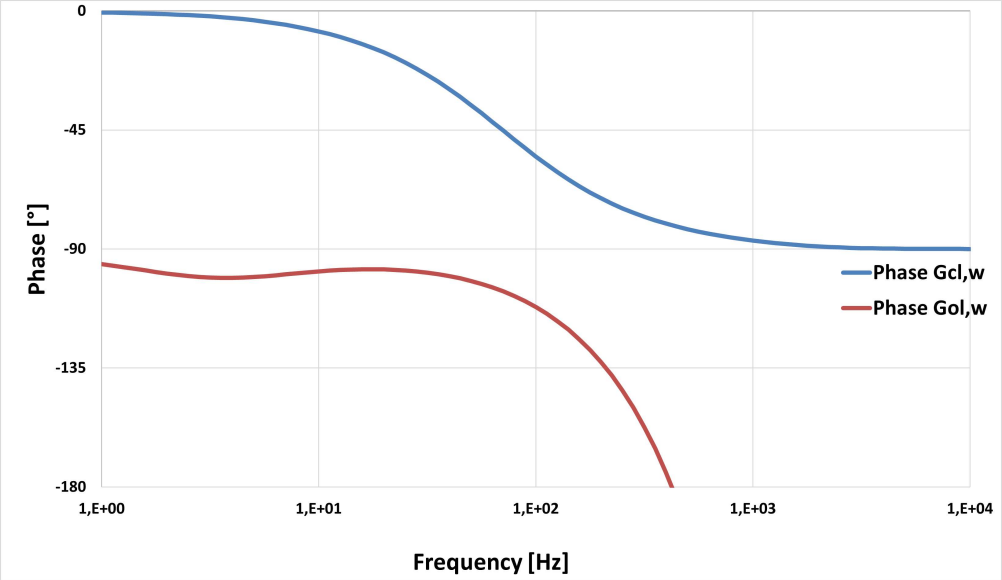


**Figure 5.13:** Frequency response of the speed loop-PHASE

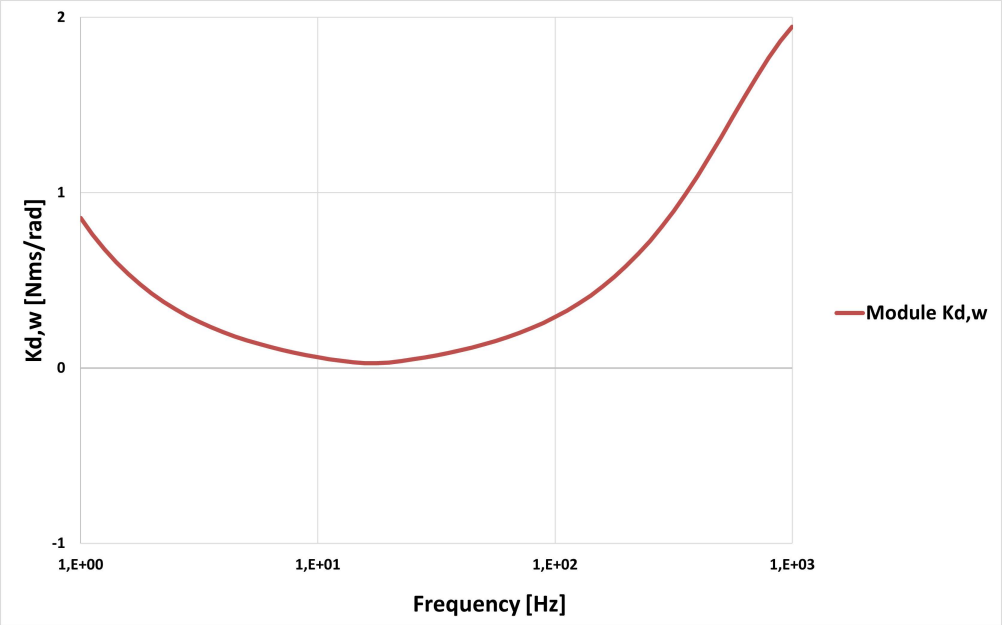


**Figure 5.14:** Dynamic stiffness - speed control loop

Again, the outcomes were acquired through an iterative procedure that enabled us to discover the values of the controllers' gains. We established them at 0.46 for the proportional gain $G_{VP}$ and 12 for the integral gain $G_{VI}$.

It is evident how, by incorporating the integral gain, the system can respond to torque disturbances and ensure that the static gain in the open loop approaches infinity. Consequently, this allows the module of the closed-loop transfer function to initiate from 0 dB. Thus, the presence of the integral gain prevents static errors, ensuring a lack of steady-state error.

Furthermore, it can be observed that the bandwidth of this loop is lower compared to that of the current loop, which is appropriate since it represents the outermost and, therefore, slower loop. Enhancing the proportional gain of the controller can achieve a wider bandwidth, but it must comply with the stability margins specified in Equation 5.15 and 5.16. By adopting the selected gain values for this loop, a gain margin $G_m$ of 16.4 dB and a phase margin $\Phi_m$ of 85° were achieved. Consequently, the angular velocity control loop adheres to the design constraints.

### 5.3.3 Position control loop

Starting from the equations derived in the previous step, we can obtain the block diagram shown in Figure 5.15.

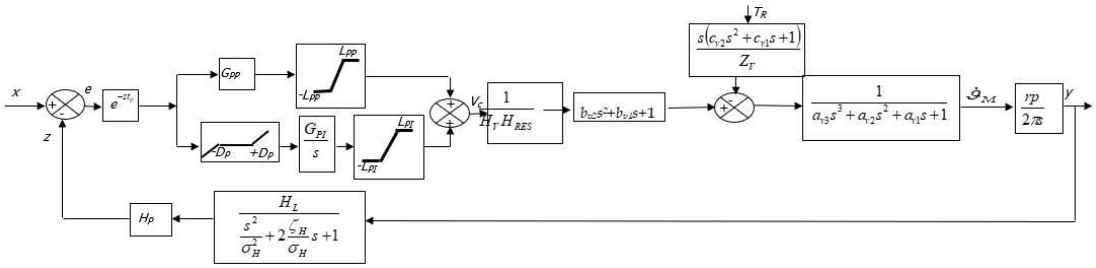


**Figure 5.15:** Position control loop

Variables:

- e: Position error
- $T_R$: Load torque reflected to motor shaft
- $V_C$: Speed command
- y: Actuator position
- z: Position feedback
- $V_Z$: Speed feedback
- $\dot{\theta}_M$: Motor angular speed

Parameters:

- $G_{PI}$: Position loop integrator gain
- $G_{PP}$: Position loop proportional gain
- $H_V$: Feedback gain
- $H_L$: RVDT gain
- $L_{PI}$: Position loop integrator path saturation
- $L_{PP}$: Position loop proportional path saturation
- r: Gear reducer speed ratio
- p/2$\pi$: Rollerscrew lead
- $\sigma_H$: Demodulator filter resonant frequency
- $\zeta_H$: Demodulator filter damping factor
- f: Microprocessor recursion rate
- $t_c$: Microprocessor computation time
- $t_r = 1/2f + t_c$: Transport delay

The gain of the RVDT can be calculated as follows:

$$H_r = \frac{SV_S}{1000}\frac{180}{\pi} = 0.705[V/rad] \tag{5.31}$$

where:

- S is the sensitivity
- $V_s$ is the input voltage

Instead, the feedback gain is calculated as:

$$H_P = \frac{\tau_{RVDT}}{H_r} = 246.83[rad/V] \tag{5.32}$$

Microprocessor recursion rate is equal to 3000 Hz, while microprocessor computation time has been assumed equal to $1 \cdot 10^{-4} s$

Demodulator filter resonant frequence was set equal to 200 Hz, while the value of demodulator filter damping factor is 1s.

In this scenario, it is evident that the open-loop transfer function already possesses a pole at the origin. This pole is associated with the integrator that enables the calculation of the actuator's position from its velocity. Consequently, the control system for the position loop can, in principle, employ a simple proportional controller since the steady-state accuracy is ensured by the pole at the origin of the pure physical integrator. However, this assumption holds true only when external disturbances are absent. To maintain an undisturbed integral term in the denominator and achieve a static stiffness that tends towards infinity, the inclusion of a proportional-integral controller becomes necessary if the steady-state error obtained with the proportional integrator alone is deemed unacceptable. In this particular case, an integrative controller has also been incorporated, albeit with a very small value, as will be elaborated upon subsequently.

By analysing the block diagram, it is possible to write the open-loop transfer function:

$$G_{ol,y} = \frac{z}{e} = \frac{\frac{G_{PI} H_L H_P r p/(2\pi)}{H_V H_{RES}} \left(\frac{G_{PP}}{G_{PI}} s + 1\right) (b_{v2} s^2 + b_{v1} s + 1) e^{-st}}{s^2 (a_{v3} s^3 + a_{v2} s^2 + a_{v1} s + 1) \left(\frac{s^2}{\sigma_H^2} + 2\frac{\zeta_H}{\sigma_H} s + 1\right)} \tag{5.33}$$

Regarding the closed-loop transfer function of the system, considering a second-order system for the measurement chain, we obtain:

$$G_{cl,y} = \frac{y}{x} = \frac{b_2 s^2 + b_1 s + 1}{H_P H_L (a_4 s^4 + a_3 s^3 + a_2 s^2 + a_1 s + 1)} \tag{5.34}$$

where:

$$b_2 = \frac{G_{PP}}{G_{PI}} \left(b_{v1} + 2\frac{\zeta_H}{\sigma_H}\right) + b_{v2} + 2\frac{\zeta_H}{\sigma_H} b_{v1} + \frac{1}{\sigma_H^2} \tag{5.35}$$

$$b_1 = \frac{G_{PP}}{G_{PI}} + b_{v1} + 2\frac{\zeta_H}{\sigma_H} \tag{5.36}$$

$$K_{OP} = \frac{H_P H_L G_{PI} r p/(2\pi)}{H_V H_{RES}} \tag{5.37}$$

$$a_4 = \frac{a_{v2} + 2\frac{\zeta_H}{\sigma_H} a_{v1}}{K_{OP}} \tag{5.38}$$

$$a_3 = \frac{a_{v1} + 2\frac{\zeta_H}{\sigma_H} + b_{v2} K_{OP} \frac{G_{PP}}{G_{PI}}}{K_{OP}} \tag{5.39}$$

$$a_2 = \frac{1 + K_{OP}\left(\frac{G_{PP}}{G_{PI}} b_{vi} + b_{v2}\right)}{K_{OP}} \tag{5.40}$$

$$a_1 = \left(\frac{G_{PP}}{G_{PI}} + b_{v1}\right) \tag{5.41}$$

Similarly, thedynamic stiffness of the position loop with respect to the disturbance can be derived:

$$K_{R,y} = (a_4 s^4 + a_3 s^3 + a_2 s^2 + a_1 s + 1)\frac{Z_V H_P H_L G_{PI}}{s^2 H_V H_{RES}(p/2\pi) r} \tag{5.42}$$

The open-loop and the closed-loop frequency response of the position loop are shown in Figures 5.16 and 5.17 , instead the dynamic stiffness is shown in Figure 5.18.

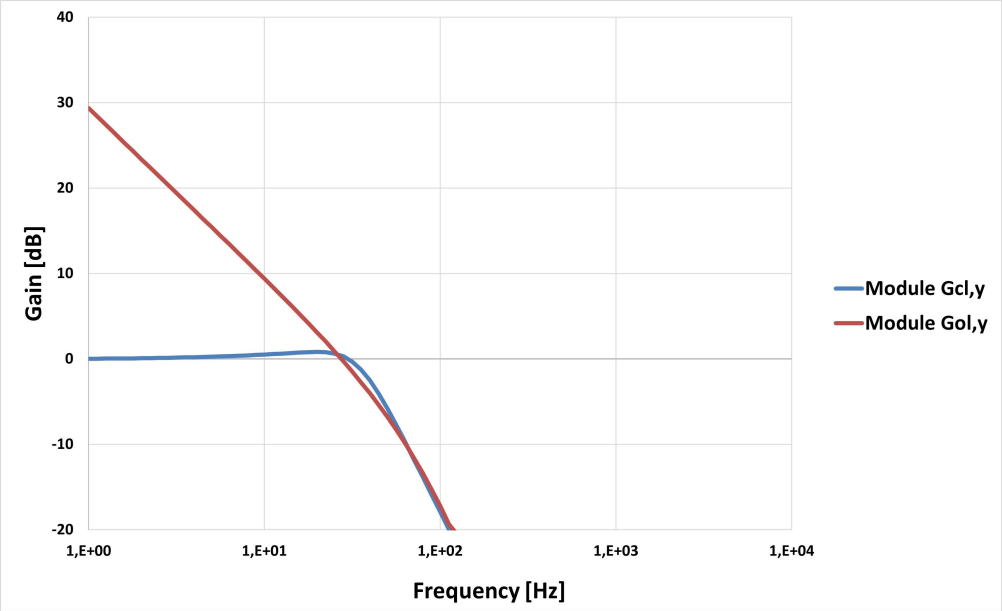


**Figure 5.16:** Frequency response of the position loop-GAIN

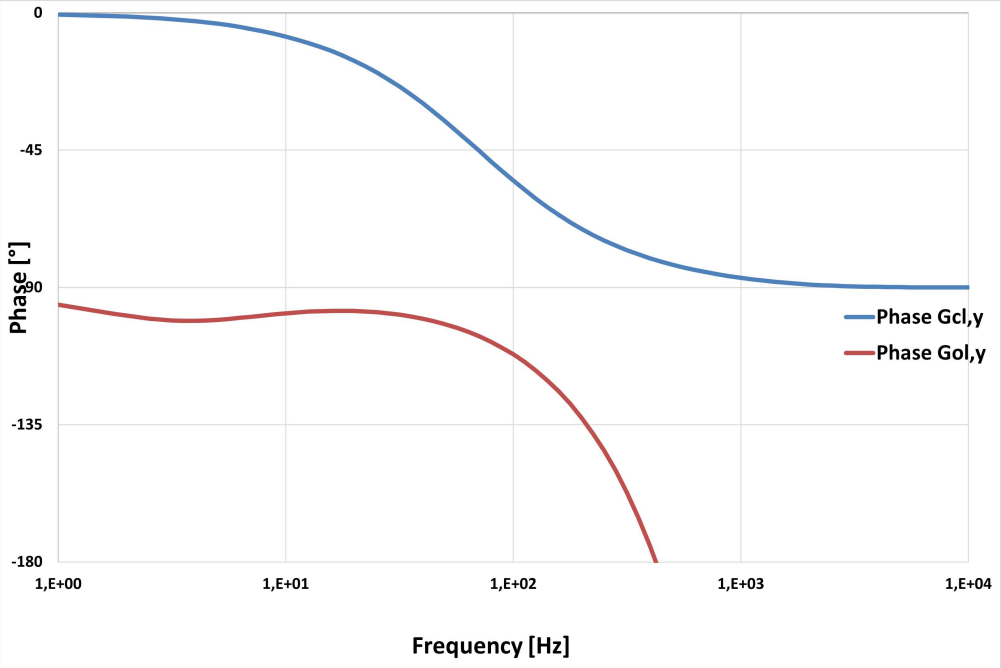


**Figure 5.17:** Frequency response of the position loop-PHASE

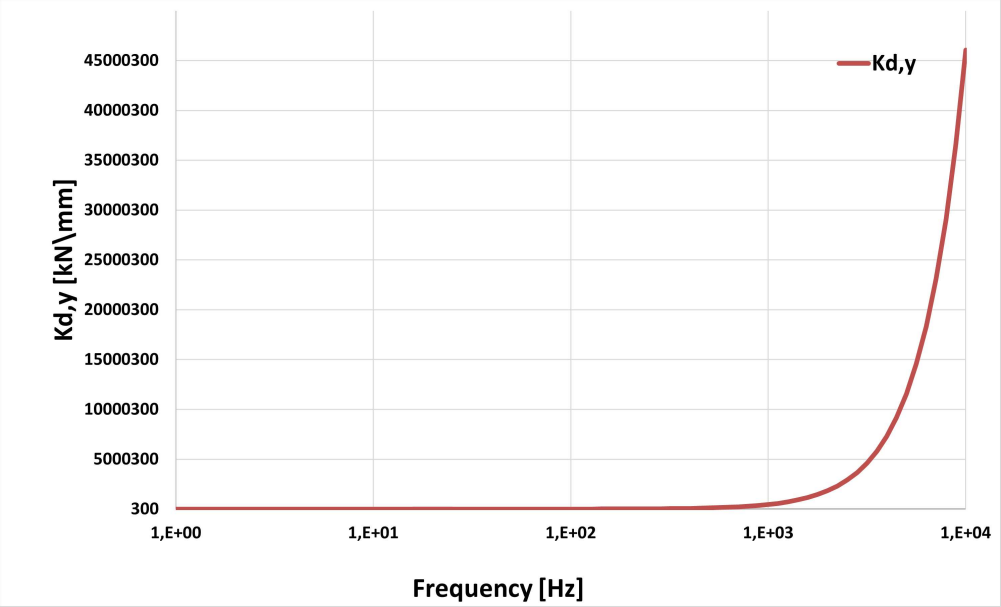


**Figure 5.18:** Dynamic stiffness - position control loop

These plots were generated considering a $G_{PP}$ value of 4000 and a $G_{PI}$ value of 25. As previously mentioned, the integral component is redundant in comparison to the proportional component. The position loop, which is the outermost loop and receives the commanded position from the pilot as an input, is primarily influenced by lower frequencies. As a result, the bandwidth of this control loop is still lower than that of the speed loop. Specifically, in this case, the cutoff frequency, representing the frequency at which the system's amplitude is -3 dB, is 41.5 Hz.

Beyond 70 Hz, the system becomes significantly out of phase, but this frequency range falls outside our area of interest.

The analysis of this final loop is concluded by evaluating the stability margins. From the Bode diagram of the open-loop transfer functions $G_{ol,y}$, a gain margin $G_m$ of 16 dB and a phase margin $\Phi_m$ of 73.96° were obtained. These margins were also found to be within the specified limits for this loop.

# Chapter 6

# Non-linear model for dynamic response

After completing the sizing and constructing the linear model in the Excel environment, a high-fidelity model was subsequently developed using the Matlab-Simulink platform. This software enabled the attainment of more authentic and precise solutions, as it facilitates the solution of constitutive equations for various components in a non-linear fashion. Consequently, employing this software not only eliminates the inherent approximations associated with linearizing a model but also allows for the consideration of numerous phenomena that are imperceptible in the linear model. These include the incorporation of real-world saturations. The system's dynamic characteristics are indeed intricate and non-linear, necessitating a mathematical model to design an effective controller using conventional control strategies like Proportional Integral (PI).

In the initial section of the chapter, an explanation will be provided regarding the models employed to represent each component. Instead, in the concluding paragraphs, the focus will shift towards presenting the results derived from simulating these models. This will serve to showcase the performance demonstrated by the actuation system when exposed to different input commands.

## 6.1 Modelling

The figure 6.1 shows the Simulink model of the complete EMA system. As explained in Chapter 2, two actuators were used in parallel, but since they are identical, the following chapter will proceed by modeling only one of them. The model is divided into subsystems. There are four sections corresponding to the main components of the system. Proceeding from top to bottom, there is the electronic control and sensors, the electric motor, the mechanical transmission, and the flight

control surface. Each subsystem has a set of inputs and outputs and is connected to the others through arrows, which allow the physical flow of information to be understood.

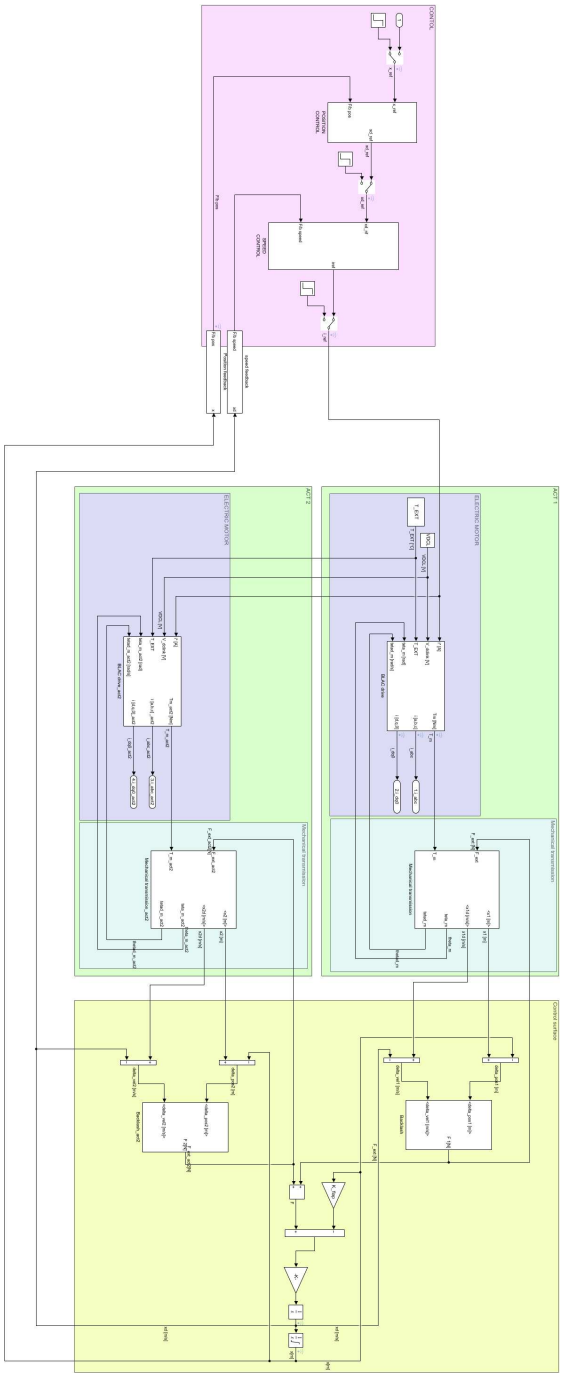

**Figure 6.1:** Simulink diagram of the complete EMA system

For simulating this model, a fixed-step solver was selected instead of the default variable-step solvers provided by the software. The reason behind this choice is that variable-step solvers are not consistent. Although they can reduce simulation time, they can result in misleading solutions and critical issues.

Once the solver type is chosen, the next step is to select the specific method for carrying out the simulation. Among the various fixed-step solvers in Simulink, the Ode14x solver was chosen. This method utilizes Newton's technique to calculate the value of the solution at the next time step. The state of the system at the next time step is determined implicitly based on the current state and the derivative of the state at the next time step, as described by the equation:

$$X(n+1) - X(n) - hdX(n+1) = 0 \tag{6.1}$$

Here, X represents the state, dX represents the state derivative, and h is the step size.

Although this solver requires more computation per step compared to an explicit solver, it offers higher accuracy for a given step size. In this case, a time step of $10^{-5}$ was chosen to strike a balance between the stability of the solving process and the computational effort involved.

### 6.1.1 Control electronics and sensors

In the comprehensive Simulink diagram depicted in Figure 6.1, the control block is accompanied by a switch element that facilitates the management of different types of inputs provided to the control loops. Specifically, utilizing a Matlab script, it becomes feasible to designate the desired input type to be fed into the control loops, such as a step command, a sinusoidal command, or an input for frequency response analysis. Subsequently, the forthcoming sections will highlight the two most frequently employed input types: the step input, utilized for the calibration of various control loops, and the input for frequency response analysis, employed to assess the performance of the servo system.

After this, there are the actual blocks representing the electronic control and sensors. Specifically, there is the position control block (Figure 6.2), which receives as input the reference position of the actuator (i.e., the position commanded by the pilot) and, on the other side, the actual position of the actuator, which is obtained as a feedback signal from the RVDT. The position control block outputs the reference velocity. Following that, there is the velocity control block(Figure 6.3), which takes as input the reference velocity and the feedback velocity from the resolver. Its output is the reference current, which in turn enters the electric motor block. The current controller has been modeled within the 'Motor' block, analogous to the real-world scenario where the electric motor control block tends to be integrated internally.

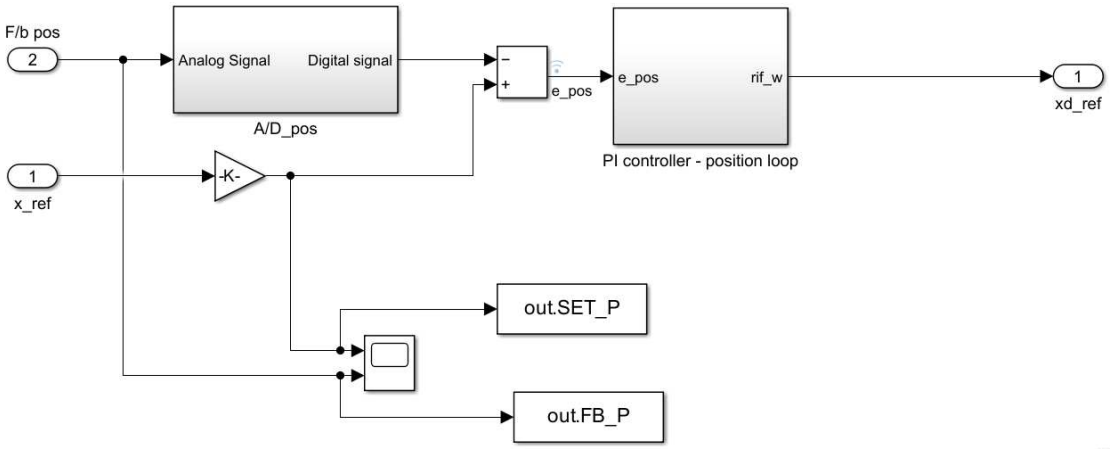


**Figure 6.2:** Simulink scheme of the position control

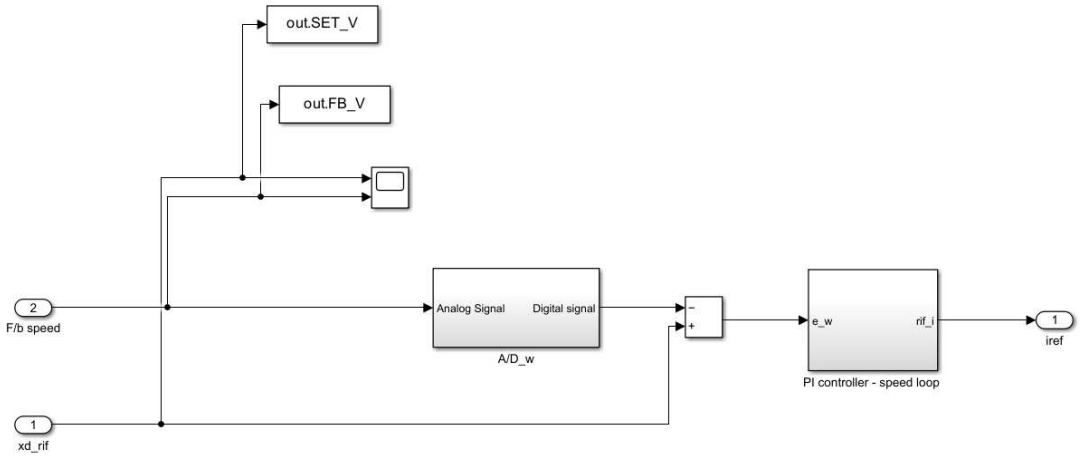


**Figure 6.3:** Simulink scheme of the speed control

It is noticeable that in both cases, the feedback signals are converted from analog to digital.The reason for converting the feedback signals from analog to digital before calculating the error is to facilitate the processing and manipulation of the signals within the digital control system. This allows for precise computation of the error between the set signal and the feedback signal, enabling the control algorithms to make accurate adjustments to achieve the desired position and velocity control. Furthermore, the conversion from analog to digital signals also helps in mitigating noise and disturbances that may be present in the analog signals. Digital signals are less susceptible to noise interference, making the control system more robust and reliable. At the end of the speed control block, the output current signal is converted from digital to analog before entering the motor block for interfacing

purposes with the physical system. Since the motor block operates with analog signals, it is necessary to convert the digital current signal into an analog signal to match the electromechanical system. This conversion ensures compatibility and seamless integration between the digital control system and the analog components of the motor, allowing for accurate and smooth control of the physical actuation system.

The two controllers (position controller(Figure 6.4) and velocity controller(Figure6.5) ) indeed follow the same logic as seen earlier in the linear model, both of them being proportional-integral (PI) controllers.

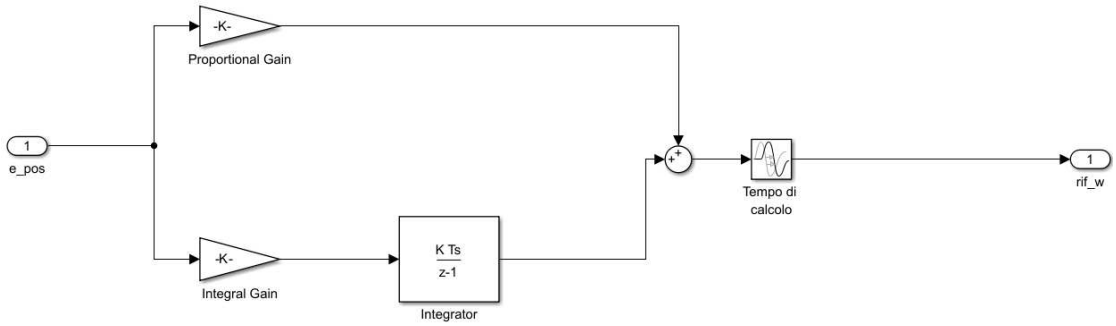


**Figure 6.4:** PI controller - position loo

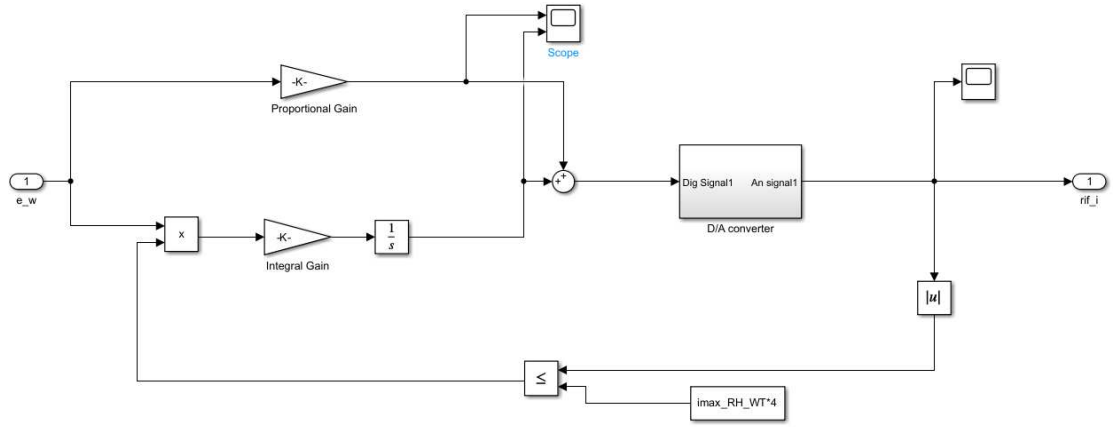


**Figure 6.5:** PI controller - speed loop

At the sensor level, in the nonlinear model, a second-order system was chosen for both the Resolver and RVDT, and a first-order system was chosen for current

sensor [1]. As for the gain of the resolver, it was set equal to 1, while the gain of the RVDT was calculated using the following formula:

$$H_{RVDT} = \frac{SV_s}{1000}\frac{180}{\pi}\sqrt{2} \tag{6.2}$$

where S is the sensitivity , while $V_s$ is the input voltage. The damping coefficient was set to 1 for both the resolver and the RVDT, while the filter natural frequency for the resolver was calculated using the following method.

$$\sigma_{res} = \omega_{max} \cdot Z_P \cdot 100 \tag{6.3}$$

It is important to underscore that the $\sigma_{res}$ was regarded as being 100 times higher than the phenomenon under examination, and this quantity was subsequently multiplied by the total count of polar pairs in the electric motor. Finally, the time constant of the current filter was calculated as follows:

$$\tau_i = \frac{4}{f_{switch,PWM} \cdot 2 \cdot \pi \cdot 1000} \tag{6.4}$$

Table 6.1 presents the parameters of the transducer models.

| Parameters of transmitters non-linear models | |
|---|---|
| Current gain $H_A$ | 1 [V/A] |
| Current time constant $t_i$ | 3.98 $\cdot 10^{-5}$ [s/rad] |
| Resolver gain $H_{RES}$ | 1 [V/(rad/s)] |
| Resolver natural pulse $\sigma_{RES}$ | 3.14 $\cdot 10^{5}$ [rad/s] |
| Resolver damping factor $\zeta$ | 1 |
| RVDT gain $H_L$ | 0.705 [V/rad] |
| RVDT natural pulse $\sigma_H$ | 1257 [rad/s] |
| RVDT damping factor $\zeta$ | 1 |

**Table 6.1:** Values of the current control loop parameters

The control electronics then send a command signal or vector to the power electronics of the command signals, depending on the error observed between set and feedback.

[1] In the linear model, the resolver was modeled as a first-order system, while the current sensor ad a zero-older system (see table 5.1 ).

### 6.1.2 Electric motor

The inputs to the Simulink model of the electric motor are:

- the reference current i*, resulting from the block upstream of the control electronics;
- the DC-link voltage $V_{dclink}$, supplied as a constant value and equal to 360 V, i.e. equal to 3/2 the motor voltage chosen in the sizing phase;
- the rotation angle of the shaft between the motor and the screw mechanism $\theta_m$ and its angular speed $\dot{\theta_m}$: values which arrive in feedback from the equilibrium to the shaft carried out in the downstream;
- temperature of the external environment $T_{EXT}$: value that is defined by the user at each simulation.

This model, characterised at this stage as a three-phase motor, presents the motor torque $T_m$ and winding currents as output.

In turn, the 'BLAC' subsystem was divided internally into four sections: Input signals, Control, Electronic power unit and Electric motor(Figure 6.6).

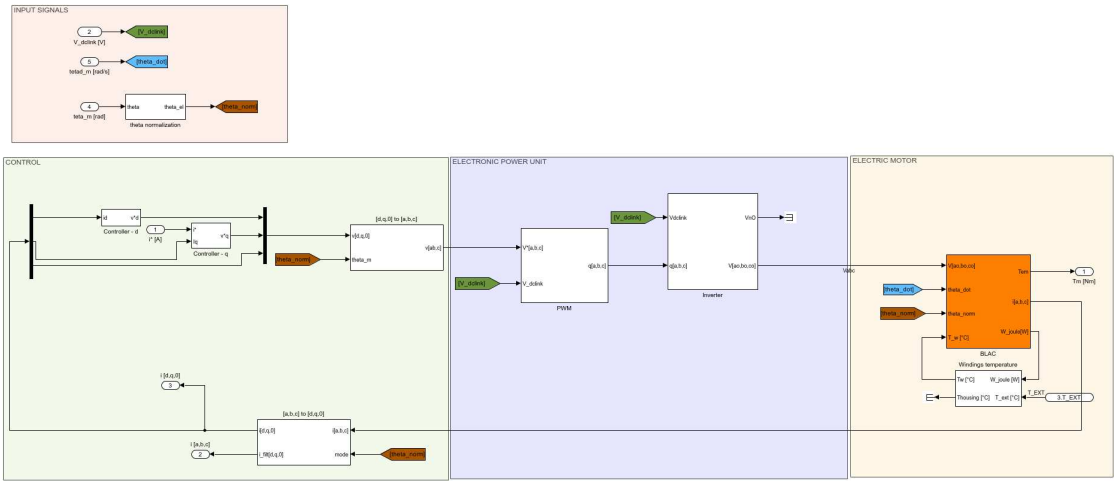


**Figure 6.6:** Internal layout of the Simulink BLAC model

In the initial section, the focal point lies on the block responsible for normalizing the rotation angle $\theta$. Specifically, this process enables the extraction of the electrical angle from the rotational angle feedback received from the downstream 'Mechanical transmission' block. By employing a resolver, modeled in an identical manner to the one described in the preceding subsection, the mechanical angle of the motor, denoted as $\theta_m$, can be derived. It is crucial to emphasize that this particular

modeling approach was chosen to circumvent potential issues. Instead of replicating the resolver model, an alternative method would have involved using only one resolver to obtain angular position measurements and subsequently calculating angular velocity through time-based differentiation. However, the latter approach would have necessitated the incorporation of a discrete derivative with a suitable sampling rate throughout the entire electric motor model, leading to unnecessary complications in this application.

Subsequently, by multiplying the value of the mechanical angle by the number of pole pairs $Z_p$, the electrical degree $\theta_{el}$ can be obtained. It is important to note that BLAC electric motors consist of three phases (a, b, c), which are nominally electrically identical but offset from one another by an electrical angle of 120°. This electrical degree $\theta_{el}$ corresponds to a multiple of the mechanical angle, or geometric angle, $\theta_m$, relative to the number of pole pairs $Z_p$ present on the rotor.

$$\theta_{el} = \theta_m Z_p \tag{6.5}$$

The second section is the control part. As discussed earlier in Chapter 3.5 a FOC (Field Oriented Control) approach was chosen for this specific application. FOC, introduced by Hasse and Blaschke in the 1970s, draws an analogy between AC motors and DC motors, where mechanical current commutation is achieved. In DC motors, the magnetic flux is controlled independently by the excitation current, while the torque is regulated by the armature current. Thus, the two currents are electrically and magnetically decoupled. Conversely, in AC motors, the stator's armature current influences both the magnetic field and the resulting torque. The decoupling of flux and torque is achieved by analyzing the instantaneous current and dividing it into two components: the field current and the current associated with torque development. FOC effectively aligns the stator current to maintain a spatial angle of 90° [2] between the rotor and stator flux, thereby enabling independent and "decoupled" control of flux and torque.

To implement FOC, a position sensor is necessary for continuous monitoring of the rotor position, which is why the resolver model was included in the preceding section. Additionally, FOC requires control over the magnitude and phase of AC quantities, hence it is often referred to as the "vector control method." However, the high-speed nature of this motor application makes it impractical to manipulate rapidly changing AC parameters using sophisticated algorithms and high-end processors. To simplify the complexity, two popular transformations known as Clarke and Park transformations are employed to convert the AC parameters into DC equivalents.

[2]The motivation lies in the fact that for a given current, maximum torque can be obtained only when the stator flux is orthogonal to the rotor flux

Clarke's transformation translates the variables from a reference frame with three magnetic axes (a, b, c), representing the three-phase system, to an orthogonal reference frame with two magnetic axes ($\alpha$, $\beta$) fixed to the stator, as depicted in Figure 6.7 . This transformation is also known as the $\alpha$, $\beta$ transformation for this reason.

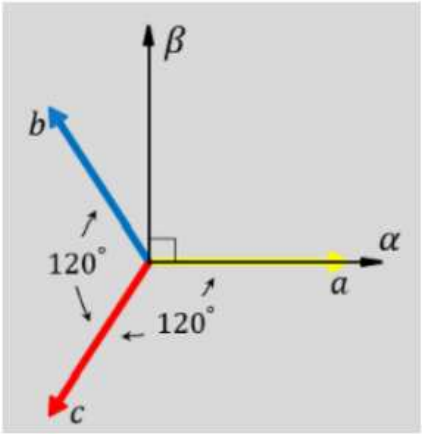


**Figure 6.7:** Stator reference systems

The matrix leading to this transformation is precisely Clarke's matrix, that in its power invariant version is:

$$\begin{bmatrix} \alpha \\ \beta \\ 0 \end{bmatrix} = \sqrt{\frac{2}{3}} \begin{bmatrix} 1 & -\frac{1}{2} & -\frac{1}{2} \\ 0 & \frac{\sqrt{3}}{2} & -\frac{\sqrt{3}}{2} \\ \sqrt{\frac{1}{2}} & \sqrt{\frac{1}{2}} & \sqrt{\frac{1}{2}} \end{bmatrix} \begin{bmatrix} a \\ b \\ 0 \end{bmatrix} \tag{6.6}$$

Instead the Park Transformation is also recognized as the d,q transformation. It serves the purpose of converting three-phase AC quantities into two-phase DC quantities by transforming the three-phase magnetic axes (a, b, c) into a rotating frame consisting of two axes (d, q) fixed to the rotor, as illustrated in Figure 6.8. Park's transformation typically involves a combination of the Clarke transformation and a subsequent rotation. If we consider aligning a power-invariant a-phase vector with the q-axis, the corresponding matrix is as follows:

$$\begin{bmatrix} d \\ q \\ 0 \end{bmatrix} = \sqrt{\frac{2}{3}} \begin{bmatrix} sin\theta & sin(\theta - \frac{2\pi}{3}) & sin(\theta + \frac{2\pi}{3}) \\ cos\theta & sin(\theta - \frac{2\pi}{3}) & sin(\theta + \frac{2\pi}{3}) \\ \sqrt{\frac{1}{2}} & \sqrt{\frac{1}{2}} & \sqrt{\frac{1}{2}} \end{bmatrix} \begin{bmatrix} a \\ b \\ c \end{bmatrix} \tag{6.7}$$

with $\theta$ the angle between the q-axis and the a-axis which is fixed to the stator.

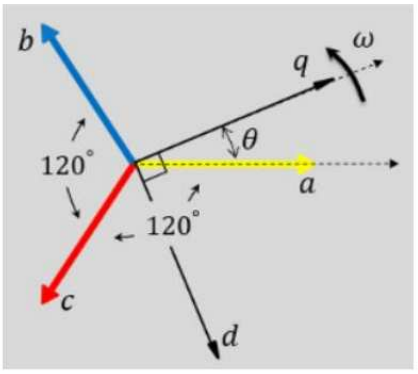


**Figure 6.8:** Rotor reference system where the a-axis and the q-axis are initially aligned

The Park transformation greatly simplifies the operation of FOC by introducing a rotating reference frame that aligns with the rotor flux axis. In this frame, the q and d current components remain constant. The direct component of current, $i_d$, runs parallel to the direction of the rotor flux, while the quadrature component, $i_q$, is perpendicular to it and aligns with the orientation of the current space vector for maximum torque output. By maintaining $i_d$ at zero and allowing $i_q$ to generate the magnetomotive force field in the stator, maximum torque can be achieved. The objective of the control system is therefore to minimize the value of $i_d$ and bring $i_q$ to the desired value.

This technique facilitates motor control in a manner analogous to a DC motor with independent excitation. It can be implemented using current control with a linear proportional-integral (PI) controller and a subsequent pulse-width modulation (PWM) inverter [10].

The proposed field-oriented control (FOC) for permanent magnet synchronous motors (PMSMs) was realized on the Simulink platform.

Taking a closer look at the control component presented in Figure 6.9, it becomes evident that the resolver-derived angular position and the currents from the three windings (a, b, c) of the actual motor model feed into the [a,b,c] to [d,q,0] block. Within this block, as depicted in Figure 6.10, a current sensor was implemented. In linear modeling, the current transducer was initially modeled as a zeroth-order, whereas in this case, it is modeled as a first-order with a time constant $\tau_i$ set to $2.5 \cdot 10^{-5}$ [s/rad]. However, in this case, three separate sensors or feedback current filters were utilized, each corresponding to a specific phase. Through the utilization of the Park transformation matrix outlined in Equation (6.7), the three-phase filtered currents are subsequently transformed into d, q parameters.

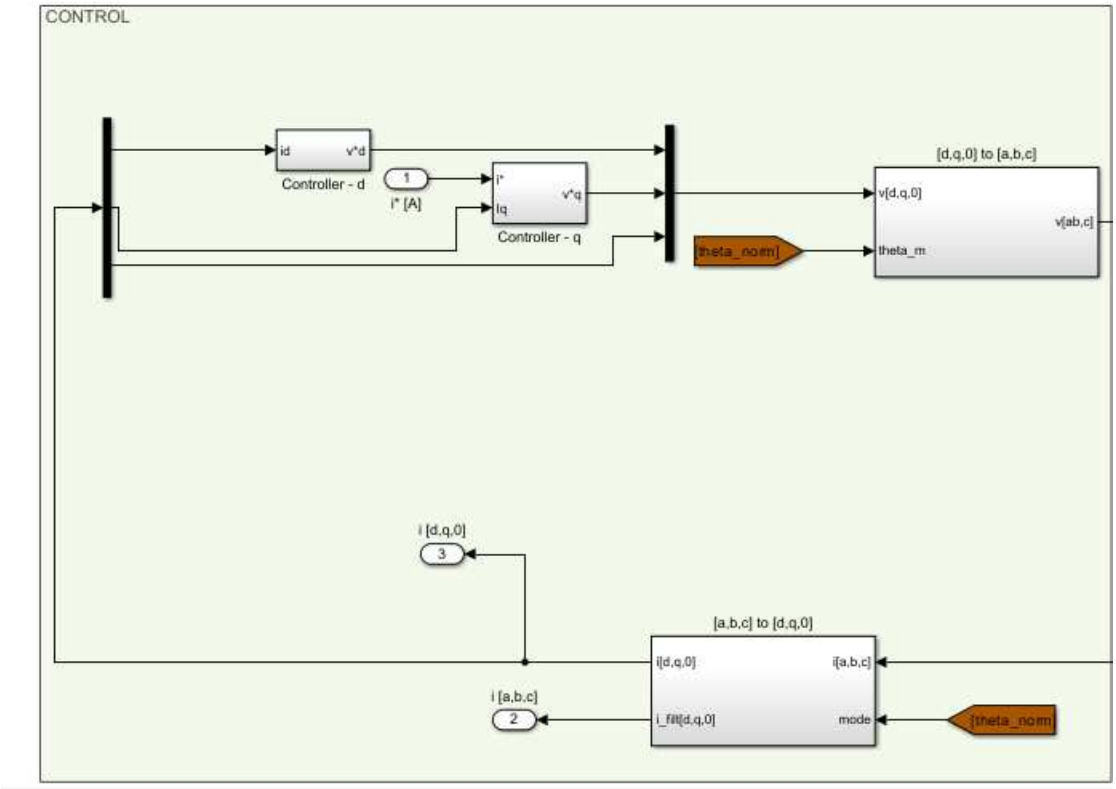


**Figure 6.9:** Simulink scheme of the electric motor control

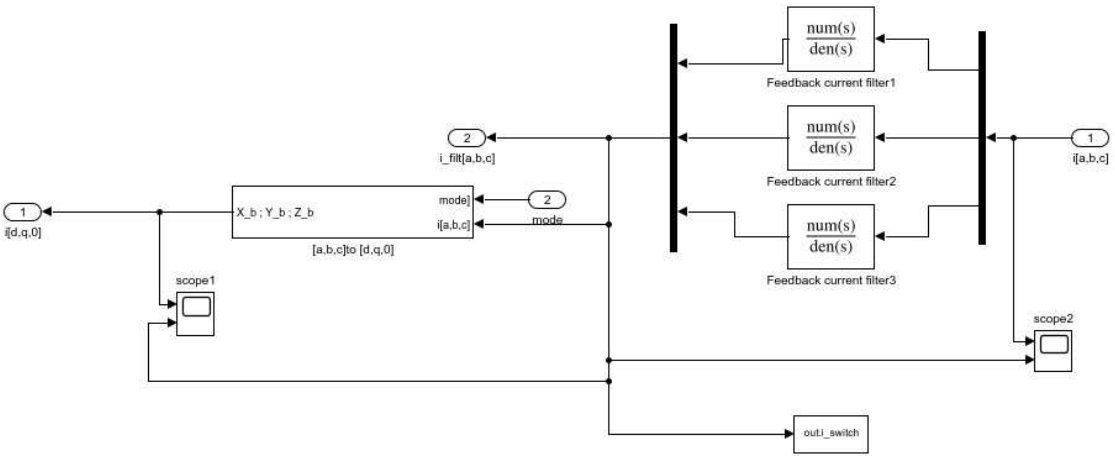


**Figure 6.10:** Simulink block [a,b,c] to [d,q,0]

Subsequently, these currents $i_d$, $i_q$ are directed to the PI controllers. In the d-axis controller, the compensation is applied to the error between zero and $i_d$, while in the q-axis controller, the compensation is based on the difference between the reference current and $i_q$. In practice, the calibration of both controllers is required, but it is common to use the same proportional and integral gain values for both axes. The outputs of these controllers, denoted as $v_d*$ ans $v_q*$, represent the corrective voltages for the d-axis and q-axis, respectively.

Subsequently, through the Simulink block [d,q,0] to [a,b,c], the d-axis and q-axis voltages are converted back into the voltages for the three stator windings, a, b,c, by employing inverse Park transformation. These voltages, $v_a, v_b, v_c$, are then sequentially sent to the power electronics system, which comprises the PWM and inverter models.

It is important to note that the modeling of the electric motor also necessitates the inclusion of the power electronics. Power electronics refers to the collection of electronic devices required to manage and regulate the electrical power sourced from an electrical network (in this case, the aircraft network) and directed towards an electrical load (in this case, the electric motor). In most instances, power conversion between the network and the electrical load is achieved through two interconnected converters, coupled via an energy storage component known as the DC-link.

Moreover, as electric motors represent an inductive electrical load, the power electronic converters commonly employed in servo systems adopt the capacitive DC-link configuration illustrated in Figure 6.11. The mains-side converter is responsible for transforming the electrical quantities from the mains into continuous quantities. The presence of a capacitive DC-link ensures the existence of a nearly constant voltage at the terminals of the load-side converter, which consequently operates as an impressed voltage source.

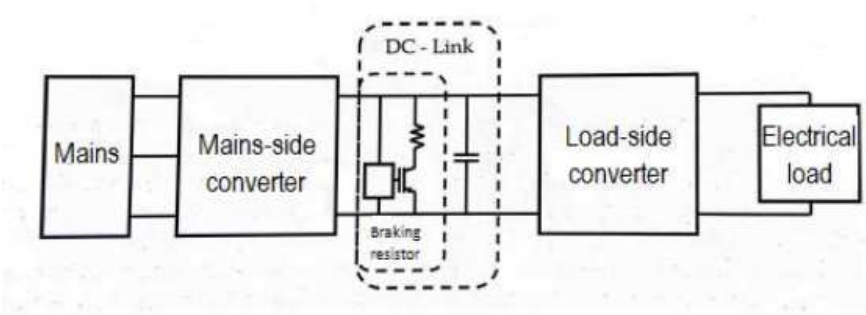


**Figure 6.11:** Schematic diagram of a power electronic converter with capacitive DC-link and braking resistor.[9]

For this particular application, the load-side converter consists of an inverter and a PWM modulator. These components work in tandem to determine the supply voltage applied to the windings, aiming to achieve the desired current magnitude in each of them. In order to generate a voltage waveform of arbitrary shape, the inverter employs a control strategy that involves alternating between available voltage levels or vectors. This ensures that the time-averaged or fundamental component of the switched voltage waveform approximates the desired voltage reference. This process is commonly referred to as modulation.

Among the various techniques for achieving power modulation using digital devices in an analog system, pulse width modulation (PWM) is the most widely employed. PWM involves generating a switching law, denoted as q(t), which governs the transitions from the 'ON' state to the 'OFF' state of each digital element in a manner that allows the time-averaged value of the controlled variable to match the desired value. To achieve this, the modulating or command signal, which represents the desired value of the controlled quantity, is compared with a signal that repeats periodically at a constant frequency known as the carrier signal. The duration of each switching cycle is defined as the switching period, denoted as $T_{switch}$, corresponding to the frequency of the carrier signal.

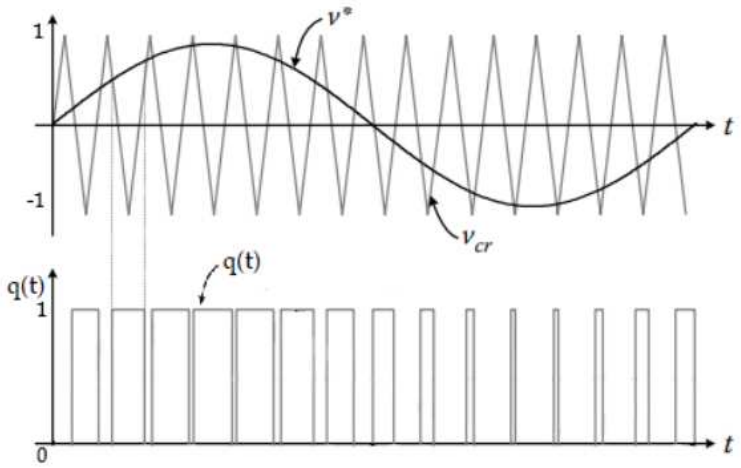


**Figure 6.12:** PWM, switching waveform generation

As can be seen in Figure 6.12, indicating with $v_{cr}$ the triangular carrier signal and with v* the reference voltage or modulating signal, the control signal q(t) follows the law:

$$\begin{cases} q(t) = 1 & if \quad v^*(t) > v_{cr} \\ q(t) = 0 & if \quad v^*(t) \leq v_{cr} \end{cases} \tag{6.8}$$

Is then defined as duty cycle d(t):

$$d(t) = \frac{T_{ON}(t)}{T_{switch}} \tag{6.9}$$

where $T_{ON}$ is the fraction of time during which the value of the modulating signal exceeds the value assumed by the carrier for the same instant of time t.

The content that was written was subsequently transferred to Simulink utilizing the model portrayed in Figure 6.8. It is apparent that the voltages across the windings, commanded by the controller $v_a, v_b, v_c$, are normalized by half of the accessible supply voltage - specifically, the voltage provided by the DC-link. These normalized voltages are then compared to the unit bipolar triangular carrier. As a result, a binary logic signal q is generated, following Equation (6.4), and subsequently converted into a double. Taking into consideration the presence of three phases, there will be respective signals $q_{a,b,c}$ which will determine the digital control signal at the corresponding switching pole of the inverter.

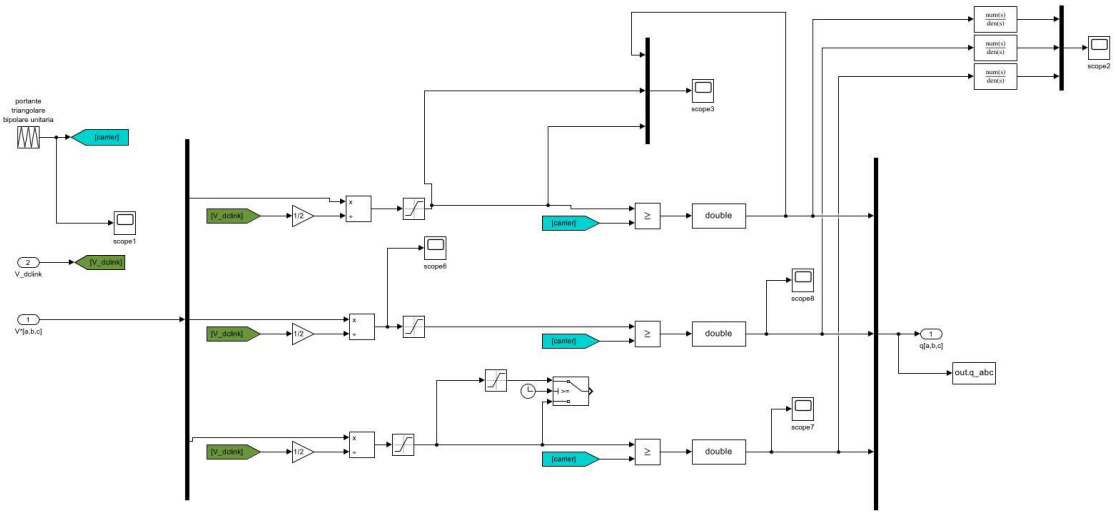


**Figure 6.13:** Simulink scheme of PWM

Indeed, given that the power electronics supplies a three-phase electrical load, it becomes essential to incorporate a converter with the capability to transform the continuous electrical quantities on the DC-link into alternating quantities. This task is accomplished through the utilization of a DC-AC converter, commonly referred to as an inverter. Figure 6.15 illustrates an instance of an inverter designed for the three-phase scenario. Inverters are formed by connecting three bidirectional switching poles to a solitary DC voltage source (depicted as the DC-link). Each bidirectional switching pole comprises two controllable electronic elements (such as

MOSFET or IGBT [3]) and two diodes. Additionally, a logic NOT gate ensures that the two power transistors are never concurrently switched "ON" to prevent short circuits. The load, in this case, connected in a star configuration, is then linked to the outputs of each switching pole.

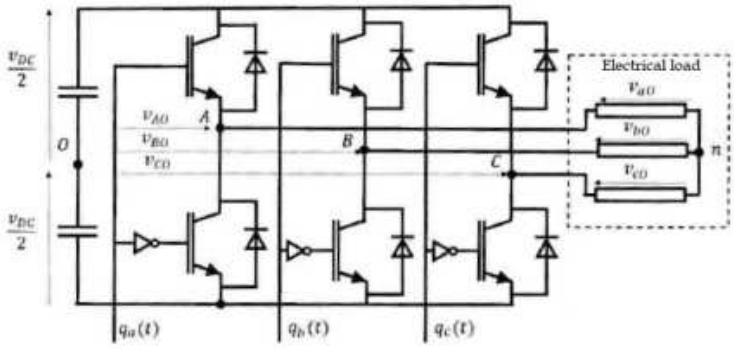


**Figure 6.14:** Three-phase PWM-controlled inverter diagram [9]

By designating O as a fictitious reference point within the power supply system, where the DC-link voltage $V_{dclink}$ is evenly divided into two equivalent parts, the focus can be placed on the voltage disparity between point A, which corresponds to the connection of phase a of the load, and point O. Taking $q_a$ as the digital control signal derived from the preceding PWM process at the respective switching pole, the value of $v_{A0}$ can be obtained using the following approach.

$$v_{A0} = [2q_a(t) - 1]\frac{V_{dclink}}{2} \tag{6.10}$$

Similar expressions are valid to the other voltages supplied by the converter.

$$\begin{cases} v_{A0} = [2q_a(t) - 1]\frac{V_{dclink}}{2} \\ v_{B0} = [2q_b(t) - 1]\frac{V_{dclink}}{2} \\ v_{C0} = [2q_c(t) - 1]\frac{V_{dclink}}{2} \end{cases} \tag{6.11}$$

The common mode voltage $v_{n0}$ is then introduced

$$v_{n0} = \frac{1}{3}[v_{A0}(t) + v_{B0}(t) + v_{C0}(t)] \tag{6.12}$$

[3]The main discriminator between IGBTs and MOSFETs is the field of application. MOSFETs are generally preferred for low power applications and voltages below 200 V, while IGBTs are used for higher power and voltage applications

The common mode voltage allows the voltages supplied to the inverter $(v_{A0}, v_{B0}, v_{C0})$ to be linked to the phase voltages acting on the load $(v_{a0}, v_{b0}, v_{c0})$.

$$\begin{cases} v_{a0} = v_{A0} - v_{n0} \\ v_{b0} = v_{B0} - v_{n0} \\ v_{c0} = v_{C0} - v_{n0} \end{cases} \tag{6.13}$$

The functional modelling of the inverter using Simulink software is shown in Figure 6.15

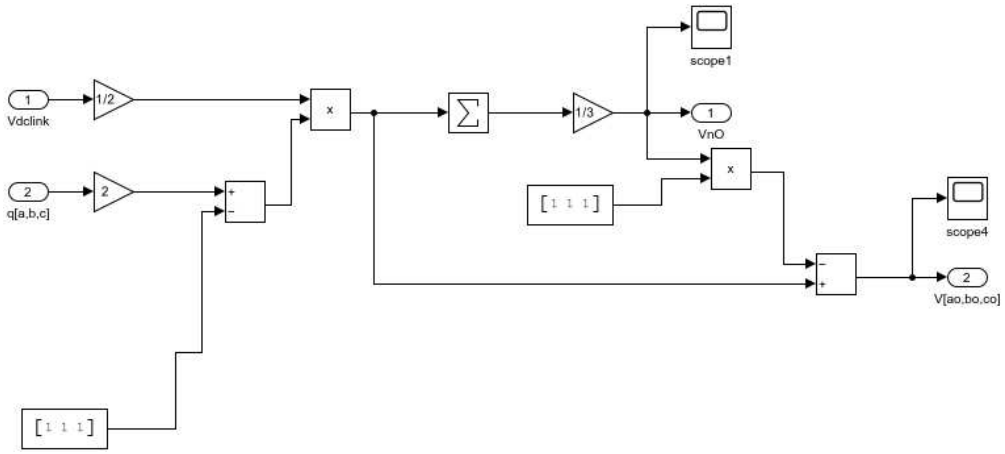


**Figure 6.15:** Simulink diagram of the inverter

The outcome of the inverter, referred to as the phase voltages $v_{a0}, v_{b0}, v_{c0}$, subsequently enters the fourth and final segment of the electric motor, as depicted in Figure 6.1. More precisely, they enter the "BLAC" module along with the electrical rotation angle $\theta_{el}$, the motor angular velocity $\dot{\theta}$, and the temperature of the windings $T_W$. The latter is determined within the "Windings temperature" module, which takes into account the power dissipated due to Joule heating and the external temperature.

Regarding the "BLAC" module, it is further divided into three subsystems: "Back-emf," "Electrical dynamics-backup," and "Electro-magnetic torque computation." The first subsystem comprises the equations responsible for computing the back-electromotive force present in the motor at each moment and estimating the torque constant $k_t$ as the ratio of the back-electromotive force to the motor's angular velocity. The second subsystem implements the electrical dynamics of the motor, providing the winding currents and the power dissipated through Joule heating as a function of three factors: the voltages applied to the windings, the generated back-electromotive force, and the temperature attained in the windings. Lastly, the

third subsystem calculates the delivered torque by multiplying the torque constant by the current flowing in each winding.

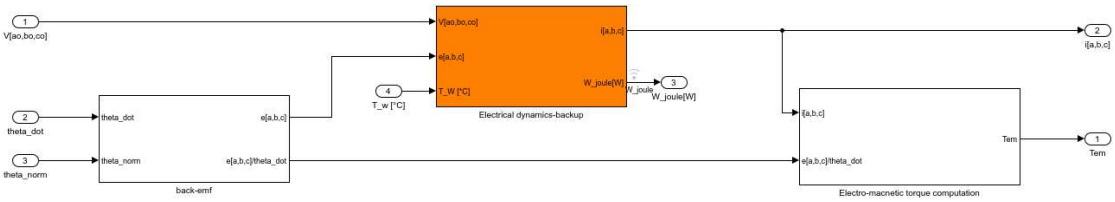


**Figure 6.16:** Simulink scheme of BLAC

Since the three phases of the BLAC motor are fundamentally electrically identical, it is possible to introduce three magnetic axes a, b, c, which are electrically offset by 120° and correspond to the three phases (a, b, c). Solving the electrical circuit on the three-phase axes yields the following system of equations:

$$\begin{cases} v_{a0} = R_a i_a + L_a \frac{di_a}{dt} + M\frac{di_b}{dt} + M\frac{di_c}{dt} + \frac{d\phi_a(\theta_{el})}{dt} \\ v_{b0} = R_b i_b + L_b \frac{di_b}{dt} + M\frac{di_a}{dt} + M\frac{di_c}{dt} + \frac{d\phi_b(\theta_{el})}{dt} \\ v_{c0} = R_c i_c + L_c \frac{di_c}{dt} + M\frac{di_a}{dt} + M\frac{di_b}{dt} + \frac{d\phi_c(\theta_{el})}{dt} \end{cases} \tag{6.14}$$

The phase voltages $v_i$ can be expressed as a function of the i-th phase current $i_i$ and the concatenated phase flux $\phi_i$, taking into account the electrical winding resistances $R_i$, inductances $L_i$, and mutual inductances M. Phase back-electromotive forces have a sinusoidal form, given the distribution of the stator windings, and can therefore be expressed as a function of a phase constant $k_{e,k}$ and the electrical position of the rotor $\theta_{el}$.

$$\begin{cases} e_a = \frac{d\phi_a(\theta_{el})}{dt} = k_{e,a} cos(\theta_{el})\dot{\theta} \\ e_b = \frac{d\phi_b(\theta_{el})}{dt} = k_{e,b} cos(\theta_{el} - \frac{2\pi}{3})\dot{\theta} \\ e_c = \frac{d\phi_c(\theta_{el})}{dt} = k_{e,c} cos(\theta_{el} + \frac{2\pi}{3})\dot{\theta} \end{cases} \tag{6.15}$$

Figure 6.17 shows the "Back-emf" subsystem, in which the system of equations given in Equation (6.15) has been implemented.

Potential malfunctions, such as partial demagnetization of components or a deviation in the air gap between the stator and rotor due to improper alignment, have not been taken into account within this subsystem. Then, considering a balanced and symmetrical three-phase system, the common mode current $i_0$ cancels.

$$i_0(t) = \frac{1}{3}[i_a(t) + i_b(t) + i_c(t)] = 0 \tag{6.16}$$

Equation 6.14 can therefore be rewritten by means of an equivalent phase inductance $L_{eq}$

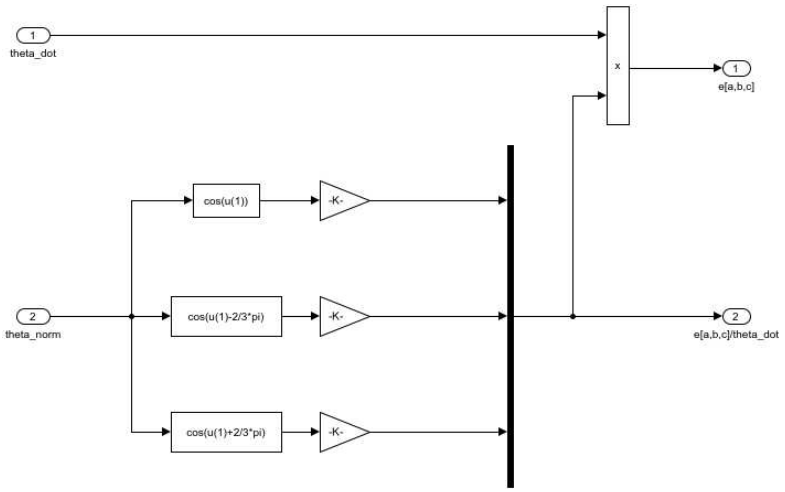


**Figure 6.17:** Simulink diagram of the electric motor subsystem for calculating back-electromotive forces

$$\begin{cases} v_{a0} = R_a i_a + L_{eq,a}\frac{di_a}{dt} + \frac{d\phi_a(\theta_{el})}{dt} \\ v_{b0} = R_b i_b + L_{eq,b}\frac{di_b}{dt} + \frac{d\phi_b(\theta_{el})}{dt} \\ v_{c0} = R_c i_c + L_{eq,c}\frac{di_c}{dt} + \frac{d\phi_c(\theta_{el})}{dt} \end{cases} \tag{6.17}$$

Equation 6.17 was then implemented on Simulink in the second subsystem "Electrical dynamics-backup", as shown in Figure 6.18 . As can be seen, the equivalent resistance and inductance values of each winding are calculated by the "R,L, Computation" subsystem, which defines the values as a function of the temperature reached by the windings, according to the linear expressions given in Equation 6.18.

$$\begin{cases} R_N = R_0(1 + a_r(T_W - T_0)) \\ L_N = L_0(1 + a_L(T_W - T_0)) \end{cases} \tag{6.18}$$

However, given the negligible change in inductance relative to winding temperature, it was determined that its influence can be disregarded, resulting in a value of $a_L$ set to 0 in the Simulink model. Conversely, when considering the impact of resistance variation, $a_r$ is assumed to be 0.00393 °C.Both the value of R and that of L taken from the catalog have been multiplied by $\sqrt{2}/2$ since t.he catalog values are measurements s taken line-to-line in direct current.

By solving the electrical circuit equations, it is then possible to calculate the phase currents $(i_a, i_b, i_c)$ but considering an internal saturation of the integrators. In fact, they cannot exceed the maximum permissible current, calculated in this case as the peak current multiplied by the $\sqrt{2}$

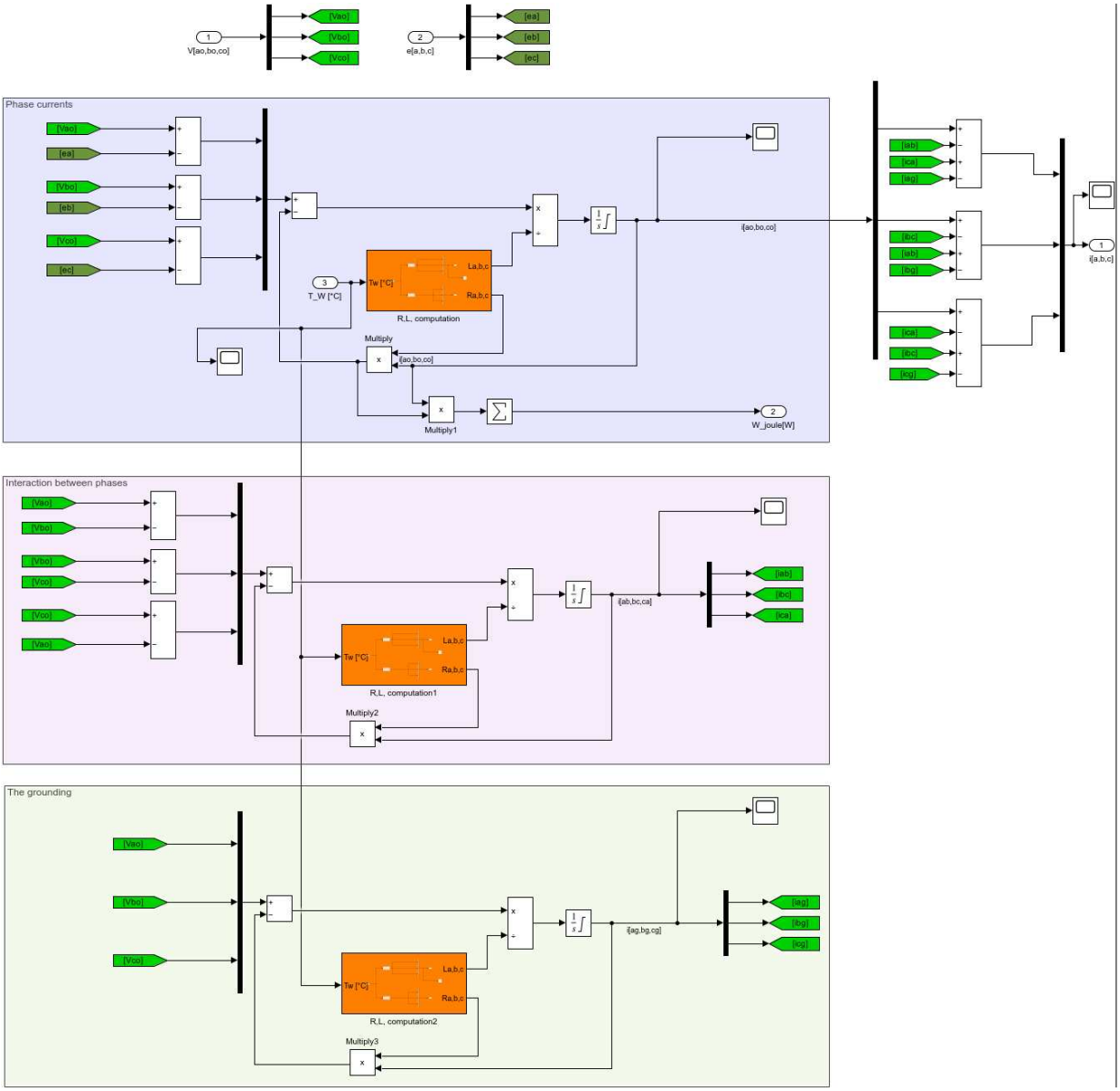


**Figure 6.18:** Simulink diagram of the electric motor subsystem for calculating currents

The diagram in the figure 6.18 demonstrates how the modeling of the electrical dynamics of the motor has actually been further elaborated by considering the interaction between phases and taking into account the grounding.

Regarding the modeling of the interactions between the phases, similar to what was done before, L and R circuits were taken into account. In these circuits, the voltages were calculated by subtracting the phase voltages, while typical values of insulating[4] materials were considered for L and R.

Below are the equations used:

$$\begin{cases} v_{ab} = R_{ab} i_{ab} + L_{ab} \frac{di_{ab}}{dt} \\ v_{bc} = R_{bc} i_{bc} + L_{bc} \frac{di_{bc}}{dt} \\ v_{ca} = R_{ca} i_{ca} + L_{ca} \frac{di_{ca}}{dt} \end{cases} \tag{6.19}$$

where:

$$\begin{cases} v_{ab} = v_{a0} - v_{b0} \\ v_{bc} = v_{b0} - v_{c0} \\ v_{ca} = v_{c0} - v_{a0} \end{cases} \tag{6.20}$$

An additional R, L circuit was considered to account for grounding. However, in aerospace electric motors, there is no grounding wire as the motor structure itself serves as the grounding. In the event of a short circuit between the electric motor and the aircraft structure, the current is discharged through the motor bearings.

$$\begin{cases} v_{a0} = R_{ag} i_{ag} + L_{ag} \frac{di_{ag}}{dt} \\ v_{b0} = R_{bg} i_{bg} + L_{bg} \frac{di_{bg}}{dt} \\ v_{c0} = R_{cg} i_{cg} + L_{cg} \frac{di_{cg}}{dt} \end{cases} \tag{6.21}$$

Finally, considering all contributions with the correct signs, the currents were calculated.

$$\begin{cases} i_a = i_{a0} - i_{ab} + i_{ca} - i_{ag} \\ i_b = i_{b0} - i_{bc} + i_{ab} - i_{bg} \\ i_c = i_{c0} - i_{ca} + i_{bc} - i_{cg} \end{cases} \tag{6.22}$$

Subsequently, the currents are fed into the final subsystem, known as the "Electro-magnetic torque computation." In this stage, the torque produced by the system is determined by taking into account power conservation principles.

$$T_m(t) = \frac{1}{\dot{\theta}} \sum_{k=a,b,c} e_k i_k \tag{6.23}$$

[4]The windings of the motor are separated by insulating material.

However, as this formula was directly implemented within this subsystem, it was deemed unnecessary to include it in the Simulink diagram.

Lastly, the thermal characteristics exhibited by electric motors were examined. Among the primary factors contributing to power dissipation in electric motors is the resistance R encountered by the electrical windings against the flow of current i. Representing the power dissipated due to the Joule effect as $W_j$, it is feasible, in an initial approximation, to describe the dynamics of winding temperature ($T_W$) as follows.

$$W_j = \sum_{k=a,b,c} (Ri_k^2) \tag{6.24}$$

$$W_j - \frac{(T_w - T_h)}{R_{th,w}} = C_{th,w}\frac{dT_w}{dt} \tag{6.25}$$

Here, $T_h$ represents the temperature of the motor housing, $R_{th,w}$ denotes the thermal resistance pertaining to the heat transfer between the windings and the motor structure, and $C_{th,w}$ signifies the thermal capacity of the windings. The housing temperature, in turn, is correlated to the temperature of the surrounding environment ($T_{ext}$) through a similar relationship, in which the thermal resistance $R_{th,h}$ is influenced by factors such as the behavior of the external environment, the presence of fins, and the type of cooling system employed.

$$\frac{(T_w - T_h)}{R_{th,w}} - \frac{(T_h - T_{ext})}{R_{th,w}} = C_{th,h}\frac{dT_w}{dt} \tag{6.26}$$

In terms of the thermal capacities of the windings ($C_{th,w}$, )and the motor housing ($C_{th,h}$), calculations were performed considering copper as the winding material and aluminum as the housing material. These values were determined using Equation 6.1.2 and 6.1.2 respectively. Here, $c_{Cu}$ represents the specific heat of copper (387 J/(kg K)), $M_m$ denotes the mass of the frameless motor, $c_{Al}$ represents the specific heat of aluminum (880 J/(kg K)), and $M_h$ represents the mass of the motor housing. Since the mass of the housing was not listed in the catalog, it was assumed to be one-third of the mass of the frameless motor.

$$C_{th,w} = c_{Cu}M_m \tag{6.27}$$

$$C_{th,h} = c_{Al}M_h \tag{6.28}$$

The complete Simulink model depicting the thermal characteristics of the electric motor, specifically focused on the 'Windings temperature' aspect, has been illustrated in Figure 6.19 .

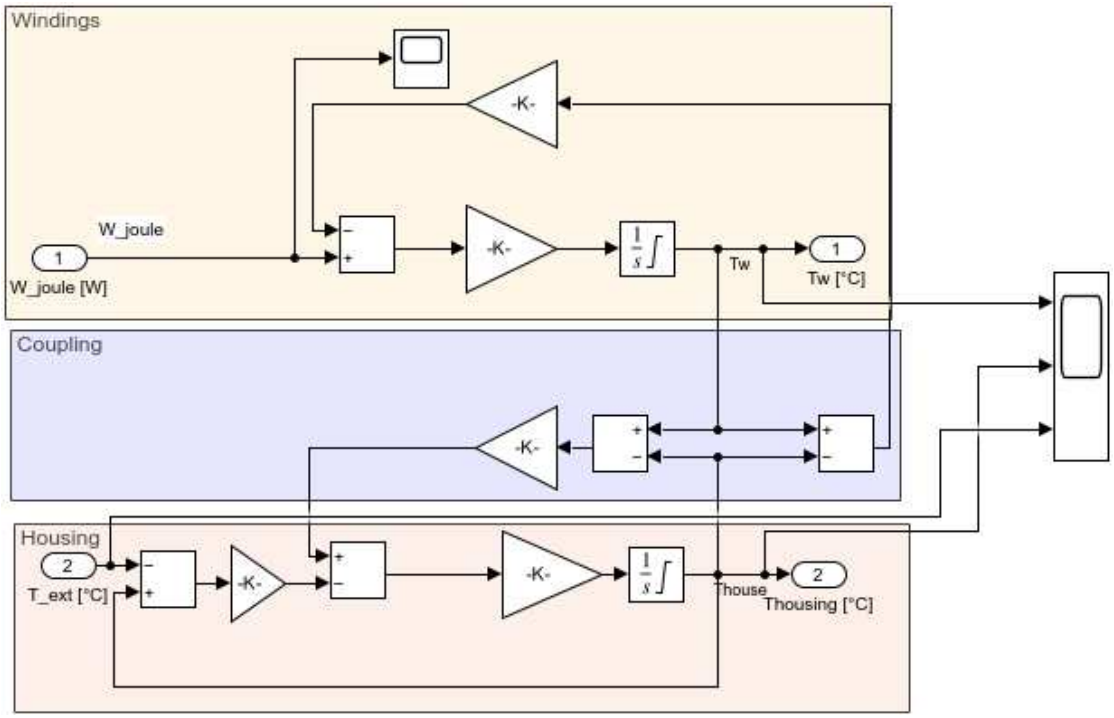


**Figure 6.19:** Simulink model of electric motor thermal phenomena.

After completing the three-phase modeling of the electric motor, in order to ensure the accuracy of the motor's modeling, a decision was made to graphically represent its static mechanical behavior (illustrated in Figure 6.20 as a normalized graph) and compare it with the performance curve provided in Figure 3.7 , extracted from Kollmorgen's catalogue. The points where the two Cartesian axes intersect seem to be similar, confirming the correctness of the model. The irregularities observed in this curve are a result of the incorporation of PWM modulation in the modeling process.

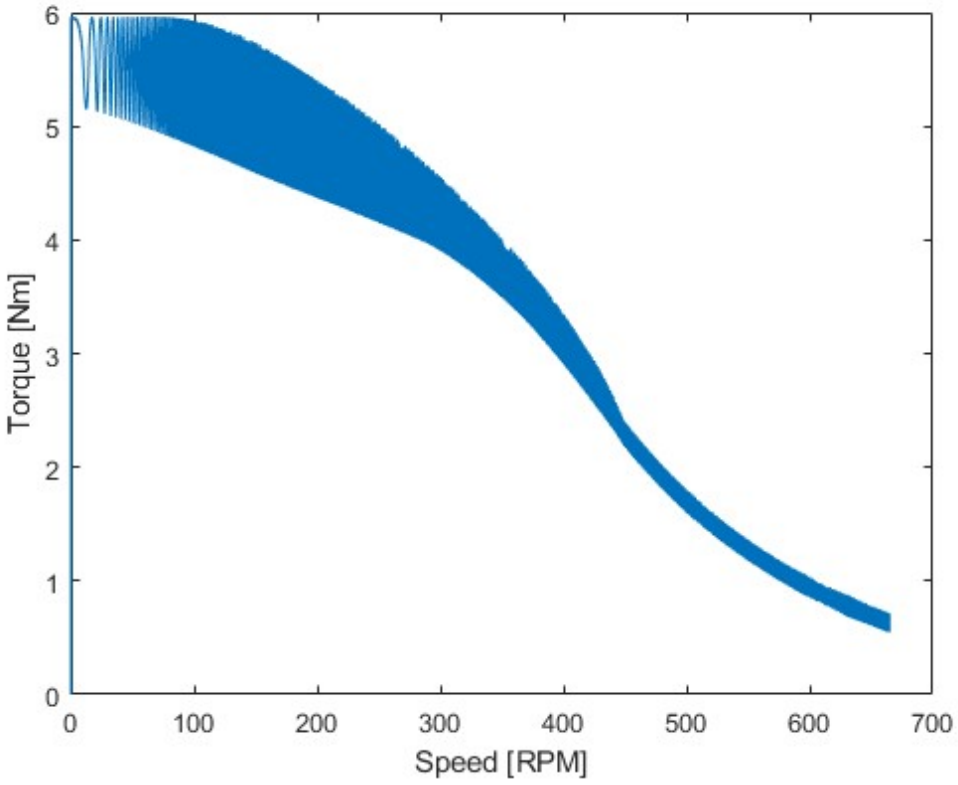


**Figure 6.20:** Mechanical characteristic of the three-phase electric motor model.

### 6.1.3 Mechanical transmission

The Simulink model of the mechanical transmission (as seen in the figure 6.1) takes as input the torque $T_m$ provided by the electric motor and the external force $F_{ext}$ resulting from the interaction between the actuator and the downstream flight control surface. As output, it provides the angular position $\theta_m$ and angular velocity $\dot{\theta}_m$ of the motor, and the linear displacement $x_1$ and linear velocity $\dot{x}_1$ of the screw actuator.

As depicted in the figure 6.21, the mechanical transmission consists of a gearbox and a screw actuator. It can be observed that there are switches to operate the model either with a simplified version of the gearbox, which considers only the gear ratios, or with the more detailed model of the double-stage epicyclic gearbox, the modeling of which will be presented below.

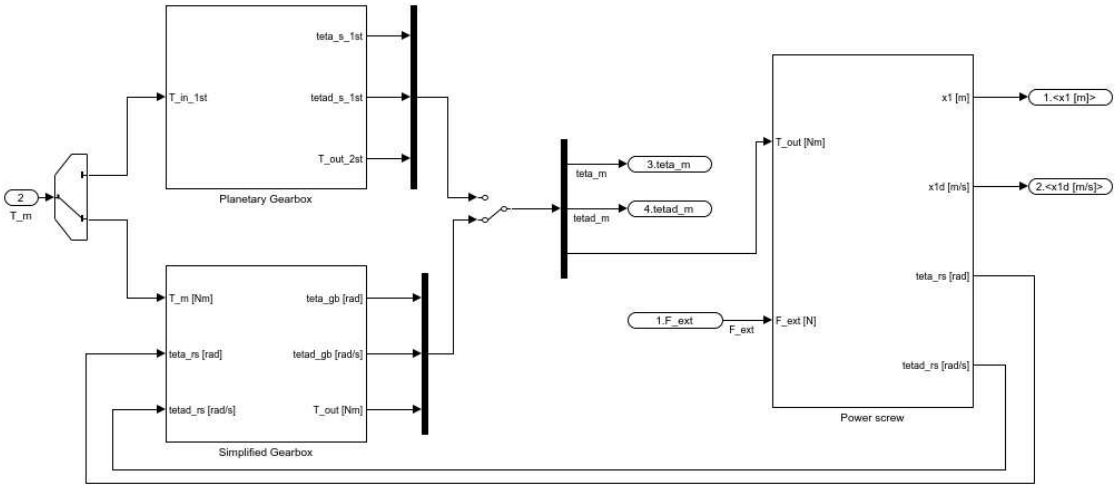


**Figure 6.21:** Simulink model of the mechanical transmission.

### GEARBOX

The following is the modeling of a two-stage planetary gearbox. Specifically, the first stage is presented, while the second stage is the same with only the values changing. The block, as shown in the figure 6.21, takes the motor torque as input and provides the angular position and angular velocity of the sun gear of the first stage of the reducer, which correspond to the motor's angular position and angular velocity, respectively. Finally, it outputs the torque that will be sent to the screw actuator.

To model the planetary gearbox, an elastodynamic analysis has been chosen, which takes into account variables such as:

- the inertia of bodies;
- the stiffness and damping of the bodies;
- the backlash between the bodies;

It is a lumped-parameter model with the variable parameter of mesh stiffness. The mesh stiffness varies depending on the number of teeth in contact, the contact point on the tooth profiles, and the magnitude of the applied torques.

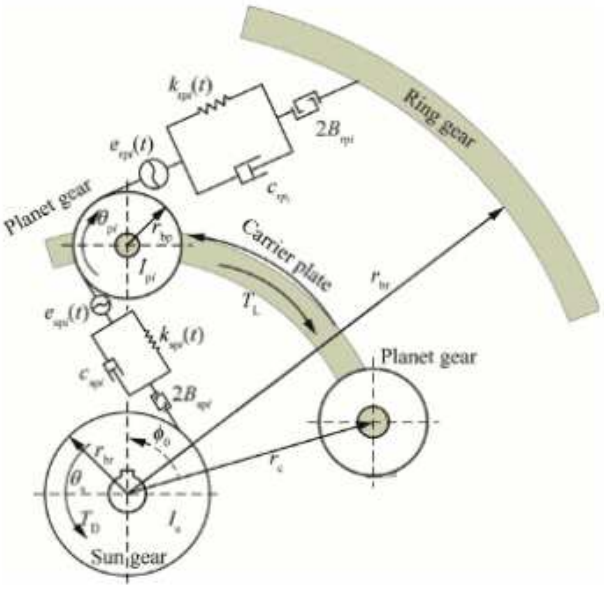


**Figure 6.22:** Dynamic model of a planetary gear train. [11]

As seen in the figure 6.22, the gear stiffness are represented as springs with parallel damping elements to simulate viscous effects.

The developed model makes the following simplifying assumptions:

- Equal and constant gear stiffnesses between the sun and satellites: $k_{sp1} = k_{sp2} = k_{sp3} = k_{sp} =;$
- Equal and constant damping coefficients between the sun and satellites: $c_{sp1} = c_{sp2} = c_{sp3} = c_{sp} =;;$
- Equal and constant gear stiffnesses between the ring and satellites: $k_{rp1} = k_{rp2} = k_{rp3} = k_{rp} =;;$
- Equal and constant damping coefficients between the ring and satellites: $c_{rp1} = c_{rp2} = c_{rp3} = c_{rp} =;;$
- Negligible transmission error: $e_{sp} \simeq 0, e_{sp} \simeq 0;$
- Constant pressure angle between the sun and satellites: $\alpha_{sp}$, and constant pressure angle between the ring and satellites: $\alpha_{rp}$.

The following are the equations of motion, considering the 5 degrees of freedom of the gear reducer: rotation of the sun gear, rotations of the 3 satellites, and rotation of the carrier, while the ring gear is assumed to be fixed.

**Equilibrium of the sun gear rotation.**

$$T_D + T_{att,s,p1} + T_{att,s,p2} + T_{att,s,p3} - r_{bs} \cdot (c_{sp1}\dot{\delta}_{sp1} + c_{sp2}\dot{\delta}_{sp2} + c_{sp3}\dot{\delta}_{sp3}) -$$

$$\mathrm{r}_{bs} \cdot (k_{sp1} \cdot f(\delta_{sp1}, B_{sp1}) + k_{sp2} \cdot f(\delta_{sp2}, B_{sp2}) + k_{sp3} \cdot f(\delta_{sp3}, B_{sp3})) = I_{sol} \cdot \ddot{\theta}_s \quad (6.29)$$

**Equilibrium of the relative rotation of the three satellites with respect to the carrier.**

$$(k_{sp1}\cdot f(\delta_{sp1}, B_{sp1}) - k_{rp1}\cdot f(\delta_{rp1}, B_{rp1}))\cdot r_{bp} + (c_{sp1}\dot{\delta}_{sp1} - c_{rp1}\dot{\delta}_{rp1})\cdot r_{bp} - T_{att,p1,s} - T_{att,p1,r} = I_{sat}\cdot\ddot{\theta}_{pi_c} \quad (6.30)$$

$$(k_{sp2}\cdot f(\delta_{sp2}, B_{sp2}) - k_{rp2}\cdot f(\delta_{rp2}, B_{rp2}))\cdot r_{bp} + (c_{sp2}\dot{\delta}_{sp2} - c_{rp2}\dot{\delta}_{rp2})\cdot r_{bp} - T_{att,p2,s} - T_{att,p2,r} = I_{sat}\cdot\ddot{\theta}_{p2_c} \quad (6.31)$$

$$(k_{sp3}\cdot f(\delta_{sp3}, B_{sp3}) - k_{rp3}\cdot f(\delta_{rp3}, B_{rp3}))\cdot r_{bp} + (c_{sp3}\dot{\delta}_{sp3} - c_{rp3}\dot{\delta}_{rp3})\cdot r_{bp} - T_{att,p3,s} - T_{att,p3,r} = I_{sat}\cdot\ddot{\theta}_{p3_c} \quad (6.32)$$

**Equilibrium of the carrier rotation (or satellite carrier).**

The tangential gear forces between the sun gear and satellites, as well as between the ring gear and satellites, are transmitted to the satellite shaft, exerting a torque on the carrier shaft that opposes the resisting torque $T_L$.

$$(c_{sp1}\dot{\delta}_{sp1}\cdot r_c\cdot cos(\alpha_{sp})+c_{rp1}\dot{\delta}_{rp1}\cdot r_c\cdot cos(\alpha_{rp})+c_{sp2}\dot{\delta}_{sp2}\cdot r_c\cdot cos(\alpha_{sp})+c_{rp2}\dot{\delta}_{rp2}\cdot r_c\cdot cos(\alpha_{rp})+$$

$$c_{sp3}\dot{\delta}_{sp3}\cdot r_c\cdot cos(\alpha_{sp})+c_{rp3}\dot{\delta}_{rp3}\cdot r_c\cdot cos(\alpha_{rp}))+(k_{sp1}\cdot f(\delta_{sp1},B_{sp1})\cdot r_c\cdot cos(\alpha_{sp})+k_{rp1}\cdot f(\delta_{rp1},B_{rp1})\cdot r_c\cdot cos(\alpha_{rp})+k_{sp2}\cdot f(\delta_{sp2},B_{sp2})\cdot r_c\cdot cos(\alpha_{sp})+k_{rp2}\cdot f(\delta_{rp2},B_{rp2})\cdot r_c\cdot cos(\alpha_{rp})+k_{sp3}\cdot f(\delta_{sp3},B_{sp3})\cdot r_c\cdot cos(\alpha_{sp})+k_{rp1}\cdot f(\delta_{rp3},B_{rp3})\cdot r_c\cdot cos(\alpha_{rp}))-T_L=I_car\cdot\ddot{\theta}_{car} \quad (6.33)$$

The quantities that appear in the equations of motion are:

- $T_D$ Solar input torque [Nm];
- $T_L$ Torque resistant to the satellite carrier [Nm];
- $r_{bp}$ base radius planets [m];
- $r_{br}$ base radius crown [m];
- $r_{bs}$ base radius solar [m];
- $r_c$ radius satellite carrier [m];
- $k_{sp}$ stiffness of solar-planet meshing [N/m];
- $k_{rp}$ stiffness of crown-planet meshing [N/m];
- $c_{sp}$ solar-planets viscous damping coefficient [kg/s];
- $c_{rp}$ crown-planets viscous damping coefficient [kg/s];
- $f(\delta_{sp}, B_{sp})$ solar-planet backlash function;
- $f(\delta_{rp}, B_{rp})$ crown-planet backlash function;

The following diagram shows the Simulink block that implements these equations for the first stage of the planetary gearbox.

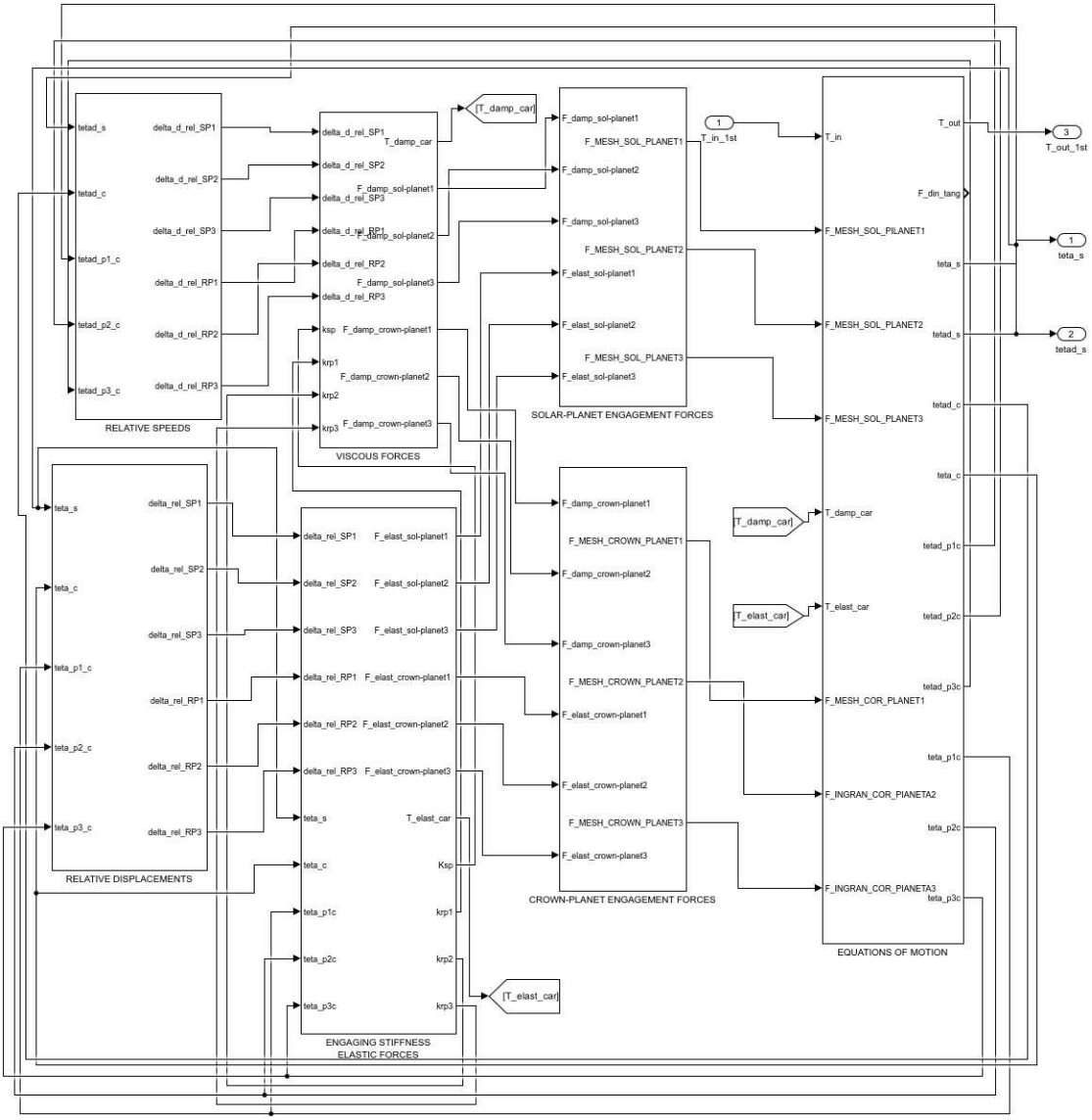


**Figure 6.23:** Simulink scheme of first stage planetary gearbox.

As shown in the diagram 6.23, moving from left to right, the calculations begin with the determination of relative displacements and velocities. Then, the viscous forces and elastic gear forces are computed. Next, the calculations proceed to determine solar-planet engagement forces and crown-planet engagement forces . Finally, there is a block that implements the equations of motion, which also includes the calculation of friction forces.

The relative displacements and their derivatives along the solar-satellite line of action and crown-satellite were calculated as follows:

$$\delta_{sp1} = r_{bs} \cdot (\theta_s - \theta_{car}) - r_{bp} \cdot \theta_{p1,c} \tag{6.34}$$
$$\dot{\delta}_{sp1} = r_{bs} \cdot (\dot{\theta}_s - \dot{\theta}_{car}) - r_{bp} \cdot \dot{\theta}_{p1,c} \tag{6.35}$$

$$\delta_{sp2} = r_{bs} \cdot (\theta_s - \theta_{car}) - r_{bp} \cdot \theta_{p2,c} \tag{6.36}$$
$$\dot{\delta}_{sp2} = r_{bs} \cdot (\dot{\theta}_s - \dot{\theta}_{car}) - r_{bp} \cdot \dot{\theta}_{p2,c} \tag{6.37}$$

$$\delta_{sp3} = r_{bs} \cdot (\theta_s - \theta_{car}) - r_{bp} \cdot \theta_{p3,c} \tag{6.38}$$
$$\dot{\delta}_{sp3} = r_{bs} \cdot (\dot{\theta}_s - \dot{\theta}_{car}) - r_{bp} \cdot \dot{\theta}_{p3,c} \tag{6.39}$$

$$\delta_{rp1} = r_{bp} \cdot \theta_{p1,c} - r_{br} \cdot \theta_{car} \tag{6.40}$$
$$\dot{\delta}_{sp1} = r_{bp} \cdot \dot{\theta}_{p1,c} - r_{br} \cdot \dot{\theta}_{car} \tag{6.41}$$

$$\delta_{rp2} = r_{bp} \cdot \theta_{p2,c} - r_{br} \cdot \theta_{car} \tag{6.42}$$
$$\dot{\delta}_{sp2} = r_{bp} \cdot \dot{\theta}_{p2,c} - r_{br} \cdot \dot{\theta}_{car} \tag{6.43}$$

$$\delta_{rp3} = r_{bp} \cdot \theta_{p3,c} - r_{br} \cdot \theta_{car} \tag{6.44}$$
$$\dot{\delta}_{sp3} = r_{bp} \cdot \dot{\theta}_{p3,c} - r_{br} \cdot \dot{\theta}_{car} \tag{6.45}$$

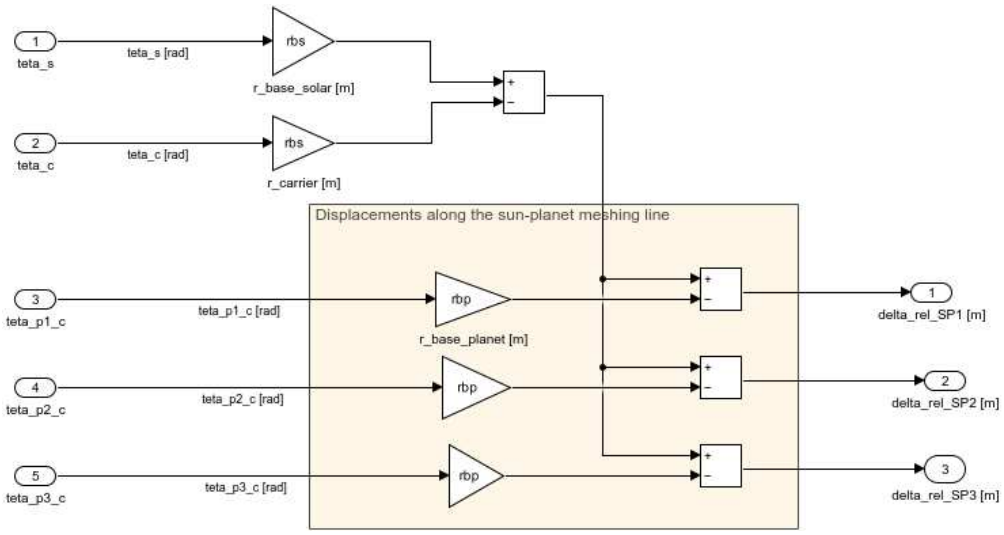


**Figure 6.24:** Calculation of relative displacements between the sun gear and planets.

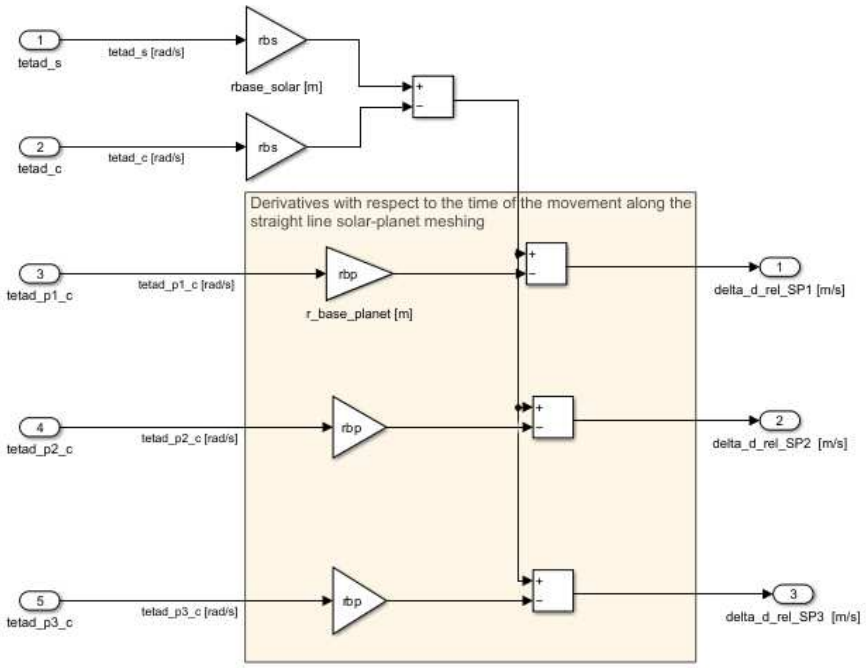


**Figure 6.25:** Calculation of relative displacements derivatives between the sun gear and planets.

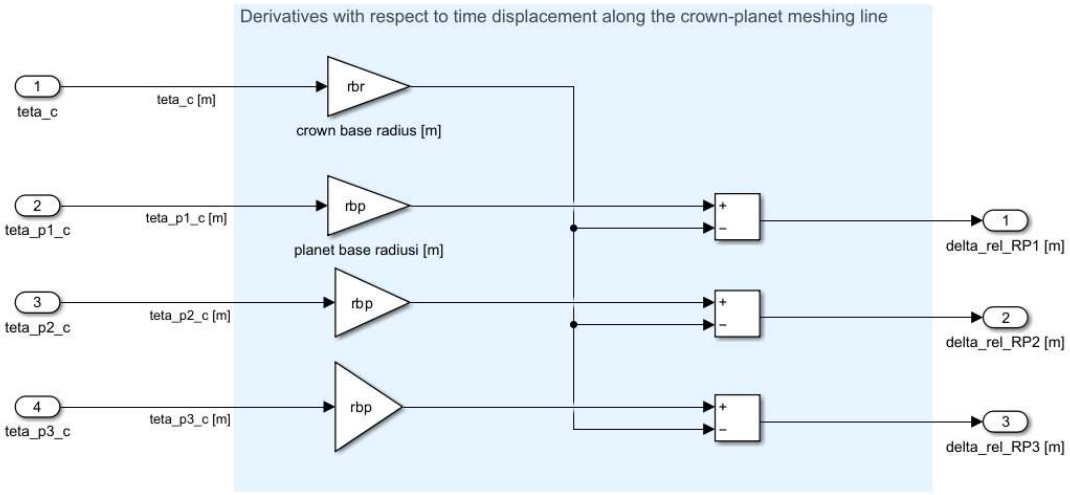


**Figure 6.26:** Calculation of relative displacement between crown and planets.

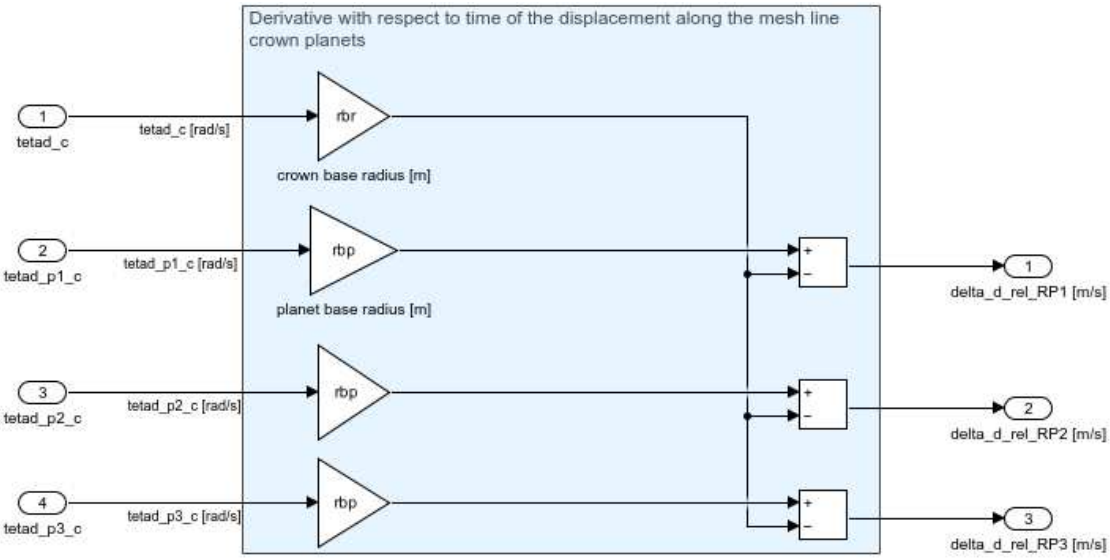


**Figure 6.27:** Calculation of relative displacement derivatives between the sun gear and planets.

A backlash function is applied to the relative movements between the sun-planet and the ring-planet along the meshing line. Backlash represents the clearance between two adjacent movable parts. This phenomenon is particularly evident in mechanical systems equipped with a driving member and a driven member that are not directly interconnected. In other words, the motor shaft and the load shaft are connected to each other through gears. The function representing the backlash phenomenon can be expressed as:

$$f(\delta, B) = \begin{cases} \delta - B & if \quad \delta > B \\ 0 & elseif \quad -B < \delta < B \\ \delta + B & else \quad \delta < -B \end{cases} \tag{6.46}$$

In Figure 6.28, the implementation of the backlash function is depicted, modeled using an if-elseif-else construct within the Simulink environment.

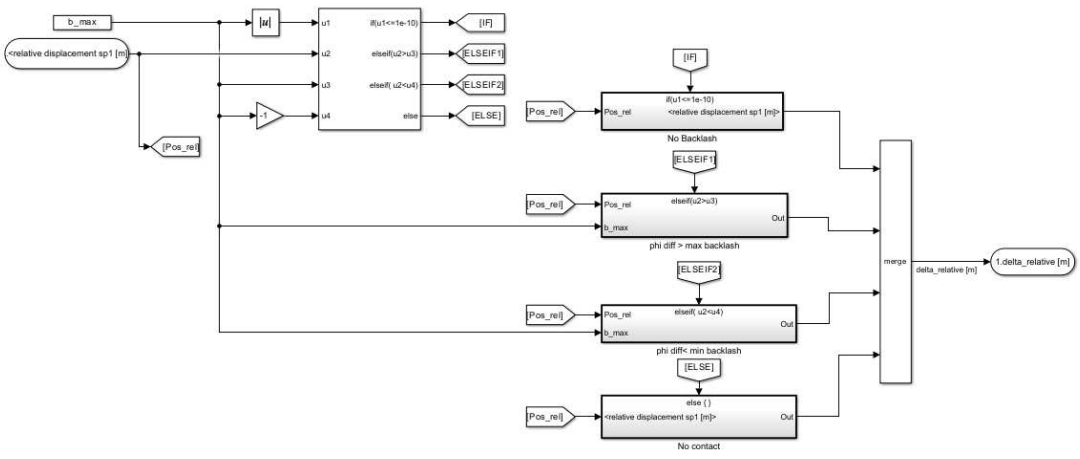


**Figure 6.28:** Backlash function in simulink environment-solar planet 1

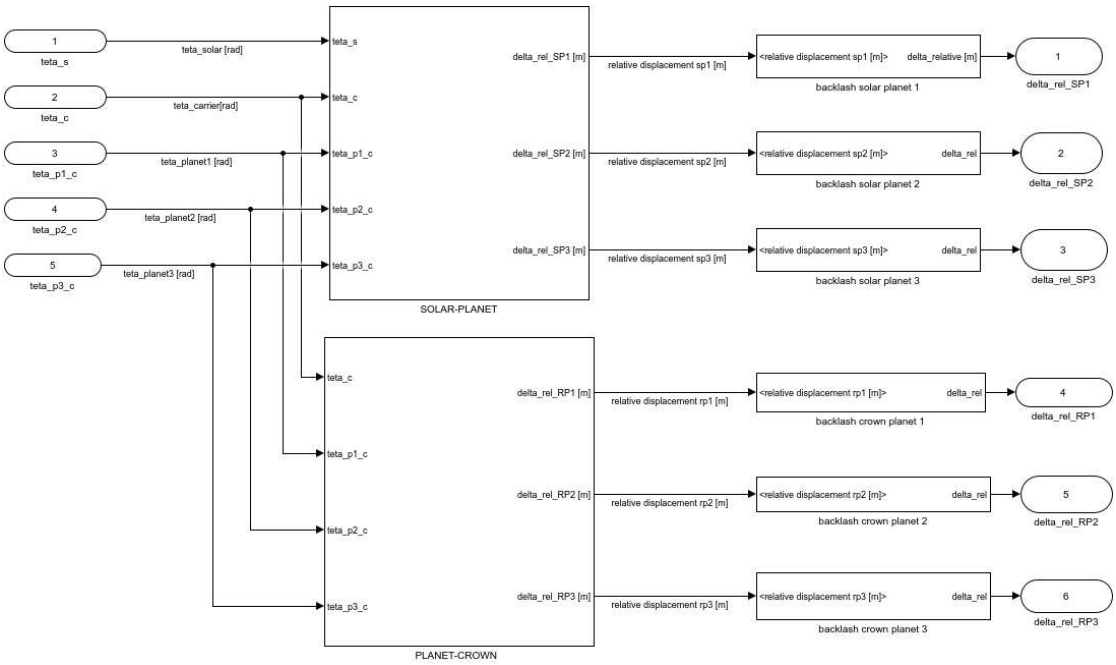


**Figure 6.29:** Backlash for the gear mesh in the Simulink environment.

Continuing with the description of the system in Figure 6.23, we move on to the calculation of the viscous meshing forces and the elastic meshing forces. The equation 6.1.3 can be simplified as follows. The values of $T_{damp,car}$ and $T_{elast,car}$ are calculated in these blocks.

$$T_{damp,car} + T_{elast,var} - T_L = I_{car} \cdot \ddot{\theta}_{car} \tag{6.47}$$

**CALCULATION OF THE VISCOUS FORCES**

$$F_{damp,sol-planet1} = c_{sp1} \cdot \dot{\delta}_{sp1} \tag{6.48}$$

$$F_{damp,sol-planet2} = c_{sp2} \cdot \dot{\delta}_{sp2} \tag{6.49}$$

$$F_{damp,sol-planet3} = c_{sp3} \cdot \dot{\delta}_{sp3} \tag{6.50}$$

$$F_{damp,crown-planet1} = c_{rp1} \cdot \dot{\delta}_{rp1} \tag{6.51}$$

$$F_{damp,crown-planet2} = c_{rp2} \cdot \dot{\delta}_{rp2} \tag{6.52}$$

$$F_{damp,crown-planet3} = c_{rp3} \cdot \dot{\delta}_{rp3} \tag{6.53}$$

$$T_{damp,car} = r_{bc} \cdot (F_{damp,sol-planet1} + F_{damp,sol-planet2} + F_{damp,sol-planet3} +$$

$$\mathrm{F}_{damp,crown-planet1} + F_{damp,crown-planet2} + F_{damp,crown-planet3}) \tag{6.54}$$

Figure 6.30 shows the Simulink diagram that implements these formulas.

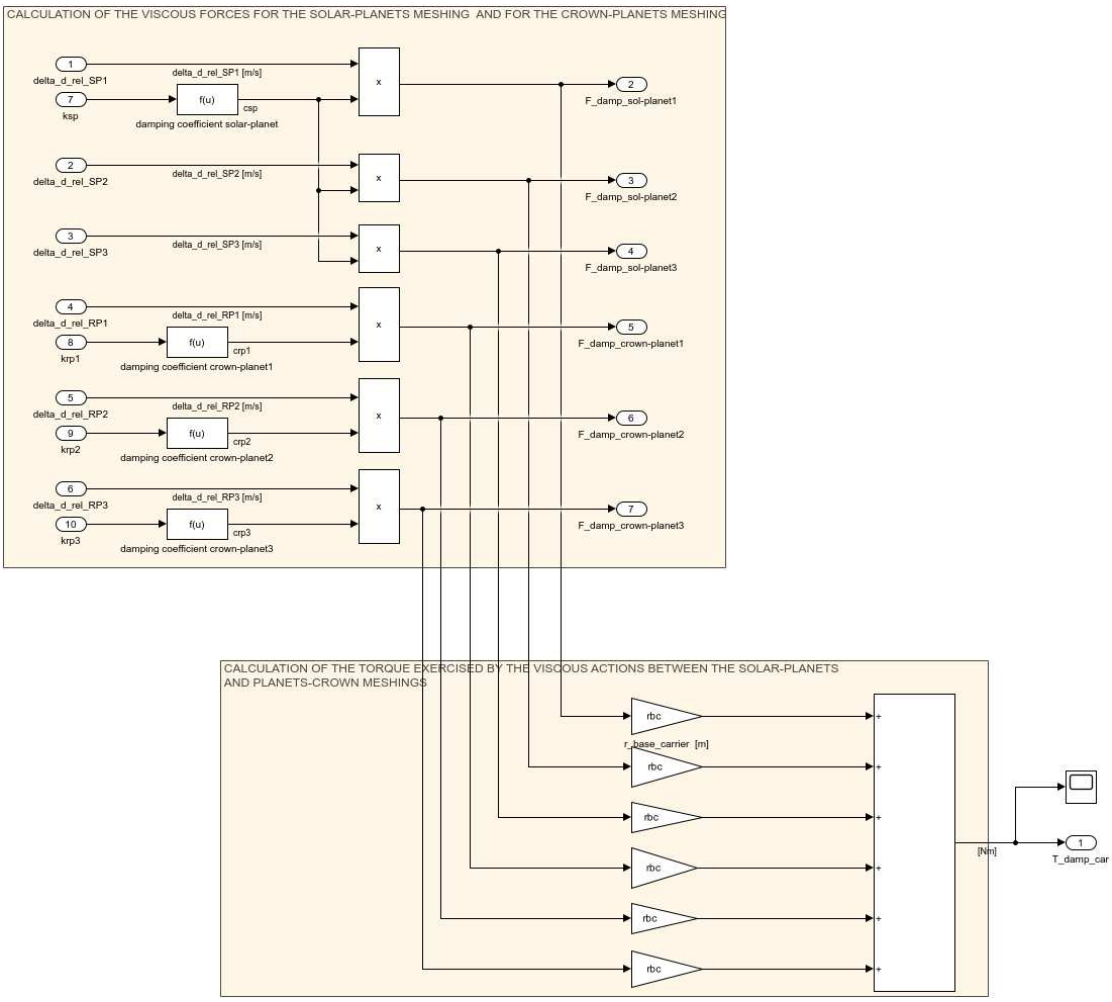


**Figure 6.30:** Simulink- Calculation of viscous forces of engagement.

The damping coefficients are functions of the meshing stiffness and are calculated using the following formulas.

$$c_{sp} = 2 \cdot eps \cdot \sqrt{\frac{k_{sp} \cdot m_{sol} \cdot m_{sat}}{m_{sol} + m_{sat}}} \tag{6.55}$$

$$c_{rp} = 2 \cdot eps \cdot \sqrt{k_{rp} \cdot m_{sat}} \tag{6.56}$$

with esp, contact damping ratio between the teeth, equal to:

$$eps = \frac{0.03 + 0.17}{2} \tag{6.57}$$

## CALCULATION OF THE ELASTIC FORCES

$$F_{elast,sol-planet1} = k_{sp1} \cdot \delta_{sp1} \tag{6.58}$$

$$F_{delast,sol-planet2} = k_{sp2} \cdot \delta_{sp2} \tag{6.59}$$

$$F_{elast,sol-planet3} = k_{sp3} \cdot \delta_{sp3} \tag{6.60}$$

$$F_{elast,crown-planet1} = k_{rp1} \cdot \delta_{rp1} \tag{6.61}$$

$$F_{ekast,crown-planet2} = k_{rp2} \cdot \delta_{rp2} \tag{6.62}$$

$$F_{elast,crown-planet3} = k_{rp3} \cdot \delta_{rp3} \tag{6.63}$$

$$T_{elast,car} = r_{bc} \cdot (F_{elast,sol-planet1} + F_{elast,sol-planet2} + F_{damp,sol-planet3} +$$

$F_{elast,crown-planet1} + F_{elast,crown-planet2} + F_{elast,crown-planet3}$)(6.64)

Figure 6.31 shows the Simulink diagram that implements these formulas.

Gear mesh stiffness refers to the ratio between the tangential force along the line of action and the deflection of the tooth in that direction. Stiffness is defined as the force required to deform a tooth by 1 meter along the line of action, with a tooth width of 1 meter ([N/m/m]). Since the applied force on a tooth varies in terms of magnitude, direction, and point of application, the deflection of the tooth is continuously variable. Therefore, the variability of gear mesh stiffness depends on both the variability of the tangential force (magnitude, direction, and sense) and the fact that the number of teeth in contact (degree of contact) varies during meshing.

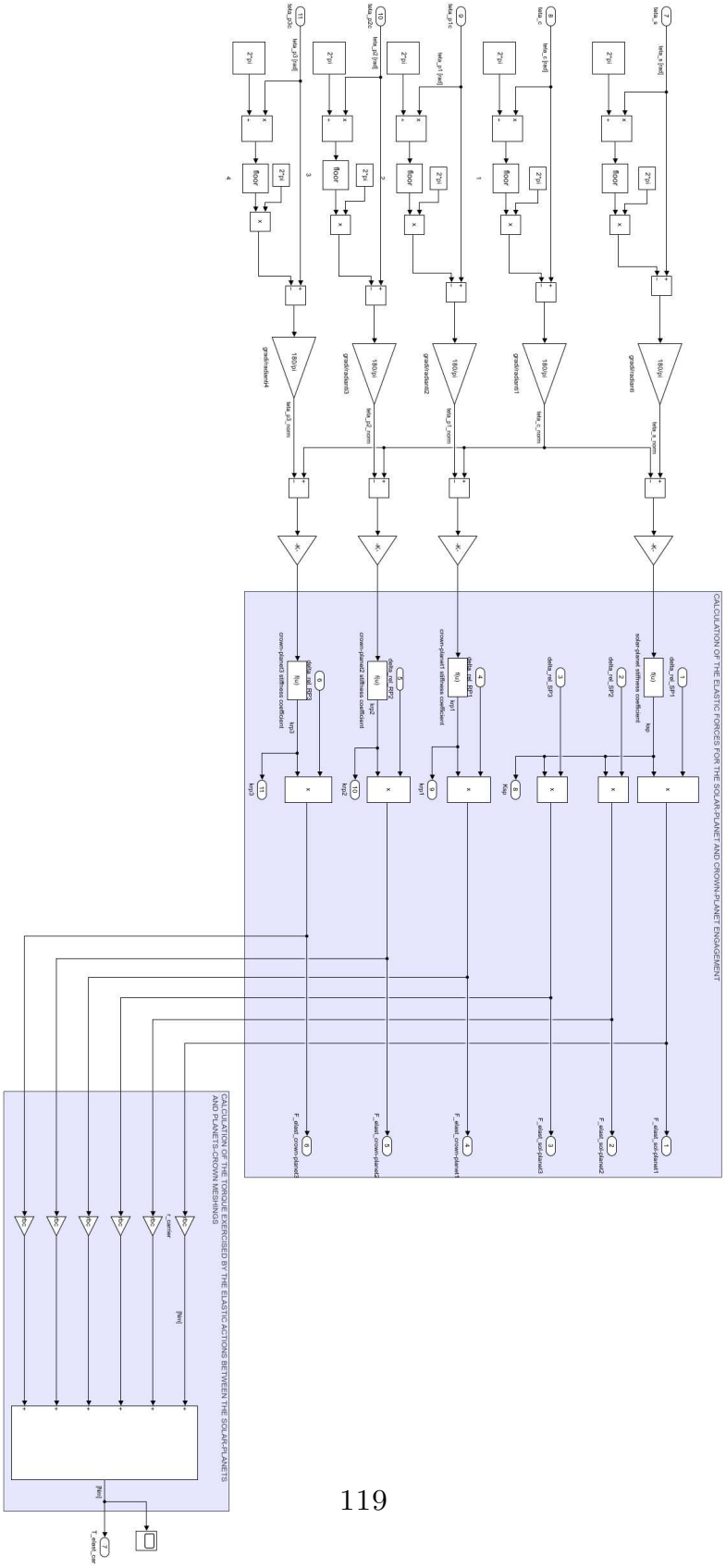




**Figure 6.31:** Simulink- Calculation of elastic forces of engagement.

*Kuang Yang model*

In this first simplified model, the analytical methodology proposed by Kuang and Yang was adopted for the calculation of gear mesh stiffness.

Following analysis performed with a finite element model, an interpolating curve was derived to determine the stiffness for spur gears, using the following expression:

$$K_i(r_i) = 10^9 \cdot (A_0 + A_1 \cdot X_i) + (A_2 + A_3 \cdot X_i) \cdot \frac{r_i - R_i}{(1 - X_i) \cdot m} \tag{6.65}$$

$K_i(r_i)$ represents the stiffness of the tooth of the i-th gear when contact occurs at the point defined by the radius. The variables $r_i, X_i, R_i, m$ and m represent the relative radius at the load position, the profile shift coefficient, the pitch radius of the gear, and the module of the gear, respectively. The coefficients A0, A1, A2, and A3, which depend on the number of teeth of the gear ($z_i$), are determined as follows:

$$A_0 = 3.867 + 1.612 \cdot Z_i - 0.02916 \cdot (Z_i^2) + 0.0001553 \cdot (Z_i^3); \tag{6.66}$$

$$A_1 = 17.060 + 0.7289 \cdot Z_i - 0.01728 \cdot (Z_i^2) + 0.00009993 \cdot (Z_i^3); \tag{6.67}$$

$$A_2 = 2.637 - 1.222 \cdot Z_i + 0.02217 \cdot (Z_i^2) - 0.0001179 \cdot (Z_i^3); \tag{6.68}$$

$$A_3 = -6.330 - 1.033 \cdot Z_i + 0.02068 \cdot (Z_i^2) - 0.0001130 \cdot (Z_i^3); \tag{6.69}$$

This formulation does not take into account the deformations induced in the adjacent teeth to the one in contact. Once the $K_i$ for the generic tooth is defined, the calculation of the stiffness of the individual gear pair, denoted as Kc, is carried out. Since the constant Ki represents the flexural stiffness of the tooth, in a dynamic model with concentrated parameters, it can be represented by a spring. The meshing between two teeth is therefore represented by two springs in series with constant stiffness, K1 and K2. Consequently, the stiffness of the individual gear pair in contact, denoted as Kc, is derived as the equivalent stiffness of the series arrangement of springs K1 and K2.

$$K_c = \frac{K_1 + K_2}{k_1 + K_2} \tag{6.70}$$

As a first attempt, a constant stiffness value was used, without considering the variation of stiffness based on the load applied to the tooth or the change in the number of teeth in contact during meshing.

$$K_{sp} = (0.75 \cdot \epsilon + 0.25) \cdot K_C b_{sol} \tag{6.71}$$

$$K_{rp} = (0.75 \cdot \epsilon + 0.25) \cdot K_C b_{ring} \tag{6.72}$$

where:

- $K_C$ is the stiffness of a gear pair in contact;
- $\epsilon$ is the degree of contact ratio;
- $b_{sol}$ is the face width of the sun gear;
- $b_{ring}$ is the ace width of the crown gear.

The multiple gear meshes in planetary gear systems have a variable number of teeth in contact, all operating at the same mesh frequency. All sun-planet meshes have the same shape and periodicity in the variation of the number of teeth in contact, but these variations are not generally in phase with each other. In other words, there is a phase difference between the number of teeth in contact of different gear meshes. The same phenomenon occurs in ring-planet meshes. Additionally, there is a phase difference between the sun-planet meshes and the ring-planet meshes.

The phase differences between the different planets are as follows:

- $\gamma_{sn}$ The relative phase difference between the sun-planet mesh of the nth pair and the first sun-planet mesh;
- $\gamma_{rn}$ The relative phase difference between the ring-planet mesh of the nth pair and the first ring-planet mesh;
- $_{rs}$ The relative phase difference between the nth sun-planet mesh and the ring-planet mesh.

To determine $\gamma_{sn}$, we imagine fixing the sun gear. After a complete rotation of the carrier, the first planet will have completed a rotation of $2\pi$ around the axis of the sun gear and will have come into contact with all its teeth. Therefore, with a rotation of the carrier $\Psi_n$, the same planet will come into contact with a number of sun gear teeth equal to $\frac{z_{sol}\cdot\Psi_n}{2\pi}$. A similar reasoning applies to the determination of $\gamma_{rn}$.

The phase differences between the planets are then determined using the following relationships (Considering counterclockwise rotation of the planets):

$$\gamma_{sn} = -\frac{z_{sol}\cdot\Psi_n}{2\pi} \tag{6.73}$$

$$\gamma_{rn} = \frac{z_{ring}\cdot\Psi_n}{2\pi} \tag{6.74}$$

with:

- $z_{sol} and z_{ring}$ number of teeth of solar and ring

- $\Psi_n$ is the angle of rotation of the carrier that brings the first planet to the initial position of the nth planet.

The angle $\Psi_n$ is defined as:

$$\Psi_n = p_n \frac{2\pi}{z_{ring} z_{sol}} \tag{6.75}$$

The mesh stiffnesses $K_{sp}$ and $k_{rp}$ depend on the angular position of the planet-sun and planet-ring gear pairs and are not constant along the line of contact. By introducing the phase differences in the meshing of the planets, $\gamma_{sp}$ and $\gamma_{rp}$, we have:

$$K_{sp} = K_{sp} \cdot (\theta + \gamma_{sp}) \qquad with \quad \theta = (\theta_{sol} - \theta_{car}) \cdot \frac{z_{sol}}{2\pi} \tag{6.76}$$

$$K_{rp} = K_{rp} \cdot (\theta + \gamma_{rp}) \qquad with \quad \theta = (\theta_{car} - \theta_{planet}) \cdot \frac{z_{plan}}{2\pi} \tag{6.77}$$

However, the assumption remains that only one pair of teeth is in contact.

Moving to the right in the diagram 6.23, we proceed to calculate the solar-planet mesh forces and the ring-planet mesh forces.

$$F_{mesh,sol-planet1} = F_{damp,sol-planet1} + F_{elast,sol_planet1} \tag{6.78}$$

$$F_{mesh,sol-planet2} = F_{damp,sol-planet2} + F_{elast,sol_planet2} \tag{6.79}$$

$$F_{mesh,sol-planet3} = F_{damp,sol-planet3} + F_{elast,sol_planet3} \tag{6.80}$$

$$F_{mesh,crown-planet1} = F_{damp,crown-planet1} + F_{elast,crown_planet1} \tag{6.81}$$

$$F_{mesh,crown-planet2} = F_{damp,crown-planet2} + F_{elast,crown_planet2} \tag{6.82}$$

$$F_{mesh,crown-planet3} = F_{damp,crown-planet3} + F_{elast,crown_planet3} \tag{6.83}$$

Since they are simple sums, the Simulink diagrams are not shown.

Finally, in the last block on the right side of the diagram 6.23, the equations of motion (6.28 6.30 6.31 6.32 6.47) are implemented.

The frictional torques in these equations vary during meshing because the position of contact point along the line of action changes, resulting in a change in the lever arm of the frictional force. The lever arm of friction depends on the values of the radii of curvature . These frictional torques have the following expression:

$$T_{att,sp} = (\mu_{sol,sat} \cdot F_{sp} \cdot sign(V_{sp})\rho_{1,sol} \tag{6.84}$$

$$T_{att,ps} = (\mu_{sol,sat} \cdot F_{sp} \cdot sign(V_{sp})\rho_{2,sat} \tag{6.85}$$

$$T_{att,pr} = (\mu_{ring,sat} \cdot F_{rp} \cdot sign(V_{rp})\rho_{1,sat} \tag{6.86}$$

As shown in the diagram 6.32, the leftmost block implements the equations of rotational equilibrium for the wheels, while the remaining blocks handle the modeling of friction.

The power losses associated with gear teeth can be divided into two main groups:

- Load-dependent losses
- Load-independent losses

Among the load-dependent losses, the following can be listed:

- Losses caused by sliding between the teeth in contact.
- Friction losses generated by viscous shear of the lubricant film and direct interaction between the surface asperities in contact (mixed lubrication regime).

The friction model presented below provides detailed modeling of both types of losses.

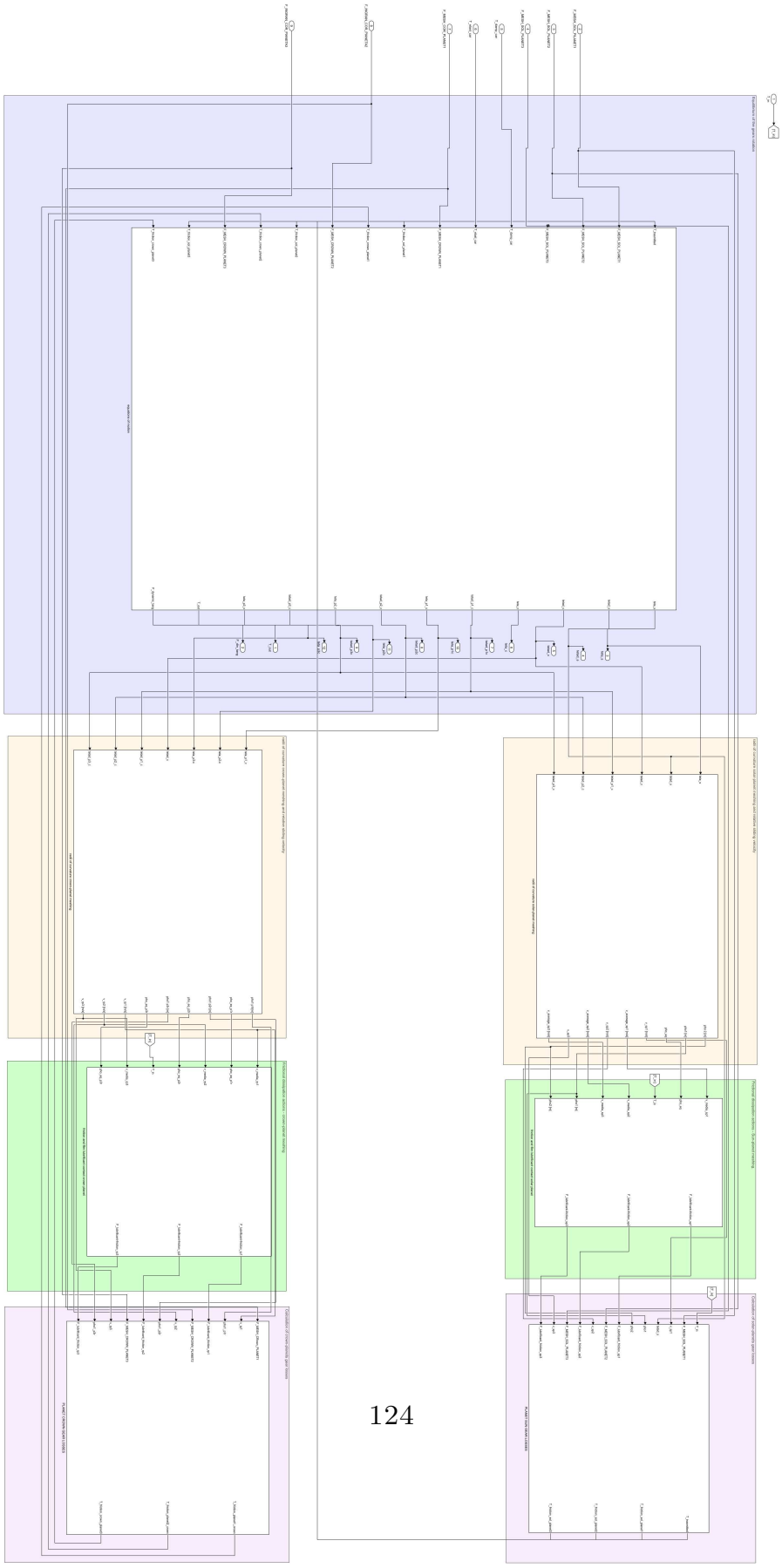



**Figure 6.32:** Simulink- Equations of motion.

**Losses due to tooth sliding in contact**

Regarding the losses caused by tooth sliding in contact, it is necessary to consider that the force exchanged between the teeth has two components: one normal to the tooth surface and one tangential to it, in the direction of the relative velocity between the two teeth. During meshing, pure rolling motion occurs only at the point of contact between the pitch circles of the two gears. In the upper and lower regions, there is sliding in the direction of the tooth height. This phenomenon generates a component of tangential friction force between the meshing teeth, denoted as $F_{att}(t)$, which exerts a variable moment arm depending on the position of the contact point along the line of action.

$$F_{att}(t) = \mu \cdot F_n(t) \tag{6.87}$$

With:

- $\mu$ as the coefficient of friction [-];
- $F_n(t)$ as the force exchanged by the teeth during meshing and directed along the line of action [N];
- $F_{att}(t)$ as the tangential friction force orthogonal to the line of action [N].

The coefficient $\mu$ is considered constant during meshing, but it is necessary to take into account the change in sign with the direction of the relative sliding velocity $V_S$.

$$\mu = \mu_0 \cdot sign(V_S) \begin{cases} \mu_0 & if \quad V_S > 0 \\ -\mu_0 & if \quad V_S < 0 \end{cases} \tag{6.88}$$

The change in direction of the friction force can trigger vibration. This phenomenon is particularly influential in gears with straight teeth, while it is negligible in the case of gears with helical teeth.

In order to simulate the presence of tangential friction during meshing, the following steps have been followed:

- Estimation of the coefficient of friction $\mu_0$;
- Calculation of the contact geometry, obtaining the expressions for the radii of curvature of the gears;
- Determination of the expression for the relative sliding velocity of the two profiles along the contact segment;
- Calculation of the friction torque exerted by $F_{att}(t)$

Regarding the evaluation of the coefficient of friction, it should be emphasized that the value of the coefficient is not constant during meshing. It varies both with the displacement of the contact point along the line of action and depending on the operating conditions such as dynamic viscosity of the lubricant, contact force, etc. In order to simplify the system modeling, a constant coefficient of friction is considered, obtained from the average of the values assumed along the meshing segment.

For the calculation, the ISO/TR 14179-2 standard has been adopted, applied to both sun-planet and ring-planet contacts. The following formulas are used:

$$\mu_{sol-sat} = 0.048 \cdot \left( \frac{F_{sol-sat}/b}{V_{tot,c}\rho_{sol-sat}} \right)^2 \cdot \eta^{-0.05} R_{am}^{0.25} \cdot X_L \tag{6.89}$$

Where:

- $F_{sol-sat}/b$ is the contact force between the solar and planet per unit length [N/mm];
- $\eta$ is the dynamic viscosity of the oil at the operating temperature $[mPa \cdot s]$
- $R_{am}$ is the arithmetic mean of the surface roughness, equal to $\frac{1}{2} \cdot (R_{a1} + R_{a2})[\mu m]$;
- is the radius of curvature of the pitch point [mm];
- $X_L$ is a factor related to the type of lubricant [-] and is set to 1;
- $V_{tot,c}$ is the sum of velocities at the pitch point [m/s];
- b is the tooth face width [mm].

For the ring-planet contact:

$$\mu_{ring-sat} = 0.048 \cdot \left( \frac{F_{crown-sat}/b}{V_{tot,c}\rho_{crown-sat}} \right)^2 \cdot \eta^{-0.05} R_{am}^{0.25} \cdot X_L \tag{6.90}$$

Where:

- $F_{crown-sat}/b$ is the contact force between the ring and planet per unit length [N/mm];
- $\rho_{crown-sat}$ is the radius of curvature of the pitch point [mm];

Continuing with the explanation of the block diagram in the figure 6.32, from left to right, after the block concerning the equilibrium equations, there are blocks for calculating the radii of curvature and slip velocities, both in the case of sun-planet meshing and planet-ring meshing. The Simulink blocks for these calculations are shown below.

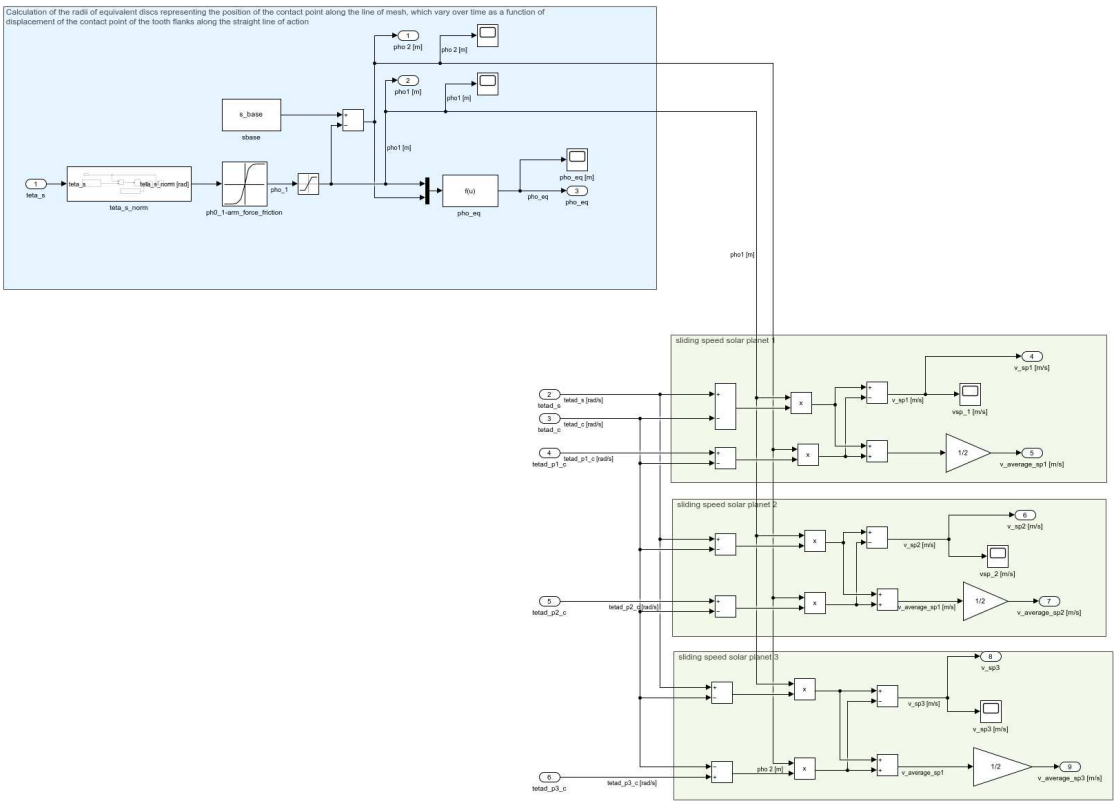


**Figure 6.33:** Simulink- calculation of radii of curvature and relative sliding velocity, solar-planet meshing

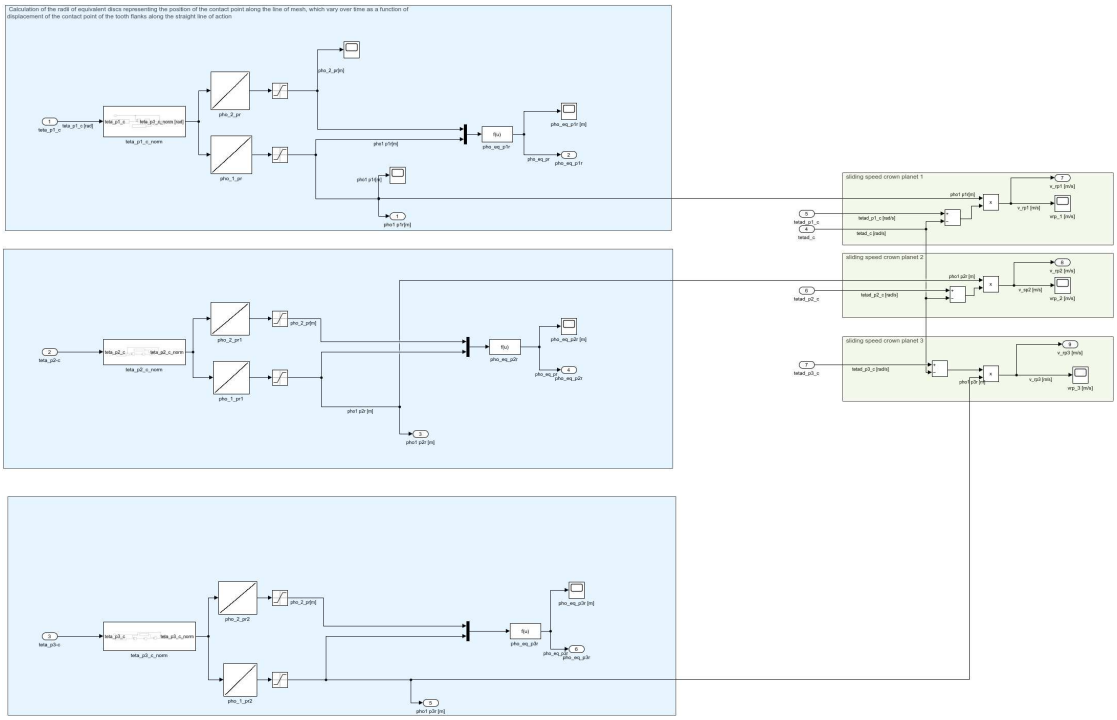

**Figure 6.34:** Simulink- calculation of radii of curvature and relative sliding velocity, crown-planet meshing

As shown in the figure 6.33, using the Lookup Table block, the values of the lever arms of the frictional force with respect to the sun and the planets, $\rho_{1,sol}$ and $\rho_{2,sat}$, are obtained at each instant based on the rotation of the sun gear. Figure 6.35 illustrates the $teta_{s,norm}$ block, which is necessary because the variation of the lever arms along the contact segment repeats for each pair of teeth involved in the meshing. The value $ldc_{length,deg}$ represents the rotation of the sun gear corresponding to the total length of the contact segment traveled by the contact point during meshing.

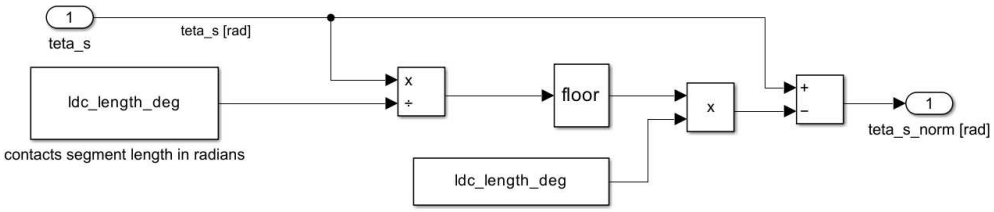


**Figure 6.35:** Simulink block $teta_{s,norm}$

Similarly, a similar construction is employed to estimate the lever arms of the

frictional forces $\rho 1_{sat}$ and $\rho 2_{ring}$, for the ring-planet meshing.

Regarding the characteristics of the sun-planet meshing, the expressions for the radii of curvature of the teeth for both the sun gear and the planet gear are derived, considering the meshing between external gears.

$$\rho_{1,sol} = \overline{T_1 P} = \frac{d_{b1}}{2} \cdot tan(\theta_{pos}) \tag{6.91}$$

$$\rho_{2,sat} = \overline{T_2 P} = s_{base} - \rho_{1,sol} \tag{6.92}$$

where:

- P is the contact point between the tooth flanks;
- the segment from T1 to T2 is referred to as the base pitch segment ($s_{base}$) and is equal to:

$$s_{base} = \frac{d_{b1} + d_{b2}}{2} \cdot tan(\alpha) \tag{6.93}$$

- $d_{b1}$ and $d_{b2}$ are the base diameters of the driving wheel (sun gear) and the driven wheel (planet gear) [m];
- $\theta_{pos}$ represents the generic position of the contact point along the contact segment.

It is the angle between the starting position ($\theta_{pos-A}$) and the ending position ($\theta_{pos-B}$) of the meshing between a pair of engaged teeth.

$$\theta_{pos-A} = arctan\left(\frac{\frac{d_{b1}}{2} \cdot tan(\alpha) - s_{acc}}{\frac{d_{b1}}{2}}\right) \tag{6.94}$$

$$\theta_{pos-B} = arctan\left(\frac{\frac{d_{b1}}{2} \cdot tan(\alpha) + s_{rec}}{\frac{d_{b1}}{2}}\right) \tag{6.95}$$

The contact segment ($s_{cont}$), which represents the portion of the line of action where actual meshing between the teeth occurs, is divided into two parts. The first part is called the approach segment ($s_{acc}$), and the second part is known as the recess segment ($s_{rec}$).

$$s_{acc} = \sqrt{\left(\frac{d_{a2}}{2}\right)^2 - \left(\frac{d_{b2}}{2}\right)^2} - \frac{d_{p2}}{2} sin(\alpha) \tag{6.96}$$

$$s_{rec} = \sqrt{\left(\frac{d_{a1}}{2}\right)^2 - \left(\frac{d_{b1}}{2}\right)^2} - \frac{d_{p1}}{2} sin(\alpha) \tag{6.97}$$

where:

- $d_{b1}$ $d_{b2}$ are the base diameters of the driving wheel (sun gear) and the driven wheel (planet gear) [m];
- $d_{p1}$ $d_{p2}$ are the pitch diameters of the driving wheel (sun gear) and the driven wheel (planet gear) [m];
- $d_{a1}$ $d_{a2}$ are the addendum diameters of the driving wheel (sun gear) and the driven wheel (planet gear) [m];
- $\alpha$ is the operating pressure angle, set at 20 °.

Similarly, the study of the gear geometry is conducted for the ring-planet meshing, where the planet gear consists of an external toothed wheel and the ring gear comprises an internal toothed wheel. In this case as well, tooth contact occurs along the tangent line to the two base circles, and the contact segment lies on this line, delimited by the intersection of the head circles of the two gears with the tangent line.

The diagrams 6.33 and 6.34 also include the calculation of the slip velocity. It is the relative velocity of the common contact point between the teeth in a transverse plane. It consists of the vector difference between the tangential components of the tooth flank velocities at the contact point.

The sun-planet and ring-planet meshings occur simultaneously in the epicyclic mechanism. Since the planets rotate both around their own centers and around the axis of the sun gear, which is solidly connected to the carrier, the slip velocities, $v_{sp}$ (sun-planet) and $v_{pr}$ (ring-planet), can be expressed as:

$$v_{sp} = (\omega_{sol} - \omega_{car}) \cdot_{1-sol} -(\omega_{sat} - \omega_{car}) \cdot_{2-sat} \tag{6.98}$$

$$v_{pr} = (\omega_{sat} - \omega_{car}) \cdot_{1-sat} \tag{6.99}$$

where:

- $_{1-sol}$ $_{2-sat}$ are the radii of curvature of the sun gear and the planet gear, respectively, for the sun-planet meshing [m];
- $_{1-sat}$ $_{2-ring}$ are the radii of curvature of the planet gear and the ring gear, respectively, for the ring-planet meshing [m];
- $w_{car}$ is the rotational speed of the carrier [rad/s];
- $w_{sol}$ is the rotational speed of the sun gear [rad/s];
- $w_{sat}$ is the rotational speed of the i-th planet gear [rad/s].

Continuing with the description of the diagram 6.32, we move on to the calculation of frictional dissipation actions.

The underlying mechanisms of friction related to the presence of lubricant are due to both the viscous effect of the film and the possible direct interactions between the surface asperities of the tooth flanks. The total frictional force is therefore expressed as the sum of these two components.

$$f_{friction} = F_{boundary} + F_{viscous} \tag{6.100}$$

where:

- $F_{boundary}$ is the frictional force due to asperity interactions [N];
- $F_{viscous}$ is the frictional force due to the viscous effect of the lubricant [N].

The Greenwood and Tripp method is employed to determine the contribution due to the interaction between surface asperities, assuming a Gaussian distribution of asperity heights. A small fraction of the load is supported by the contacting surfaces [39].

The load supported by the contacting asperities is defined as Wa, and the contact area between the surfaces is defined as the contact patch area.

$$W_a = \frac{16 \cdot \sqrt{2}}{15} \cdot \pi \cdot (\zeta \cdot \beta \cdot \sigma)^2 \cdot \sqrt{\frac{\sigma}{\beta}} \cdot E' \cdot A_{app} \cdot F_{\frac{5}{2}}(\lambda) \tag{6.101}$$

$$A_a = \pi^2 \cdot (\zeta \cdot \beta \cdot \sigma)^2 \cdot A_{app} \cdot F_2(\lambda) \tag{6.102}$$

Where:

- $(\zeta \cdot \beta \cdot \sigma)$ is the roughness parameter equal to 0.03;
- $\frac{\sigma}{\beta}$ is the average asperity slope equal to $10^-4$;
- E' is the effective modulus of elasticity [Pa];
- $A_{app}$ is the apparent contact area [$m^2$].

The polynomial functions $F_{\frac{5}{2}}(\lambda)$ $F_2(\lambda)$ represent the Gaussian distribution of asperity heights and are expressed as follows:

$$F_{\frac{5}{2}}(\lambda) = \begin{cases} -0.004 \cdot^5 + 0.057 \cdot \lambda^4 - 0.296 \cdot \lambda^3 + 0.784 \cdot \lambda^2 - 1.078 \cdot \lambda + 0.617 & \lambda \leq 3 \\ 0 \qquad \lambda > 3 \end{cases} \tag{6.103}$$

$$F_{\frac{5}{2}}(\lambda) = \begin{cases} -0.002 \cdot \lambda^5 + 0.028 \cdot \lambda^4 - 0.173 \cdot \lambda^3 + 0.526 \cdot \lambda^2 - 0.804 \cdot \lambda + 0.500 & \lambda \leq 3 \\ 0 \qquad \lambda > 3 \end{cases} \tag{6.104}$$

With $\gamma$ as the Stribeck parameter, defined as the ratio of the lubricant film thickness h to the equivalent surface roughness $\sigma$.

The importance of the parameter, the minimum film thickness $h_0 = h_{min}$, is determined by comparing it with the surface roughness. This allows us to determine whether a given gear pair operates under elastohydrodynamic lubrication, direct surface contact, or a mixed regime. Defining the average roughness of the meshing as the average of the roughness of the meshing gears, given by $R_{am} = \frac{1}{2} \cdot (R_{a1} + R_{a2})$, the following cases can occur:

- if $h_0 < 0.7R_{am}$ the surfaces come into direct contact, posing a risk of surface damage;
- if $h_0 \simeq R_{am}$ Ram, a partial elastohydrodynamic lubrication regime is established;
- if $h_0 > 2R_{am}$ elastohydrodynamic lubrication occurs without direct surface contact.

The relationships for determining the minimum film thickness model the gear meshing contact by considering two cylindrical surfaces that, like other parameters, vary during the meshing process.

$$h_{min} = R' \cdot 1.714 \cdot (W'^{(} - 0.128) \cdot U^{(}0.694) \cdot G^{(}0.568)) \tag{6.105}$$

With:

- $W' = \frac{W}{b \cdot R' \cdot E_{eq}}$ as the dimensionless load term;
- $U = \frac{u \cdot \eta_0}{R' \cdot E_{eq}}$ as the dimensionless velocity parameter;
- $G = \alpha \cdot_{eq}$ as the dimensionless term related to material properties.

Where:

- W is the normal load on the surfaces at the contact point [N];
- $R' = \frac{1}{1} + \frac{1}{2}$ is the radius of curvature at the contact point [m];
- $\eta_0$ is the dynamic viscosity of the lubricant at ambient temperature [Pa*s];
- $E_{eq} = \frac{E}{1-v^2}$ is the equivalent modulus of elasticity [Pa];
- u is the average velocity at the contact point [m/s];

- $\alpha$ is the compressibility viscosity coefficient $[m^2/N]$.

Once the lubricant film thickness is calculated, the limiting shear stress of the lubricant $\tau_L$ is defined as follows:

$$\tau_L = \tau_{OL} + \epsilon \cdot P_m \tag{6.106}$$

With:

- $\tau_{OL}$ Eyring-shear stress [Mpa];
- $\epsilon$ as the shear coefficient induced by contact pressure, equal to 0.047;
- $P_m = \frac{W_a}{A_a}$ as the average pressure at the summit of the asperities [MPa].

Finally, the boundary force $F_{boundary}$ is obtained as follows:

$$F_{boundary} = \tau_L \cdot A_a \tag{6.107}$$

At this point, the viscous action $F_{viscous}$ is estimated using the following formula (Evans and Johnson):

$$F_{viscous} = F_{flank} \cdot \left( 0.87 \cdot \alpha \cdot \tau_0 + 1.74 \cdot \frac{\tau_0}{\overline{p}} \cdot ln \left( \frac{1.2}{\tau_0 \cdot h_{c0}} \cdot \left( \frac{2 \cdot \dot{K} \cdot \eta_0}{1 + 9.6 \cdot \zeta} \right)^{\frac{1}{2}} \right) \right) \tag{6.108}$$

$$\zeta = \frac{4}{\pi} \cdot \frac{\dot{K}}{\frac{h_{c0}}{R}} \cdot \left( \frac{\overline{p}}{E' \cdot R \cdot K' \cdot \rho' \cdot c' \cdot V} \right)^{\frac{1}{2}} \tag{6.109}$$

Where:

- $\dot{K}$ is the thermal conductivity of the lubricant [W/mK];
- K' is the thermal conductivity of the solid surfaces [W/mK];
- $\rho'$ is the density of the solid surfaces $[kg/m^3]$;
- c' is the specific heat capacity of the solid surfaces [kJ/kg];
- $h_{c0}$ is the thickness of the lubricant film [m];
- R is the radius of curvature of the surfaces [m];
- $\overline{p}$ is the average contact pressure [Pa];
- $F_{flank}$ is the average contact pressure [Pa].

The above equations show that the frictional actions vary along the contact segment due to changes in slip velocity, contact geometry, and lubricant thickness. The contact force exchanged between the tooth surfaces is obtained at each simulation step.

Figures 6.36 and 6.37 illustrate the Simulink model for estimating Fboundary and Fviscous for both the sun-planet and ring-planet meshing.

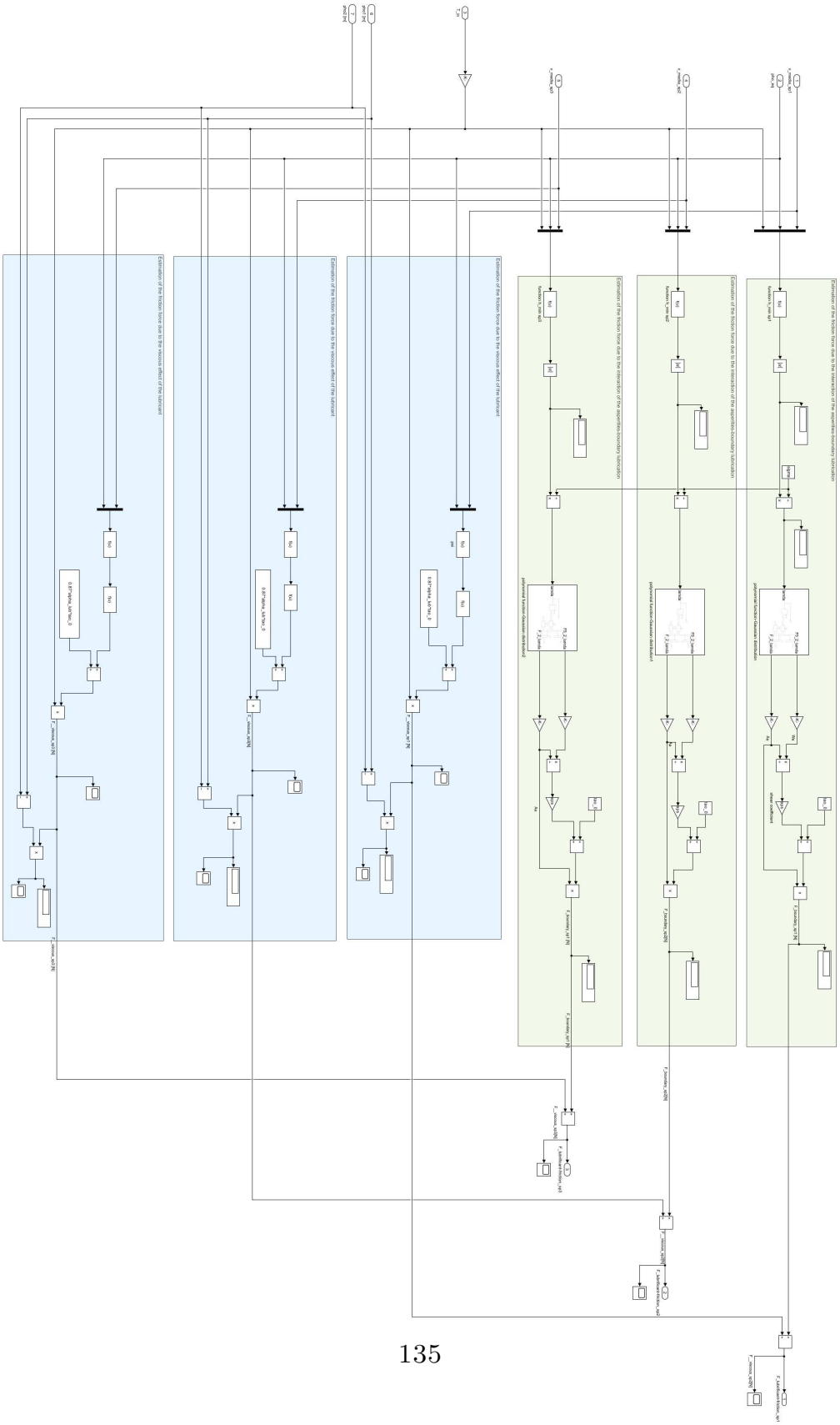



**Figure 6.36:** Simulink- Frictional dissipation actions - Sun-planet meshing.

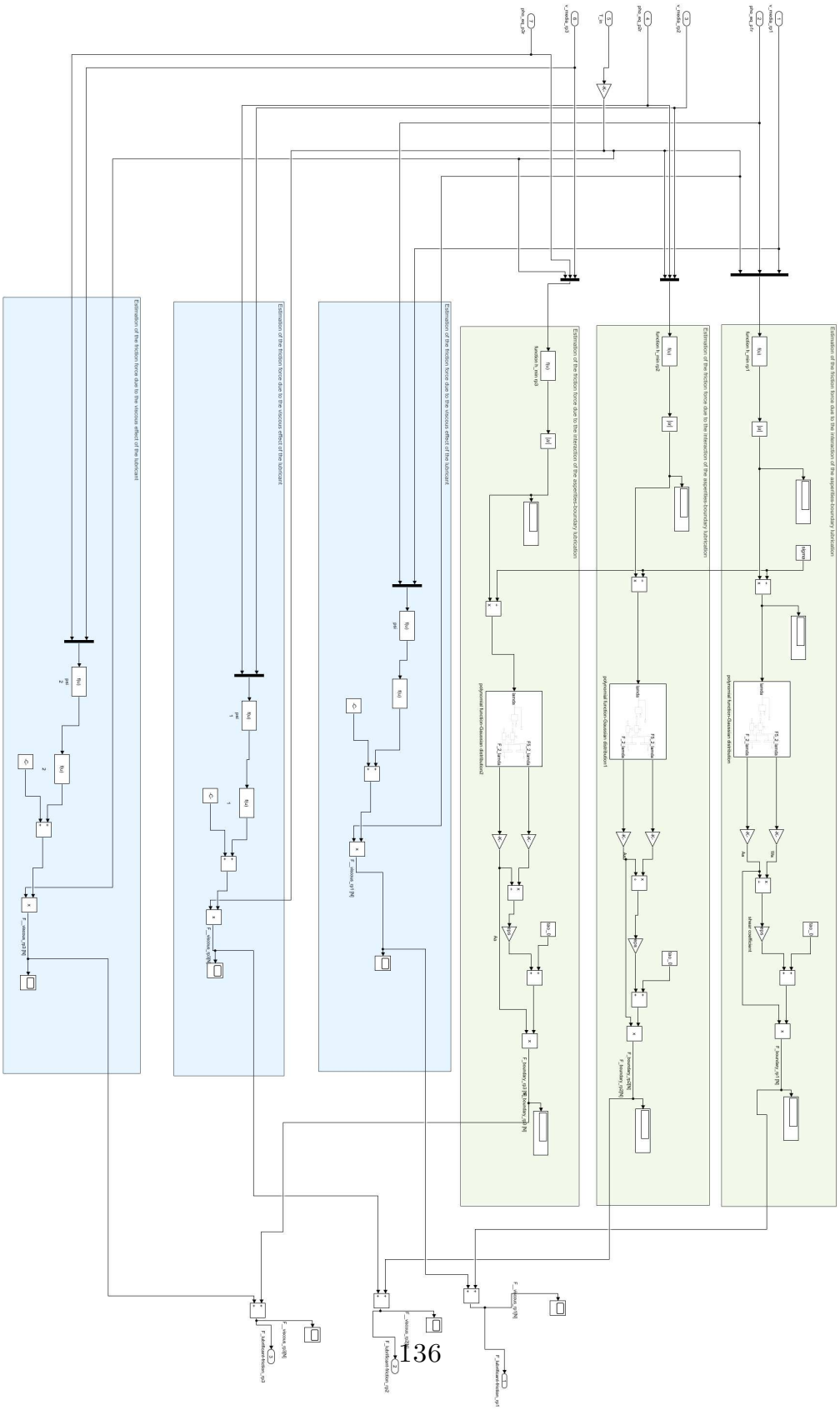



**Figure 6.37:** Simulink- Frictional dissipation actions - crown-planet meshing

Regarding power losses independent of the load, ventilation losses have been considered. These losses are due to two phenomena:

- Ventilation losses related to the viscous dissipation of the fluid in which the gears operate.
- Losses due to micro-collisions during the initial stages of meshing.

These phenomena generate a torque opposing the motion, which can be approximated by a quadratic relationship with an experimental coefficient $c_s$.

$$T_{vent} = c_s \cdot \dot{\theta}^2 \tag{6.110}$$

$$c_s = k_s \cdot d_{sol}^2 + \left(\frac{z_{sol}}{z_{sat}}\right)^3 \cdot k_s \cdot d_{sat}^2 \tag{6.111}$$

Where $k_s$ is the temperature-dependent velocity loss parameter, which at T=20 [°C] takes values between $2 \cdot 10^{-}10 and 5 \cdot 10^{-}10 N m s^2/mm^2 rad^2$.

Finally, in Figure 6.39 and Figure 6.38, the Simulink models for calculating the power losses independent of the load and the losses related to the discussed frictional torques are presented.

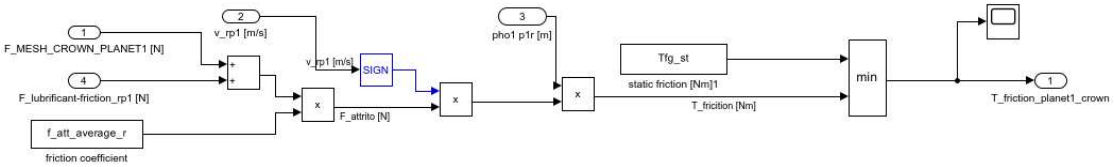


**Figure 6.38:** Simulink block calculation of crown-planet 1 gear losses .

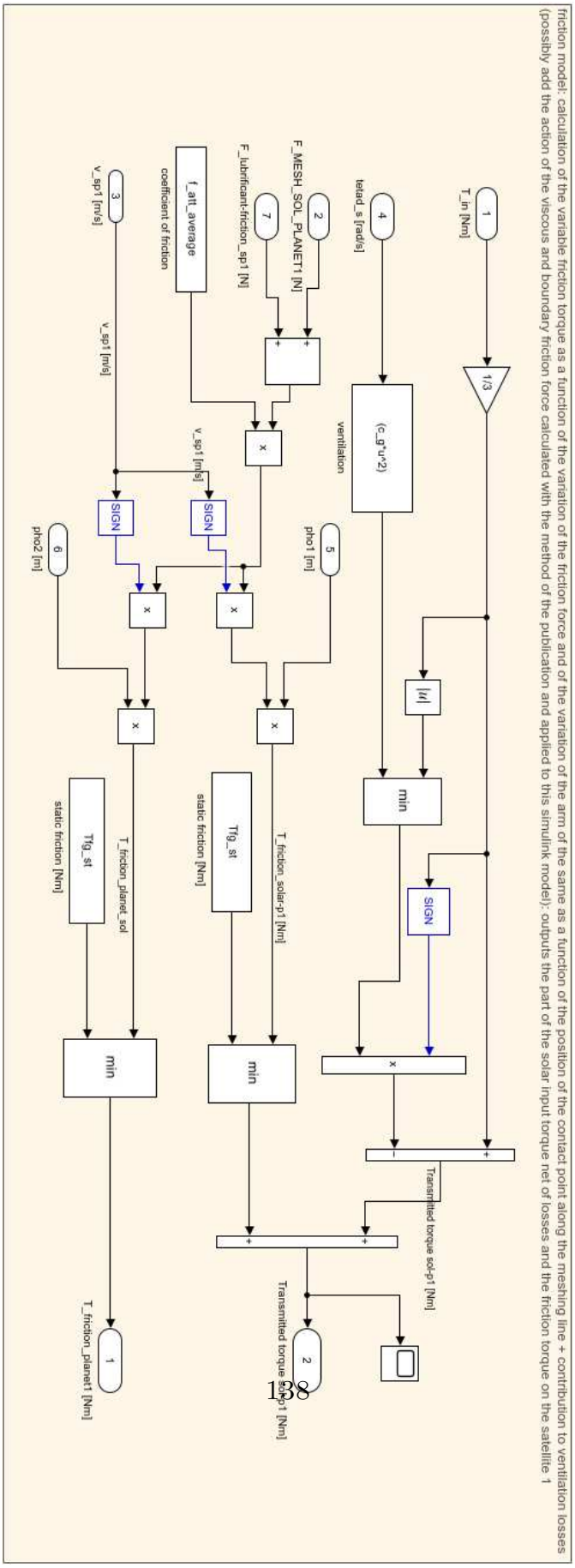


**Figure 6.39:** Simulink block calculation of solar-planet 1 gear losses .

## SCREW MECHANISM

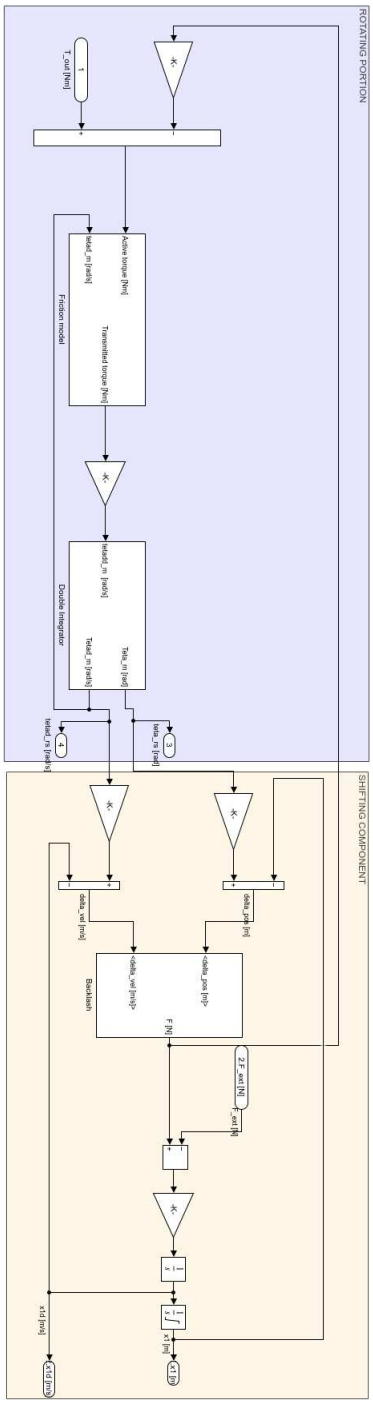


**Figure 6.40:** Simulink model of screw actuator.

The model of the satellite roller screw transmission is shown in the figure 6.21. It receives as inputs the torque output from the gearbox and an external force resulting from the interaction between the actuator and the flight control surface. It outputs the linear displacement and linear velocity of the screw, as well as the rotation and angular velocity of the nut. This system can be divided into a rotational part (modeling of the nut) and a shifting part (modeling of the screw).

As a first step, the net torque acting on the system $T_{active}$ is calculated, which is the difference between the electromagnetic torque coming from the electric motor and transmitted by the reducer, and the load given by the force acting on the rod of the EMA multiplied by the transmission ratio from rotary to linear motion of the screw. Then, the friction component ($T_{passive}$) is subtracted from this value, resulting in the transmitted torque.

$$T_{active} = T_{out} - F \cdot \frac{p}{2\pi} \tag{6.112}$$

$$T_{transmitted} = T_{active} - T_{passive} \tag{6.113}$$

In Equation 6.112, p represents the pitch of the screw, and F is determined by the backlash block with input parameters:

$$\Delta x = x_{nut} - x_{screw} \tag{6.114}$$

$$\Delta \dot{x} = \dot{x}_{nut} - \dot{x}_{screw} \tag{6.115}$$

Where:

- $x_{mv} = \theta_{mv} \frac{p}{2\pi}$ Linear displacement of the nut;
- $x_v$ Screw displacement;
- $\dot{x}_{mv} = \dot{\theta}_{mv} \cdot \frac{p}{2\pi}$ Linear velocity of the nut;
- $\dot{x}_v$ Screw velocity;

To complete the description of the modeling of the rotating part, once the transmitted torque is calculated, it is divided by the inertia of the nut added to that of the motor shaft ($J_{rs} + J_m$), thus obtaining the angular acceleration of the nut. Integrating once gives the angular velocity, and integrating a second time gives the rotation.

When it comes to modeling the screw, it follows the following relationship:

$$F - F_{ext} = m\ddot{x}_1 \tag{6.116}$$

Where:

- F is the force calculated by the backlash block;

- $F_{ext}$ is derived from the interaction between the screw and the control surface;
- m is the mass of the screw;

Similarly to what was done for the nut, integrating the acceleration gives the velocity, and integrating again gives the linear displacement of the actuator.

The following will delve into the modeling of backlash and the modeling of friction.

**MODELING OF BACKLASH**

Backlash is a phenomenon present in coupled mechanical systems. Mechanical clearance results in errors in kinematic transmission, force/torque losses, reduced transmission efficiency, and control difficulties. When considering two coupled components, backlash can be defined as the maximum displacement that one of the components can make before contacting and dynamically connecting with the other when it is stationary. The transmission of torque in the presence of backlash is modeled through an equivalent "spring-damper" system, where the equivalent stiffness coefficient of contact and equivalent damping coefficient of contact model the actions (forces or moments) involved. The relative position helps determine whether contact is occurring or not, and together with the relative velocity at the interface, it determines the actions exerted by the interaction of the two components based on the specific case.

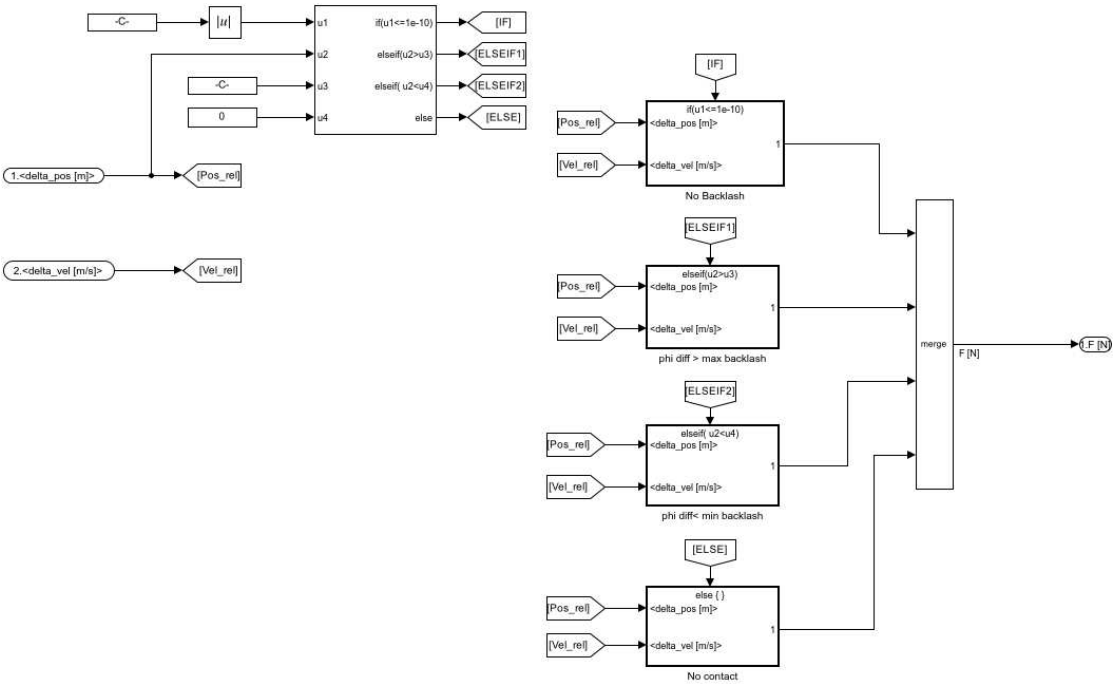


**Figure 6.41:** Simulink block BACKLASH.

Four cases are distinguished based on the relative position between the considered components:

- No backlash: There is no mechanical clearance between the two coupled components. The coupling is approximated by a "spring-damper" model for torque transmission.
- phi diff $>$ max backlash: There is mechanical clearance, and the internal element in the coupling is in contact on the positive side of the displacement direction. The equivalent spring-damper system transmits torque when compressed in the contact direction.
- phi diff $<$ min backlash: There is mechanical clearance, and the internal element in the coupling is in contact on the negative side of the displacement direction. The equivalent spring-damper system transmits torque when compressed in the contact direction.
- No contact: The elements are decoupled, meaning their positions are covered by the backlash, and there is no contact, resulting in no torque transmission.

**MODELING OF FRICTION**

For modeling the friction between the nut and the screw, the Karnopp friction model is implemented. The mathematical model of Karnopp is as follows:

$$T_{friction} = \begin{cases} -min(T_{static}, T_{applied}) & if(|\omega| < a) \\ -T_{dynamic} \cdot sign(\omega) & else \end{cases} \tag{6.117}$$

The basis of the Karnopp model is the choice of a velocity interval centered at the origin. A deadband is introduced within which the mechanical system is considered to be in static friction condition, providing a more realistic modeling of the phenomenon. One difficulty in applying the Karnopp model lies in selecting the velocity deadband. For simplicity, in our case, a value of "a" equal to 0.0001 has been chosen. The following figure presents the Simulink block of the implemented Karnopp model.

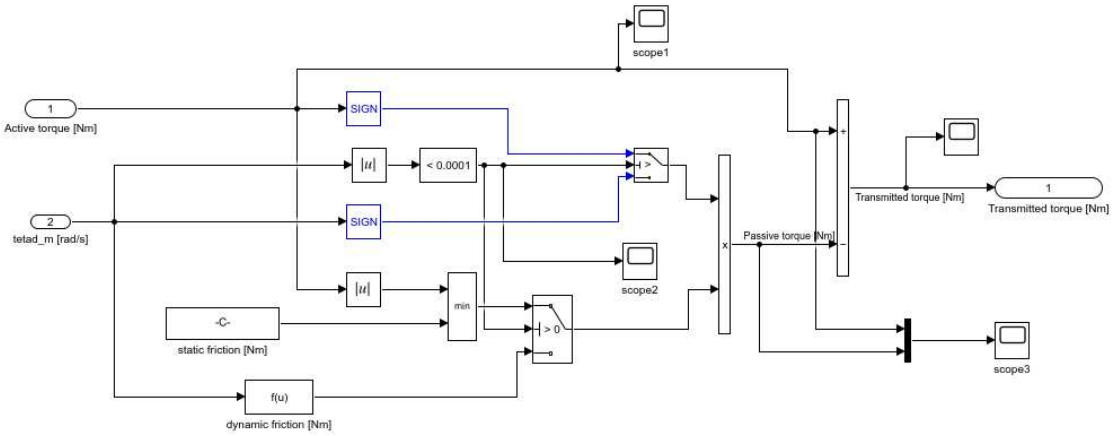


**Figure 6.42:** Simulink block- friction model

## 6.1.4 Control surface

Returning to the diagram in the figure 6.1, which illustrates the complete modeling of the system considering the two parallel actuators, we now move on to describing the final part that pertains to the flight control surface.

There are two backlash blocks that model the contact between the surface and the two actuators. By summing the two forces calculated using these blocks, we obtain the force applied to the surface. This surface is modeled as a system with

mass and stiffness, and it follows the following formula [5]:

$$m\ddot{x} + k_{flap}x = F \tag{6.118}$$

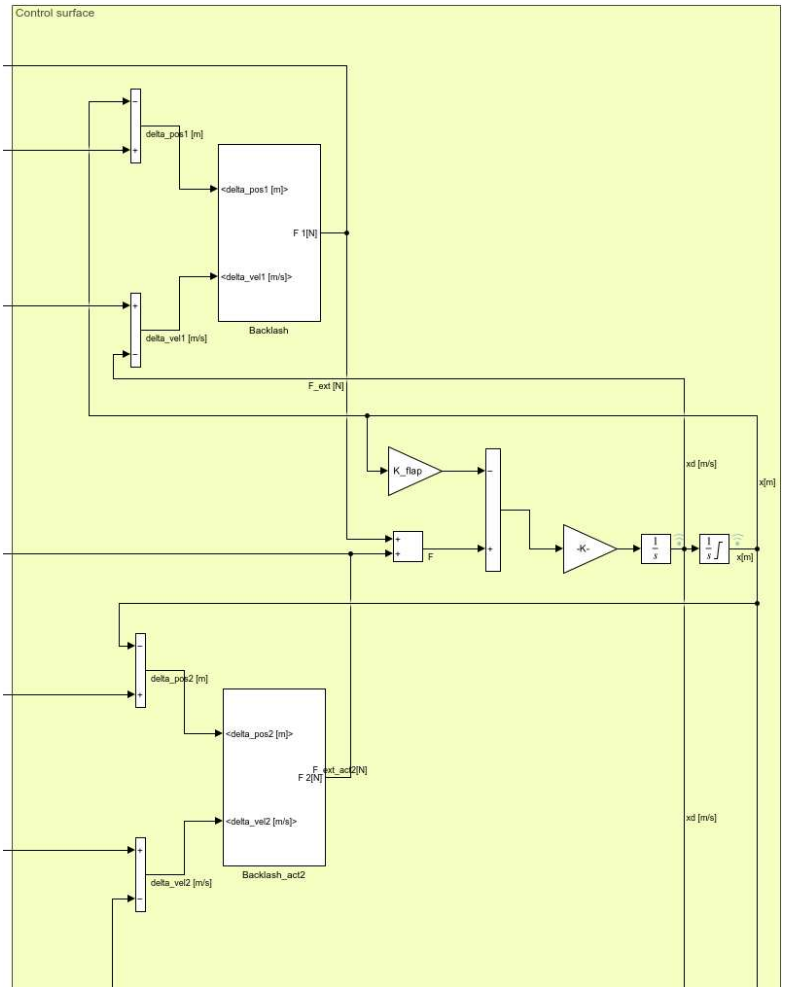


**Figure 6.43:** Simulink-control surface.

[5]The presence of an external load on the surface will also be taken into account later.

### 6.1.5 Temperature influence

Temperature plays a significant role in the performance of various components. As discussed in Chapter 4, studying the system's behavior at different temperatures revealed how they affect various aspects, particularly in friction calculations. The variation of various coefficients with temperature depends on various factors associated with the detailed design of the actuator and the type of lubricant used. The Simulink model for estimating corrective factors as a function of temperature is presented below:

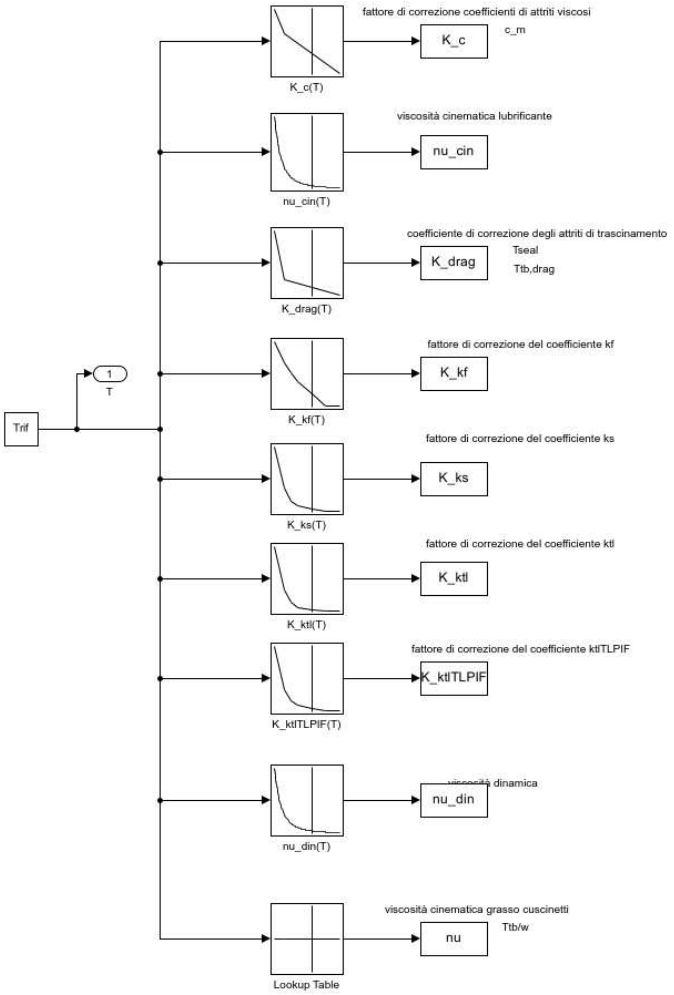


**Figure 6.44:** Simulink-Calculation of temperature-dependent parameters

## 6.2 Time response to a step command

After completing the entire model, it was determined that initiating a simulation campaign would be necessary to assess its actual performance. This evaluation can be conducted in both the time and frequency domains. Specifically, requirements in the time domain typically pertain to the step response and encompass parameters such as settling time, steady-state error, and overshoot. Conversely, in the frequency domain, the evaluation is based on Bode diagrams and encompasses steady-state error, bandwidth, stiffness, and stability.

Initially, the system's response to a step command was examined. This response not only provides crucial insights into the system's temporal behavior but also facilitates the calibration of controller constants following the Ziegler-Nichols method. This approach entails initially setting the integral and proportional gains to zero. Then, the proportional gain is gradually increased from zero until reaching the ultimate gain, at which the control loop output exhibits stable and consistent oscillations. The ultimate gain and oscillation period are subsequently utilized to establish the proportional and integral gains of the PI controller, employing formulas outlined in the literature. However, in practical scenarios, it is common to increase the proportional gain until an overshoot is achieved while keeping the integral gain at zero. Subsequently, the integral gain is increased until the error is brought back to a steady state, aligning with the desired dynamics. In this way, new control parameter values were found, which are reported in the following table.

| Controller parameters | |
|---|---|
| $Kp_{id}$ | 5000 [V/A] |
| $Ki_{id}$ | 1000 [Vrad/s] |
| $Kp_{iq}$ | 5000 [V/A] |
| $Ki_{iq}$ | 1000 [Vrad/s] |
| $Kp_w$ | 40 [As/rad] |
| $Ki_w$ | 15 [A] |
| $Kp_p$ | 4000 [rad/ms] |
| $Ki_p$ | 25 $[rad^2/ms^2]$ |

**Table 6.2:** Summary table of controller parameters

Subsequent simulations were performed using various step command amplitudes. This is because, in a non-linear system, the response is significantly affected by the amplitude of the applied command. Specifically, amplitudes corresponding to 10 % and 70% of the maximum actuator stroke were considered. Following that, tests were conducted under different conditions: without any load and with a resisting load. These tests were carried out while maintaining an ambient temperature of 20°C.

The most significant plots for each test are displayed below.

For the initial analysis, the system's response to a position command with an amplitude of 10 % of the actuator stroke was examined, in the absence of aerodynamic load.

To elaborate further, the actuator was initially positioned at the center, and after 0.1 seconds, a positive position command of 0.058 meters was issued.

Consequently, a position error arises in the system due to this reference signal. Once compensated for by the position loop PI controller, it becomes the reference angular velocity for the inner velocity loop. This, in turn, leads to a velocity error, which is then compensated for, and serves as the reference current for the innermost current loop.

As a result, currents are generated in the three motor phases ($i_a, i_b, i_c$), and their interaction with the magnetic field of the fixed magnets within the rotor determines the torque exerted between the stator and rotor.

Figure 6.45 illustrates the behavior of the reference velocity $xd_{ref}$ compared to the actual velocity xd achieved by the system. Immediately after receiving the step command for position, the system generates a significant velocity command $xd_{ref}$. Initially, it reaches a peak value that surpasses the maximum attained velocity reference and subsequently starts to decrease until it reverses its direction at time t = 0.49s, reaching a negative peak of much smaller magnitude compared to the previous one. The change in sign is attributed to the overshoot of the position signal, as visible in Figure 6.47. Subsequently, from time t = 4.87s onwards, the system exhibits a velocity command that oscillates around zero. However, its value is not exactly zero due to a small steady-state error in the position loop. On the other hand, the actual velocity of the system, despite attempting to track the velocity command, fails to reach its peak condition due to the physical limits of the system and the delay in the system's response to the given command.

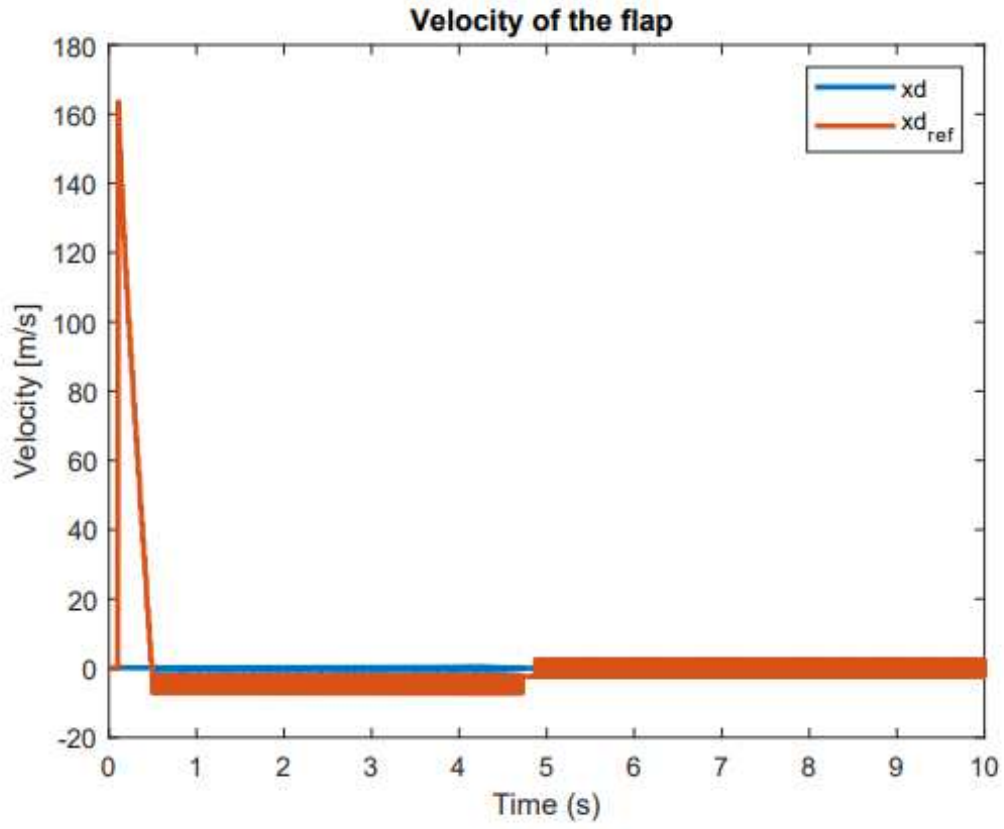


**Figure 6.45:** Plot of the reference speed and the actual speed of the flap (test with 10 command and no external load)

The discrepancy between the velocities results in an error that, once corrected, leads to the emergence of the reference current signal $i_{ref}$, as depicted in Figure 6.46. It is immediately apparent that the trend of this quantity is very similar to that of the reference angular velocity.

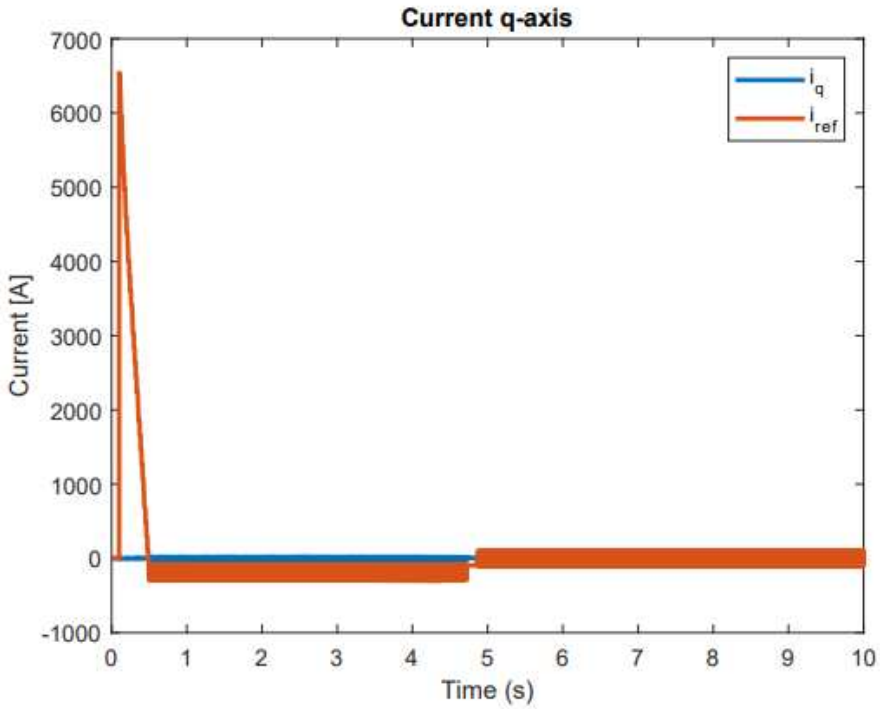


**Figure 6.46:** Plot of the reference current and the current on the quadrature axis (test with 10 % command and no external load).

Subsequently, the reference current was juxtaposed with the quadrature axis current $i_q$, taking into account a rotating axes (d, q) model of the motor at the current controller level. However, this current component fails to attain the peaks observed in the reference current due to both the saturation effects on the three-phase currents of the electric motor and the interference caused by the direct-axis current $i_d$. The currents $i_d$ and $i_q$, which are referenced to a rotor-aligned coordinate system, correspond to the currents $i_a$, $i_b$, $i_c$ of the three motor phases through the inverse Park transform. The current is converted into mechanical energy, which is utilized to move the control surface.

The figure 6.47 illustrates what happens to the position. The system is quite responsive and tracks the provided position command effectively, with a settling time [6] of 0.48s for a 5 % threshold. Specifically, it exhibits a slight overshoot of 5.1 % before stabilizing and oscillating around the reference value. At steady state,

[6]The system's settling time is characterized as the duration subsequent to the initiation of a step input, during which the system takes to attain and sustain a level that deviates by a specified margin from the ultimate value. Typically, a value of 5 % is commonly referenced.

there may be a very small static error of 6  10-4 observed between the two.

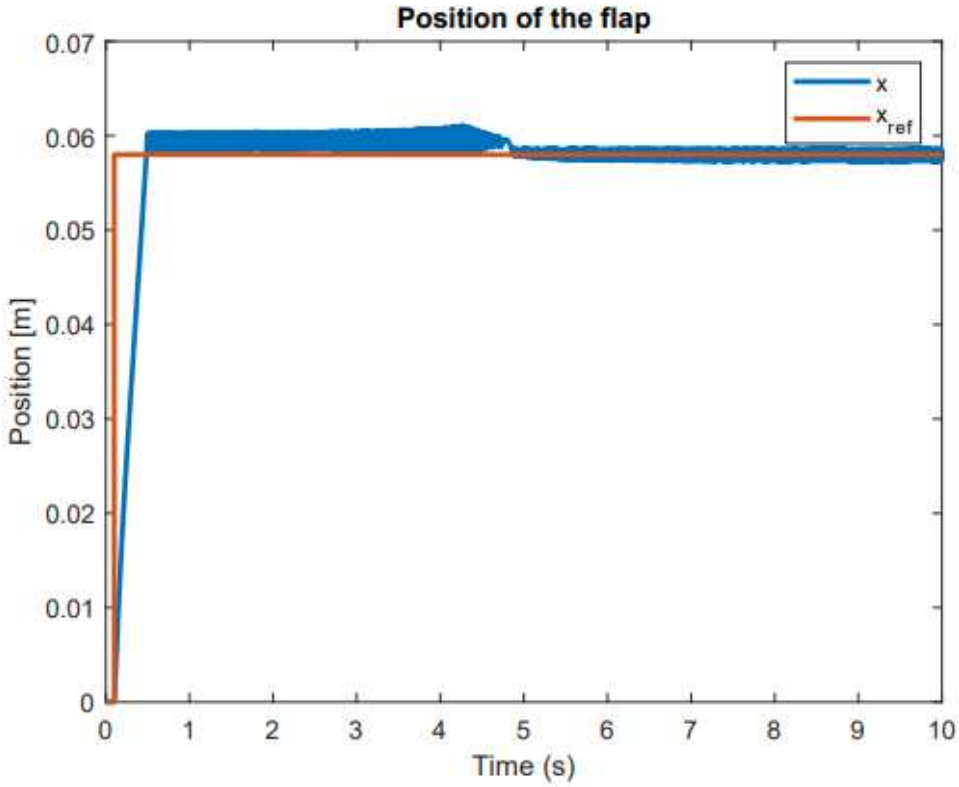


**Figure 6.47:** Plot of the position commanded by the pilot and the position actually reached by the actuator (test with 10 % command and no external load)

Regarding the tests conducted without load but with higher values, Figure 6.48 presents the position graph obtained with a command equal to 70 % of the actuator stroke. The first observation that can be made is that as the provided position command increases, the overshoot gradually shifts to the right, indicating longer settling times. In the case of a command with an amplitude equal to 70 % of the stroke, the maximum settling time is indeed 4.8s. Additionally, it is notable that a steady-state error of 0.014 remains.

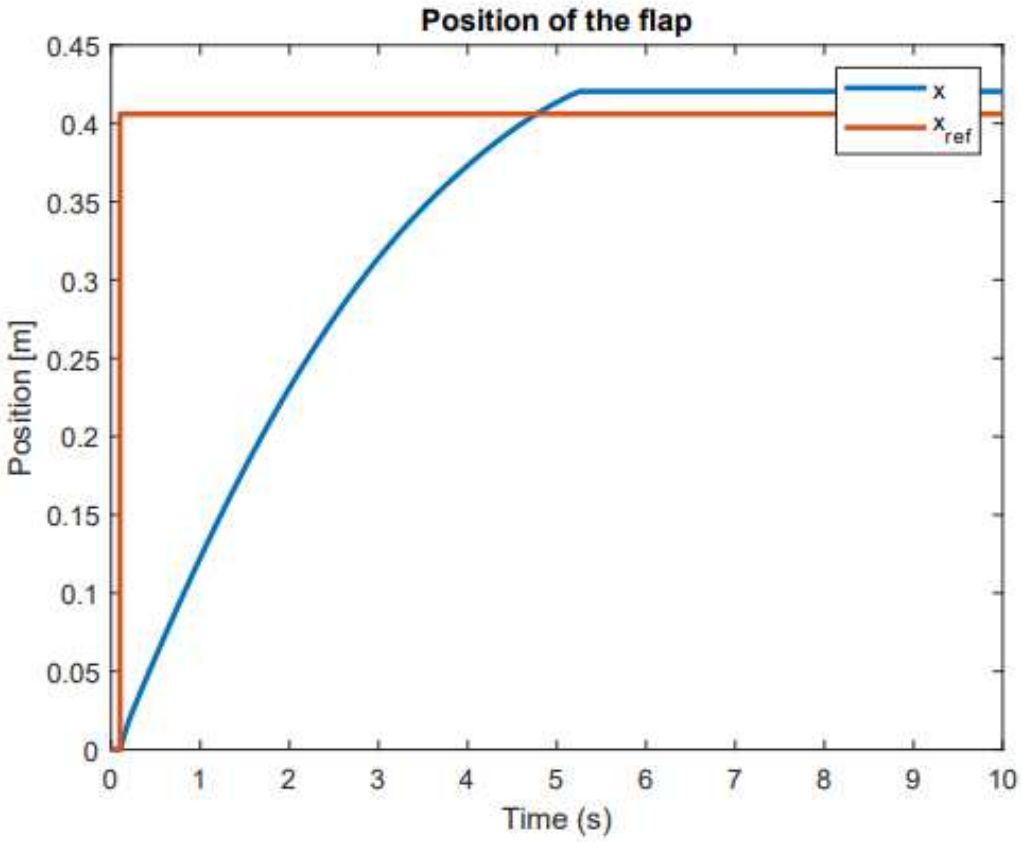


**Figure 6.48:** Plot of the position commanded by the pilot and the position actually reached by the actuator (test with 70 % command and no external load).

Tests were subsequently conducted in the presence of aerodynamic resisting loads, equal in magnitude to the nominal load (5066 N), and at various position control amplitudes.

Only the case of the resisting nominal load with a positive position command amplitude of 10 % of the available stroke is shown in more detail below. Comments have been added primarily related to the external load, such as comments on the system's behavior with a step position command, which have already been extensively examined earlier. The aerodynamic load acting on the control surface, in this case, experiences an upward rotation after 0.1s due to the actuator rod extending by 10 % of the actuator stroke. This load is equal to the nominal load and occurs after 0.2s, as depicted in Figure 6.49. This specific time instance has been chosen to clearly observe how the system responds to an external disturbance after receiving the position command.

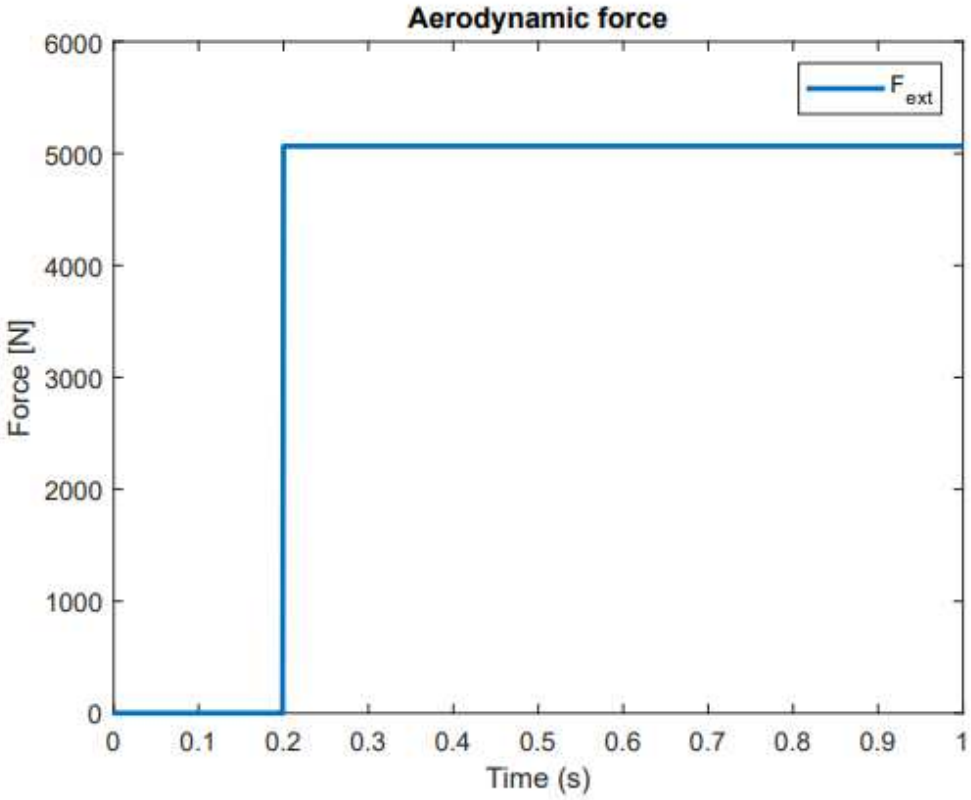


**Figure 6.49:** Plot of the resistant aerodynamic load.

Figure 6.50 illustrates the actual position achieved by the flap in relation to the position command given by the pilot. In this case, between the system surpassing and converging towards the commanded value, the system is disrupted by the external aerodynamic load, which causes increased oscillations.

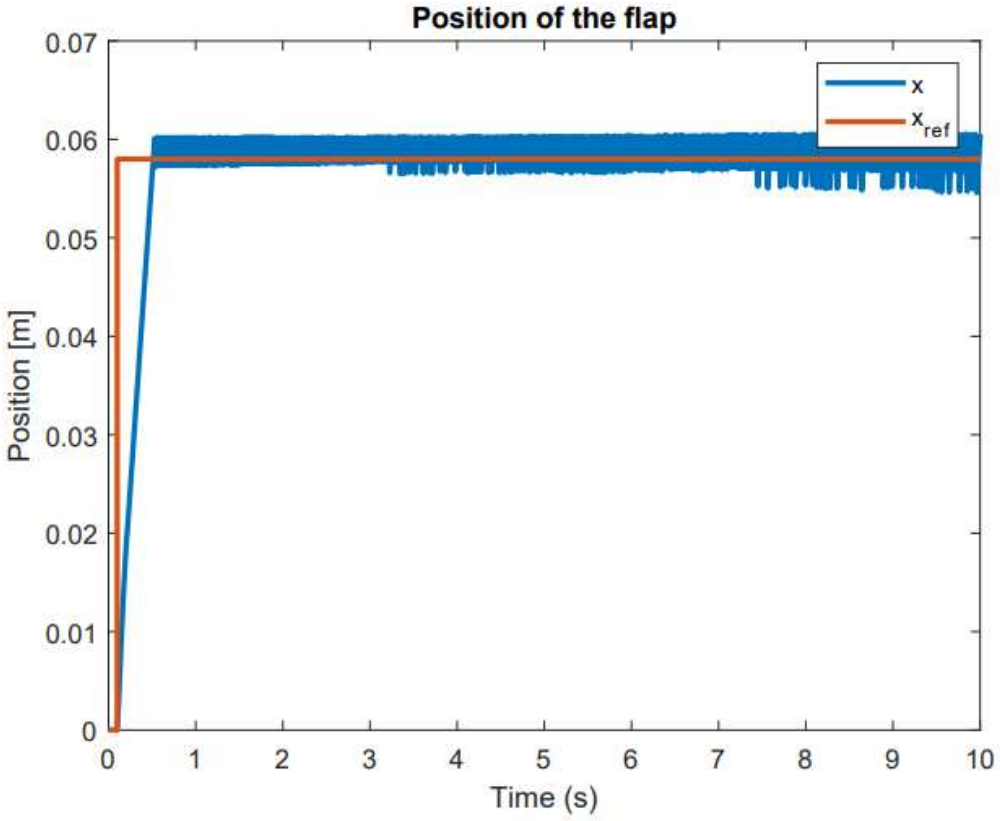


**Figure 6.50:** Plot of the position commanded by the pilot and the position actually reached by the flap (test with 10 % command and resistant aerodynamic load) .

## 6.3 Frequency response

Following the time response analysis, the frequency response was evaluated using Bode plots. However, due to the system's strong non-linearity and the intention to avoid linearization, Simulink application couldn't be employed to generate these plots. Consequently, a Matlab script presented in Appendix A was utilized to deduce the frequency trends retrospectively based on simulated data.

Subsequently, both closed-loop and open-loop frequency responses are presented to assess the system's stability and meet its requirements. Stability is the primary operational specification, and once it is ensured, there is a need to achieve minimum performance criteria to ensure satisfactory system performance.

Nevertheless, it is crucial to note that, even in the case of a non-linear system, the frequency response exhibits varying characteristics depending on the amplitude of the input control. Therefore, it was determined that the analysis of different loops would be conducted with a command equivalent to 10% of the maximum magnitude under examination.

Starting with the innermost loop, namely the current loop, its frequency response was investigated. Specifically, Figure 6.51 illustrates the magnitude and phase curves for the closed- loop, while Figure 6.52 exhibits the magnitude and phase curves for the open-loop configuration.

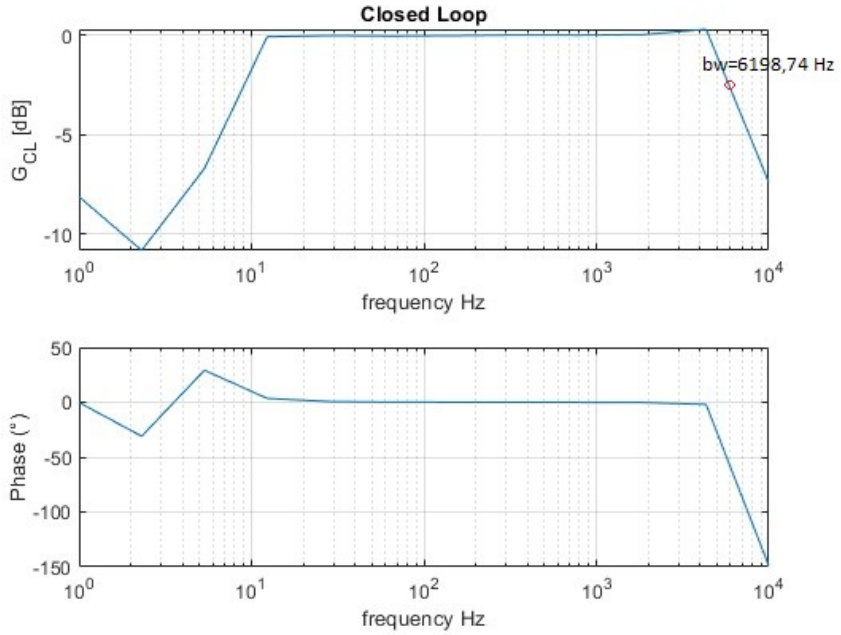


**Figure 6.51:** Frequency response of closed loop current obtained from Simulink model simulation

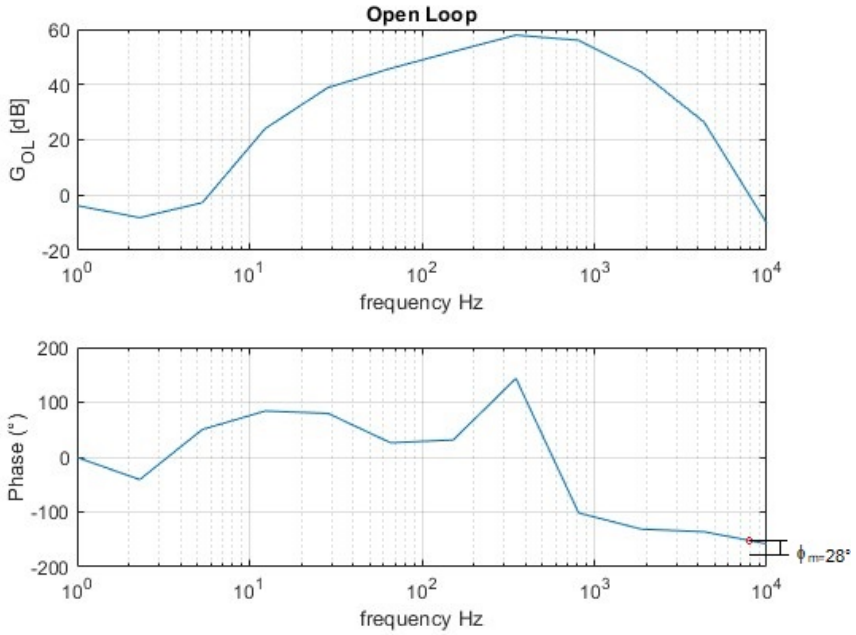


**Figure 6.52:** Frequency response of open loop current obtained from Simulink model simulation

Looking at the closed-loop graphs, it is possible to observe the behavior of this inner loop. Regarding the closed-loop magnitude, it can be noted that the attenuation of this quantity is approximately zero from a frequency of 12.32 Hz up to about 100 Hz. Beyond this value, a more pronounced attenuation occurs, reaching -15 dB at 4328.76 Hz. Specifically, the system's amplitude is -3 dB at a frequency of 6198.74 Hz, which represents the system's bandwidth. As for the phase, it can be seen that there is an approximately zero phase shift from 28 Hz to 4328.76 Hz, and a phase shift of about -148° at 104 Hz. Above 4 103 Hz, both the magnitude and the phase shift are more pronounced, but for practical purposes, these high frequencies are of little relevance. By using the open-loop graphs, on the other hand, it is possible to observe the system's stability. In particular, the system has a phase margin $\phi_m$ of 28 at a frequency of 7920 Hz, as well as a gain margin Gm that in this case will not be infinite as in the case of the linearized model but will certainly be greater than the instability limits. In fact, since the phase reaches -180° at very high frequencies, the module in that area will surely have high attenuation and this will ensure large gain margins. For these reasons, it was not considered important to simulate the model for further higher frequencies.

After obtaining satisfactory results in the current loop, we moved on to the immediately outer control loop, namely the speed loop. Once again, as shown in Figure 115 and Figure 116, the closed-loop and open-loop configurations of the

considered system were studied, respectively.

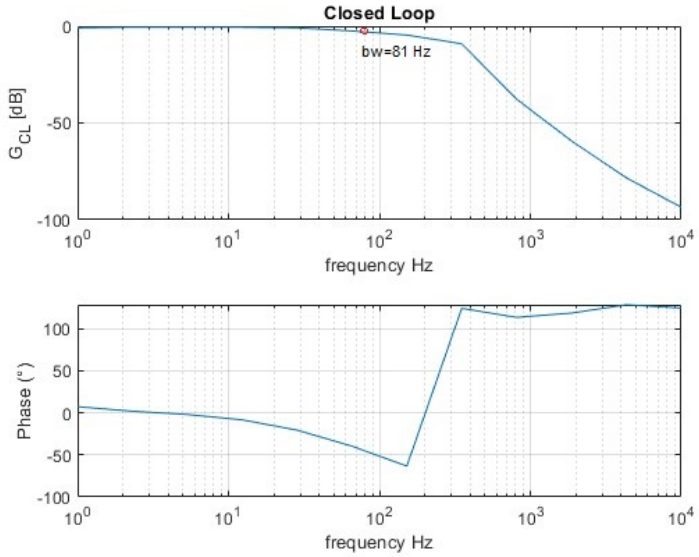


**Figure 6.53:** Frequency response of closed loop velocity obtained from Simulink model simulation

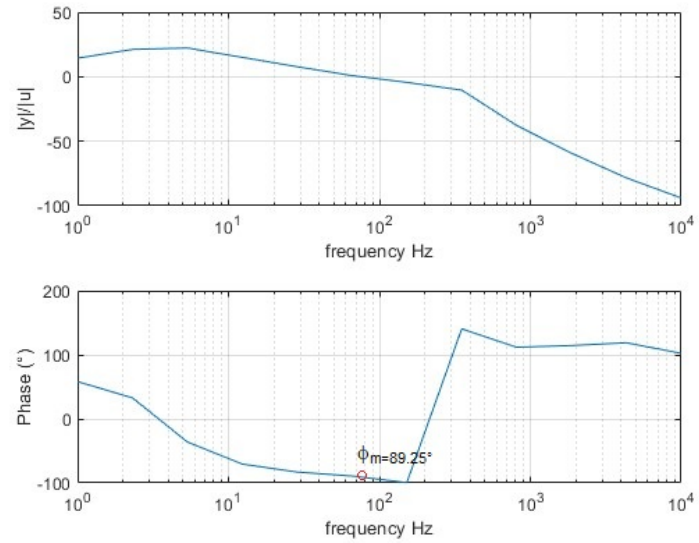


**Figure 6.54:** Frequency response of open loop velocity obtained from Simulink model simulation

In this case, the magnitude plot of Gcl shows that the output of this loop is

identical to the input up to approximately 11 Hz. After this value, the magnitude starts to decrease, reaching a value of -3 dB at 81 Hz, which represents the bandwidth of this second analyzed loop. However, even at higher frequencies considered for this loop, the magnitude attenuation does not exceed 20 dB, which is an acceptable result.

Similarly, the phase of the closed loop presents results in line with expectations, as it does not exceed 100° of phase shift up to 351 Hz, a frequency beyond the range of interest for this loop.

From the open-loop Bode diagrams, it was also possible to verify the stability of this second loop. In fact, in this case, the magnitude assumes a null value around 75 Hz, and at this frequency, a phase margin $\phi_m$ of 89.25° is obtained. The gain margin Gm is infinite, or at least the phase reaches -180° at high frequencies that are not relevant to the case under consideration. These values are well beyond the stability margins normally assumed by the scientific community and reported in Chapter 5. Such high stability margins at very low angular speeds (10 % of the maximum value) are positive because, as mentioned earlier, instability can occur at low speeds and not at high speeds.

Ultimately, the examination of the position loop's frequency response awaits. Given that this loop serves as the outermost layer, it also exhibits the slowest characteristics. Following a similar approach employed for the two innermost loops, the subsequent diagrams present the Bode plots for both open-loop and closed-loop analysis. These plots are based on a sinusoidal input command with an amplitude equal to 10 % of the available actuator stroke.

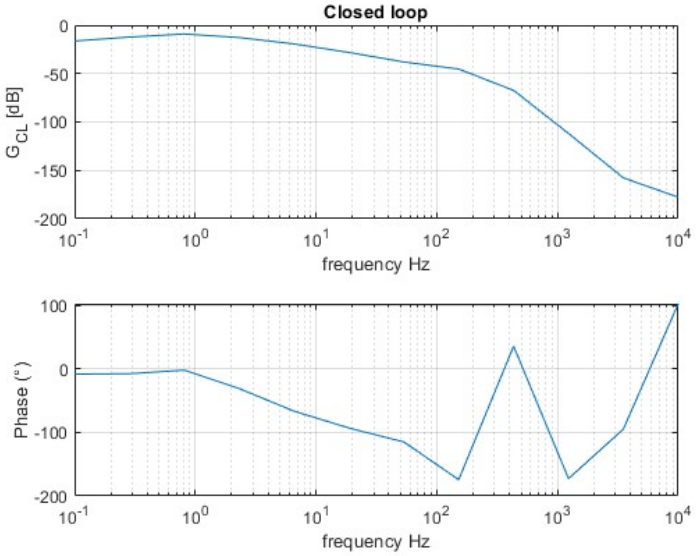


**Figure 6.55:** Frequency response of closed loop position obtained from Simulink model simulation

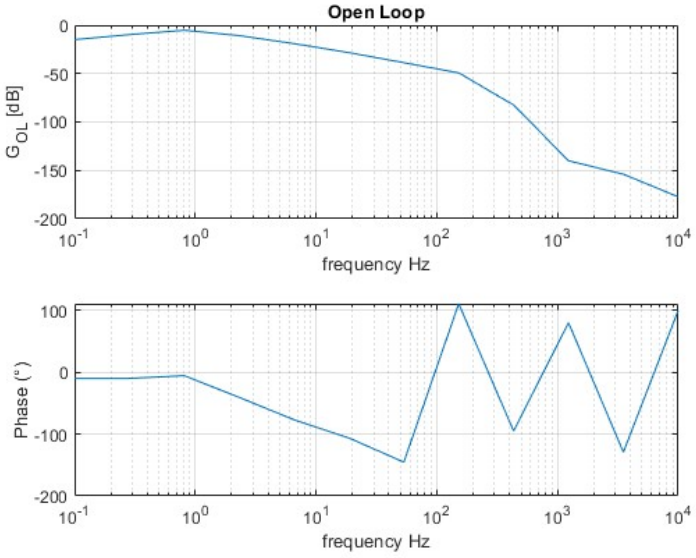


**Figure 6.56:** Frequency response of open loop position obtained from Simulink model simulation

# Chapter 7

# Conclusion

The objective of this thesis is the design and study of a control system for an electromechanical actuator for secondary flight control; specifically, in this case, it is a Fowler flap. However, this sizing technique can be extended to any secondary flight control surface.

First, the architecture to be used was outlined, which in this case involved two identical electromechanical actuators operating in parallel to enhance reliability and fault tolerance. Moving forward, all the necessary sizing steps were defined, and all the components were identified. Once the sizing process is completed, the masses and volumes of the various components were calculated. Using this preliminary model, the system's behavior was studied under varying temperatures, specifically conducting a verification at low temperatures (-54°C), considering only one operational actuator. As to be expected, it was found that the worst-case scenario occurred when only one actuator was operating at low temperatures. It was ensured that the chosen motor was capable of delivering the required power in all cases. Additionally, the stop and start conditions were studied.

After these calculations, the linearized system was modeled to evaluate its dynamic characteristics and obtain an initial estimate of the necessary control parameters. Specifically, by writing the linearized equations that characterize the system's physics, constructing a block diagram, and deriving the transfer functions of the three considered control loops, it was possible to represent the Bode diagrams and study the frequency response. Following a careful calibration of the controller parameters, the results obtained from this analysis, presented in Chapter 5, were satisfactory as they ensured both stability margins and compliance with the typically required position control and flight command requirements. By analyzing the open-loop Bode diagrams, it was feasible to assess the stability characteristics of the different system loops.

A more in-depth study of the system could involve conducting tests using a more comprehensive model of the palnetary gearbox. Possible future developments could

focus on improving the system's performance, aiming to enhance the reliability of the electromechanical actuator and prevent or at least predict the phenomenon of jamming. This would enable its widespread utilization in primary flight control systems as well.

# Chapter 8

# Acknowledgements

I would like to express my sincere appreciation to all the individuals who have provided unwavering support throughout this extraordinary journey.

I am deeply grateful to my advisor, Prof. Massimo Sorli, for granting me the opportunity and instilling confidence in my abilities. I extend my heartfelt thanks to my co-advisor, Dr. Andrea De Martin, for his exceptional patience and willingness to address my myriad of inquiries. Their support has been crucial in successfully concluding my academic journey.

I also want to extend my gratitude to my tutor, Rocco Gentile, who has guided me during my invaluable internship experience at Leonardo Labs. His guidance, warm reception, and advice have played a vital role in my professional growth.

Furthermore, I want to convey my deep appreciation to my dear friends and beloved family. Without their unwavering support and love, I would not have been able to reach this significant milestone. Their encouragement and understanding have been my pillars of strength.

# Appendix A

# Appendix A

The Matlab script for acquiring the frequency response in closed and open loop is presented hereinafter. It comprises a primary script (startsim.m) that invokes the $rf\_ana.m$ function, which in turn invokes the FreqResp.m function to compute the magnitude and phase in both frequency responses.

```
%%%%%%%%%%%%%%%%%%%%
%startsim.m
%%%%%%%%%%%%%%%%%%%%
%clear all
ampl=0.058;%0.0058;%1.352; %amplitude
bias=0;% average generator value
itime=3;%integration time
frmin=1;%frequency min, Hz
frmax=20;%10^4;%frequency max Hz
npunti=12;% number of frequencies analyzed equally spaced on the logarithmic axis
grat=0;
graf=1;

nomemod='EMA.slx';

 % % Current
 % nomesig.OL_in = "i_e";
 % nomesig.OL_out = "i_q";
 % nomesig.CL_in = "i_ref";
 % nomesig.CL_out = "i_q";

% % Speed
% nomesig.OL_in = "e_speed";
% nomesig.OL_out = "F/b speed";
% nomesig.CL_in = "xd_ref";
% nomesig.CL_out = "xd [m/s]";

%Position
nomesig.OL_in = "e_pos";
nomesig.OL_out = "F/b pos";
nomesig.CL_in = "x_ref";
nomesig.CL_out = "x[m]";

[OL,CL,w]=rf_ana([ampl bias itime frmin frmax npunti grat graf], nomesig,nomemod,1,1e-5);
```

```
function [OL,CL,vett_w]=rf_ana(Par,nomesig,nomemod,skip_time,FixedStepSize)

%definition of analysis parameters
%================================
%n° of points into which the interval is divided
npunti=Par(6);
%amplitude of excitation
vett_Ampi=Par(1)*ones(npunti,1);
%average excitation value
bias=Par(2);
%frequency range analysed
wmin=Par(4)*2*pi; %minimal pulsation [rad/s]
wmax=Par(5)*2*pi; %maximum pulsation [rad/s]
vett_w=logspace(log10(wmin),log10(wmax),npunti)';
%simulation duration
itime=Par(3);
%variables that activate the graphics
grat=Par(7); %graphs over time
graf=Par(8); %frequency graphs
%model variable parameter: optional not activated
%if a parametric analysis was needed, it would be necessary to activate one
%second input port from which to enter the parameter value for each simulation
vett_C=[1];

%frequency response calculation for an assigned parameter value
%=============================================================================
nparam=max(size(vett_C));
for j=1:nparam,
C=vett_C(j);

  %calculation of the amplitude of the answer in freq. for each freq.
  %_____________________________________________________________

  for i=1:npunti
            w=vett_w(i); %rad/s
         Ampi=vett_Ampi(i);

         %instants of start and end of simulation
         periodo=2*pi/w;

            ncicli=6;

            if ncicli*periodo <= itime
             ncicli=ceil(itime/periodo);
            end

            disp(['n_cicli = ',num2str(ncicli)])

            Tstart=0;
            Tfinal=periodo*ncicli;
            TIMESPAN=[Tstart Tfinal];
```

```
        %Sinusoidal input to the model
        %each cycle is divided into 100 time intervals
        TT=Tstart:periodo/100:Tfinal;
        U=Ampi*sin(w*TT)+bias;
        UT=[TT',U'];

             %definition of simulation options
       %       RelTol=1e-3;
       %       AbsTol=1e-6;
       %     MaxStep=periodo/20;
       %       InitialStep=MaxStep/10;
       %
 options=simset('RelTol',RelTol,'AbsTol',AbsTol,'MaxStep',MaxStep,'InitialStep',InitialSte
 options=simset('FixedStep',FixedStepSize);
 %try
 Simout=sim(nomemod,TIMESPAN,options,UT);
 clc
 disp(['Step = ',num2str(j)])
 index_skip = round(skip_time./FixedStepSize);
 length(Simout.logsout.get(nomesig.OL_in).Values.Time(index_skip:end))
 T =
 Simout.logsout.get(nomesig.OL_in).Values.Time(index_skip:end);%(round(index_in(1)./2):end
 OLV(:,1) = Simout.logsout.get(nomesig.OL_in).Values.Data(index_skip:end)-
mean(Simout.logsout.get(nomesig.OL_in).Values.Data(index_skip:end));
 OLV(:,2) = Simout.logsout.get(nomesig.OL_out).Values.Data(index_skip:end)-
bias;
 [OLAmp(i,j),OLFas(i,j),OLFasin(i,j),OLFasout(i,j)] = FreqResp(OLV,w,T,Tfinal-
skip_time);
 %save(['OLV_',num2str(j),'-',num2str(i),'.mat'],'OLV')
 clear OLV
 if max(size(nomesig.CL_in))>0
 CLV(:,1) =Simout.logsout.get(nomesig.CL_in).Values.Data(index_skip:end)-bias;
 CLV(:,2) = Simout.logsout.get(nomesig.CL_out).Values.Data(index_skip:end)-
bias;
 [CLAmp(i,j),CLFas(i,j),~,~] = FreqResp(CLV,w,T,Tfinal-skip_time);
 %save(['CLV_',num2str(j),'_',num2str(i),'.mat'],'CLV')
 clear CLV
 end
 %catch
 %disp('Simulation aborted')
 %end
 end
end

OL.Amp = OLAmp;
OL.Fas = OLFas;
OL.Fasin = OLFasin;
OL.Fasout = OLFasout;

if max(size(nomesig.CL_in))>0
    CL.Amp = CLAmp;
    CL.Fas = CLFas;
    figure("Name",'Closed Loop')
    subplot(2,1,1)
```

```
    semilogx(vett_w/(2*pi),20*log10(CL.Amp)),grid
    xlabel('frequency Hz')
    ylabel('|y|/|u|')
    subplot(2,1,2)
    semilogx(vett_w/(2*pi),CL.Fas*180/pi),grid
    xlabel('frequency Hz')
    ylabel('Phase (°)')
else
    CL.Amp = [];
    CL.Fas = [];
end

%display of numerical values
%frequency response graphs

% if graf==1
figure("Name",'Open Loop')
subplot(2,1,1)
semilogx(vett_w/(2*pi),20*log10(OL.Amp)),grid
xlabel('frequency Hz')
ylabel('|y|/|u|')
subplot(2,1,2)
semilogx(vett_w/(2*pi),OL.Fas*180/pi),grid
xlabel('frequency Hz')
ylabel('Phase (°)')
```

*Published with MATLAB® R2023a*

3

```
function [Amp,Fas,Fasin,Fasout] = FreqResp(Y,w,T,Tfinal)
  Reout=2/Tfinal*trapz(T,sin(w*T).*Y(:,2));
  Imout=2/Tfinal*trapz(T,cos(w*T).*Y(:,2));
  Ampout=sqrt(Reout^2+Imout^2);
  Fasout=atan2(Imout,Reout);
  Rein=2/Tfinal*trapz(T,sin(w*T).*Y(:,1));
  Imin=2/Tfinal*trapz(T,cos(w*T).*Y(:,1));
  Ampin=sqrt(Rein^2+Imin^2);
  Fasin=atan2(Imin,Rein);
  Amp=Ampout/Ampin;
  Fas=Fasout-Fasin;
end
```

*Published with MATLAB® R2023a*

# Appendix B

# Appendix B

The Matlab code that contains all the data for the model is as follows:

```
%% System data
clear all; close all; clc

%% Properties of the gearbox lubricant
pho_lub=0.869;         % [kg/dm3] density of the lubricant at the reference temperature
alpha_lub=1.67*1e-8;   % [m^2/N] compressive viscosity coefficient
nu_din_rif=0.144;      % [Pa*s] dynamic viscosity of the lubricant at the reference temperature
eps=0.047;             % pressure-induced shear coefficient
tao_0=0.2*10^6;        % [Pa] eyring shear stress
K_lub=2000;            % [W/mK] lubricant conductivity
K_steel=50;            % [W/mK] conductivity
c_steel=0.012;         % specific heat
c1=-1.890758;
c2=10.5253;
psi=-0.001;                                  % density-temperature coefficient
T=-54:40;                                    % temperature range
nu_cin=10.^(10.^(c1.*log(T+273)+c2));        % kinematic viscosity  f(T)
pho2_T=pho_lub.*(exp(psi.*(T-15)));
nu_din=(nu_cin./10^6).*(pho2_T*1000);

%****************************** TEMPERATURE DEPENDENCIES ******************************
%% Temperature dependent parameters
Trif = input('Reference temperature [°C] = ');
if Trif < -54
    disp('Minimum temperature: -54°C');
    Trif = -54;
else if Trif > 40
        disp('Maximum temperature: 40°C');
        Trif = 40;
    end
end

 sim T_influence
 nu = nu(end);
 nu_cin = nu_cin(end);
 nu_din = nu_din(end);
 K_drag = K_drag(end);
 K_kf = K_kf(end);
 K_ks = K_ks(end);
 K_ktl = K_ktl(end);
 K_ktlTLPIF = K_ktlTLPIF(end);
 K_c = K_c(end);
 nu_din_vec=[0.1368 0.0217 0.0060 0.0035 0.0024];

%************************ AERODYNAMIC SURFACE PARAMETERS ****************************

%%% dynamic parameters
meq_flap_RH_WT=50;                      % [kg] flap equivalent translating mass
K_flap=1e5;                             % [N/m] flap stiffness
F_ext_flap=0;%5066;                        % [N] aerodynamic load

%%% kynematic parameters
xlim_p_RH_WT = 0.580;                    % [m] actuator max stroke +
xlim_n_RH_WT = 0;                        % [m] actuator max stroke -
kynematics_RH_WT = @(x)(1600-sqrt(1600^2-4*1064.93*x))/2/1064.93;
xmap_RH_WT = linspace(xlim_n_RH_WT,xlim_p_RH_WT,1000);
thetamap_RH_WT = kynematics_RH_WT(xmap_RH_WT);

%%% backlash data
xbl_flap_RH_WT = 0;                % [m] flap initial backlash (da 0.01 a 0.1)
K_shaft_flap_RH_WT = 5e6;                 % [N/m] equivalent contact stiffness
C_shaft_flap_RH_WT = 1e5;          % [Ns/rad] equivalent contact damping factor

%*************************** POWERSCREWS PARAMETERS *********************************
%% Screw

%%% Meaningful geometrical quantities
prs_RH_WT = 0.03;                                       % [m] screw step
anglim_p_RH_WT = xlim_p_RH_WT *2*pi/prs_RH_WT;          % [rad] screw angular stroke +
anglim_n_RH_WT = xlim_n_RH_WT *2*pi/prs_RH_WT;          % [rad] screw angular stroke -

%% Friction data
% Reference temperature T = 40°C
T_seal_0 = 0.030;               % [Nm] seals drag torque
Ttb_seal = 0.0038;          % [Nm] thrust bearing seals drag torque
Ttb_drag_0 = 1.49*10^-7;    % [Nm] thrust bearing drag torque
```

```
Ttb_sl= 0.0171;             %[Nm] thrust bearing sliding frictional moment
ktb_ftag=9.97e-1;           % reduction factor for heating from shear phenomena
ktb_rs=9.96e-1;             %filling/deficiency kinematic correction factor
Grr = 0.001249/1000;        % speed loss parameter
espf = 0.6;             % SKF exponent

Tfrs_sl_RH_WT = (Ttb_drag_0+T_seal_0+Ttb_seal);
Tfrs_st_RH_WT = K_drag*(T_seal_0+Ttb_drag_0+Ttb_seal);

%%% inertia
Jrs_RH_WT = 0.00086;      % [kgm2]    moment of inertia of the screw
mrs_RH_WT = 20.62;        % [kg]      è la massa dell'attuatore??

%%% backlash data
xbl_rs_RH_WT = 0;                       % [m] screw initial backlash (da 0.01 a 0.1)
K_shaft_rs_RH_WT = 7.8e7;               % [N/m] equivalent contact stiffness
C_shaft_rs_RH_WT = 1e4;                 % [Ns/rad] equivalent contact damping factor

%% ************************* GEARBOX PARAMETERS ************************************
tau_tot=18;

%% FIRST STAGE
%%% geometric data of the gear wheels
pho=7850;                       % [kg/m3] density
eps_sp_1st=1.47;                %  conduct report solar-planet ATTENZIONE NEL SUO CASO ERANO UGUALI
eps_rp_1st=1.60;                %  conduct report ring-planet
x_i=0;                          % correction factor
alpha=20*(pi/180);              %[rad] pressure angle
mn = 1/1000;                    %[m] normal module
z_1st = [28 56 140]';           % numeber of teeth solar-planet-ring - 1st stage
d_1st=mn.*z_1st;                %[m] pitch diameters  1st
s_dente=pi*mn/2;                %[m] tooth thickness in the pitch circle
b_1st=20;                       %[mm] band width
m_sol_1st=0.097;                %[kg] solar mass
m_sat_1st=0.387;                %[kg] planet mass

% Wheelbase , base radii and head radii
Int=((d_1st(1) + d_1st(2))/2);      %[m] wheelbase
rbs= 0.01315;                       %[m] base radius solar gear
rbp= 0.0263;                         %[m] base radius planet gear
rbr= 0.0658;                         %[m] base radius ring
rbc=rbs+rbp;                        %[m] "base radius" carrier
rts=(d_1st(1)/2)+mn;                %[m] head radius solar
rtp=(d_1st(2)/2)+mn;                %[m] head radius planet
rtr=(d_1st(3)/2)+0.25*mn;           %[m] head radius ring

% shaft
E_shaft_in=210;                %[Gpa] elasticity module
v=0.3;                         % Poisson coefficient

%%% kinematics
% transmission reports
tau_rp = z_1st(2)/z_1st(3);
tau_sp = -(z_1st(1)/z_1st(2));
tau_1st = 1 + (z_1st(3)/z_1st(1));
% torque distribution-static analysis
T_s= 24;                         % [Nm]
F_sp=T_s./(3*d_1st(1)*cos(alpha));
F_rp=F_sp;
% speed
n_in=2088;                       %[rpm]
omega_in=(2*pi*n_in)/60;         %[rad/s] solar shaft speed
omega_c=omega_in/tau_1st;        %[rad/s] carrier speed
omega_s=omega_in;                %[rad/s] solar speed
omega_p=(omega_s-omega_c)*(z_1st(1)/z_1st(2)); %[rad/s] relative speed planet


%%% dynamic
% Moment of inertia
I_sol=9.47e-6;  %[kg*m2] moment of inertia solar
I_sat=1.52e-4;  %[kg*m2] moment of inertia planet
I_car=1.60e-4;     %[kg*m2] moment of inertia carrier
```

```
%%% mesh stiffness- Kuang_Yang model
% solar-planet
R_sol_inf=sqrt(((Int*sin(alpha)) - sqrt((mn + d_1st(2)/2)^2 -(((d_1st(2)/2)*cos(alpha))^2)))^2 +
((d_1st(1)/2)*cos(alpha))^2); %radial distance from the contact initiation points
A=0;                                % start of the contact segment
B=(eps_sp_1st-1)*2*pi/z_1st(1);
C=2*pi/z_1st(1);
D=eps_sp_1st*2*pi/z_1st(1);

% first stretch (two pairs of teeth in contact)
tetaAB=linspace(A,B);              % mesh angle feed vector from A to B
% second stretch (a pair of teeth in contact)
tetaBC=linspace(B,C);             % mesh angle feed vector from B to C
rBC_1=sqrt((((d_1st(1)/2)*cos(alpha)).^2) + (sqrt((R_sol_inf.^2)-(((d_1st(1)/2)*cos(alpha)).^2)) +
(d_1st(1)/2)*cos(alpha).*tetaBC).^2);
rBC_2=sqrt((((d_1st(2)/2)*cos(alpha)).^2) + ((Int*sin(alpha) - sqrt(rBC_1.^2 -
((d_1st(1)/2)*cos(alpha)).^2))).^2);
[KBC_sol]=mesh_stiffness(mn,z_1st(1),d_1st(1),rBC_1,x_i);
[KBC_sat]=mesh_stiffness(mn,z_1st(2),d_1st(2),rBC_2,x_i);
% third stretch (two pairs of teeth in contact)
tetaCD=linspace(C,D)  ;            % mesh angle feed vector from C to D

% stiffness with a pair of teeth in contact (BC)
Keq_1cop= (b_1st/1000).*((KBC_sol.*KBC_sat)./(KBC_sol + KBC_sat));

% planet-ring
R_sat_inf=sqrt(((Int*sin(alpha)) - sqrt((-mn + (d_1st(3)/2))^2 -(((d_1st(3)/2)+ (1.25*mn))^2))^2 +
((d_1st(2)/2)*cos(alpha))^2));
Apr=0;                                          % start of the contact segment
Bpr=(eps_rp_1st-1)*2*pi/z_1st(2);
Cpr=2*pi/z_1st(2);
Dpr=eps_rp_1st*2*pi/z_1st(2);
% second stretch (a pair of teeth in contact)
tetaBCpr=linspace(Bpr,Cpr) ;                      % mesh angle feed vector from B to C
rBC_1_pr=sqrt((((d_1st(2)/2)*cos(alpha)).^2) + (sqrt((R_sat_inf.^2)-(((d_1st(2)/2)*cos(alpha)).^2)) +
(d_1st(2)/2)*cos(alpha).*tetaBCpr).^2);
rBC_2_pr=sqrt((((d_1st(3)/2)+ (1.25*mn)).^2) + ((Int*sin(alpha) - sqrt(rBC_1_pr.^2 -
((d_1st(2)/2)*cos(alpha)).^2))).^2);
[KBC_sat_pr]=mesh_stiffness(mn,z_1st(2),d_1st(2),rBC_1_pr,x_i);
[KBC_ring_pr]=mesh_stiffness(mn,z_1st(3),d_1st(3),rBC_2_pr,x_i);

% stiffness with a pair of teeth in contact (BC)
Keq_1cop_pr= (b_1st/1000).*((KBC_sat_pr.*KBC_ring_pr)./(KBC_sat_pr + KBC_ring_pr));

% constant stiffness and damping
Keq_1cop_const=mean(Keq_1cop);
Keq_1cop_const_pr=-mean(Keq_1cop_pr);
ksp=(0.75*eps_sp_1st + 0.25)*Keq_1cop_const*(b_1st/1000);
krp=(0.75*eps_rp_1st + 0.25)*Keq_1cop_const_pr*(b_1st/1000);
damp_ratio=(0.03+0.17)/2;

%Varying mesh stiffnesses over time
pb=3;                                       %basic step
psi_n=pb*(2*pi)/(z_1st(1)*z_1st(3));
gammasol_sat=-(z_1st(1)/(2*pi))*psi_n;
gammaring_sat=(z_1st(3)/(2*pi))*psi_n;

% speed loss coefficients
ks0 = 3.5E-10;                  % [Nms2/mm2rad2] speed loss parameter @40°C -10
ks = ks0*K_ks;                  % [Nms2/mm2rad2]speed loss parameter
% cs coefficients computation
cs= ks*(((d_1st(1)*1000))^2+3*(z_1st(1)/z_1st(2))^3*((d_1st(2)*1000))^2);
% tare losses
ktl0 = 0.001;                % [Nm/mm] tare losses coefficient @40°C
TLPIF = 2.15;                 % tare losses increase factor (breakout)
ktl_TLPIF = ktl0*TLPIF*K_ktlTLPIF; % tare losses coefficient breakout
TtlBO = ktl_TLPIF*(((d_1st(1)*1000))+3*(z_1st(1)/z_1st(2))*((d_1st(2)*1000)));
Tfg_st = TtlBO;
c_g = cs;

%%% dati backlash
b_max = 0;
```

```
%%% contact segment SOLAR-PLANET
% length of solar-planet contact segments
s_acc=sqrt((rtp^2)-(rbp^2)) - (d_1st(2)/2)*sin(alpha);
s_rec=sqrt((rts^2)-(rbs^2)) - (d_1st(1)/2)*sin(alpha);
s_base=(rbs+rbp)*tan(alpha);

teta_rif_A=atan((rbs*tan(alpha) - s_acc)/rbs);
teta_rif_B=atan((rbs*tan(alpha) + s_rec)/rbs);
teta_rif=linspace(teta_rif_A,teta_rif_B,300);
ldc_length_deg=teta_rif(end)-teta_rif(1);      % the rotation of the solar corresponding to the total length
of the segment of the path contacts
pho1=rbs.*tan(teta_rif);         % [m] radii of the equivalent circles
pho2=s_base-pho1;
pho_eq=(pho1.*pho2)./(pho1+pho2);
E=E_shaft_in;
E_eq=E/(1-(v^2));
% load splitting along the contact line
F_spAB=linspace(F_sp/3,(2/3)*F_sp,length(tetaAB));
F_spBC=(2/3)*F_sp*ones(1,length(tetaBC));
F_spCD=linspace((2/3)*F_sp,F_sp/3,length(tetaCD));
F_sp_lin=[F_spAB F_spBC F_spCD];

%%% RING-PLANET contact segment
% length of solar-satellite contact segments
s_cont_pr=Int*sin(alpha)+ sqrt((rtp^2)-(rbp^2)) - sqrt((rtr^2)-(rbr^2));
s_acc_pr=rbr*tan(alpha) - sqrt((rtr^2)-(rbr^2));
s_rec_pr=s_cont_pr - s_acc_pr;
teta_rif_A_pr=atan((rbp*tan(alpha) - s_acc_pr)/rbp);
teta_rif_B_pr=atan((rbp*tan(alpha) + s_rec_pr)/rbp);
teta_rif_pr=linspace(teta_rif_A_pr,teta_rif_B_pr,300);
ldc_length_deg_pr=teta_rif_pr(end)-teta_rif_pr(1);
N2B2=sqrt((rtr^2)-(rbr^2))-Int*sin(alpha);
pho1_pr=N2B2+rbp.*tan(teta_rif_pr);
pho2_pr=Int*sin(alpha)+pho1_pr;

%%% friction coefficient estimate ISO/TR 14179-2
% SOLAR-PLANET
sigma=(0.2+0.2)/(2*(10^6));
r_curv=1/((d_1st(1))/2) + 1/((d_1st(2))/2);
v_per=omega_s*(d_1st(1)/2);
v_sw=2*v_per*sin(alpha);

f_att2=0.48.*(((F_sp_lin./(b_1st./1000))./(v_sw.*r_curv)).^0.2).*((nu_din).^(-0.05))*(sigma.^0.25);

f_att_average=mean(f_att2);
% % PLANET-RING
r_curv_r=1/((d_1st(2))/2) - 1/((d_1st(3))/2);
v_per_r=omega_p*(d_1st(2)/2);
v_sw_r=2*v_per_r*sin(alpha);

f_att2_r=0.48.*(((F_rp./(b_1st./1000))./(v_sw_r.*r_curv_r)).^0.2).*((nu_din).^(-0.05))*(sigma.^0.25);
f_att_average_r=mean(f_att2_r);

%%% Friction and lubricating film
hmin_centro=((1/(d_1st(1)/2))+(1/(d_1st(2)/2))).*1.714.*(((F_sp./((b_1st).*((1/(d_1st(1)/2))+(1/(d_1st(2)/2))
).*1000.*(E_eq*10^3))).^-
0.128).*(((v_per.*1000.*nu_din_rif)./(((1/(d_1st(1)/2))+(1/(d_1st(2)/2))).*1000.*(E_eq*10^9))).^0.694).*((alp
ha_lub.*(E_eq*10^9)).^0.568)); %lubricant film thickness
a=((3.*F_sp_lin.*pho_eq)./(2*E_eq.*10^9)).^(1/3);
A_eff=2*a.*s_dente; %apparent contact area
P_0_vec=sqrt((F_sp_lin.*pho_eq.*(E_eq.*10^9))./(2*pi.*(s_dente))); %contact pressures

%% Second stage
%%% geometric data of the gear wheels
eps_sp_2st=1.49;                %  conduct report solar-planet 2st ATTENZIONE NEL SUO CASO ERANO UGUALI
eps_rp_2st=1.53;                %  conduct report ring-planet 2st
mn_2st = 1.5/1000;              %[m] normal module -2stage
z_2st = [60 30 120]';           % numeber of teeth solar-planet-ring - 2stage
d_2st=mn_2st.*z_2st;            %[m] pitch diameters  2stage
s_dente_2st=pi*mn_2st/2;        %[m] tooth thickness in the pitch circle 2stage
b_2st=30;                       %[mm] band width 2 stage
m_sol_2st=1.498;                %[kg] solar mass 2st
m_sat_2st=0.375;                %[kg] planet mass 2st
```

```
% % Wheelbase , base radii and head radii
Int_2st=((d_2st(1) + d_2st(2))/2);     %[m] wheelbase 2st
rbs_2st= 0.042;                        %[m] base radius solar gear 2st
rbp_2st= 0.021;                        %[m] base radius planet gear 2st
rbr_2st= 0.085;                        %[m] base radius ring 2st
rbc_2st=rbs_2st+rbp_2st;               %[m] "base radius" carrier 2st
rts_2st=(d_2st(1)/2)+mn_2st;           %[m] head radius solar 2st
rtp_2st=(d_2st(2)/2)+mn_2st;           %[m] head radius planet 2st
rtr_2st=(d_2st(3)/2)+0.25*mn_2st;      %[m] head radius ring 2st

%%% kinematics
% transmission reports
tau_rp_2st = z_2st(2)/z_2st(3);
tau_sp_2st = -(z_2st(1)/z_2st(2));
tau_2st = 1 + (z_2st(3)/z_2st(1));
% torque distribution-static analysis
T_s_2st= 144;                          % [Nm]
F_sp_2st=T_s_2st./(3*d_2st(1)*cos(alpha));
F_rp_2st=F_sp_2st;
% speed
n_in_2st=348;                         %[rpm]
omega_in_2st=(2*pi*n_in_2st)/60;    %[rad/s] solar shaft speed
omega_c_2st=omega_in_2st/tau_2st;   %[rad/s] carrier speed
omega_s_2st=omega_in_2st;           %[rad/s] solar speed
omega_p_2st=(omega_s_2st-omega_c_2st)*(z_2st(1)/z_2st(2));      %[rad/s] relative speed planet

%%% dynamic
% Moment of inertia
I_sol_2st=1.52e-3;  %[kg*m2] moment of inertia solar 2stage
I_sat_2st=9.48e-5;  %[kg*m2] moment of inertia planet 2 stage
I_car_2st=6.40e-3;  %[kg*m2] moment of inertia carrier 2 stage

%%% mesh stiffness- Kuang_Yang model
% solar-planet
R_sol_inf_2st=sqrt(((Int_2st*sin(alpha)) - sqrt((mn_2st + d_2st(2)/2)^2 -(((d_2st(2)/2)*cos(alpha))^2)))^2 +
((d_2st(1)/2)*cos(alpha))^2); %radial distance from the contact initiation points
A_2st=0;                              % start of the contact segment
B_2st=(eps_sp_2st-1)*2*pi/z_2st(1);
C_2st=2*pi/z_2st(1);
D_2st=eps_sp_2st*2*pi/z_2st(1);

% first stretch (two pairs of teeth in contact)
tetaAB_2st=linspace(A_2st,B_2st);              % mesh angle feed vector from A to B
% second stretch (a pair of teeth in contact)
tetaBC_2st=linspace(B_2st,C_2st);             % mesh angle feed vector from B to C
rBC_1_2st=sqrt((((d_2st(1)/2)*cos(alpha)).^2) + (sqrt((R_sol_inf_2st.^2)-(((d_2st(1)/2)*cos(alpha)).^2)) +
(d_2st(1)/2)*cos(alpha).*tetaBC_2st).^2);
rBC_2_2st=sqrt((((d_2st(2)/2)*cos(alpha)).^2) + ((Int_2st*sin(alpha) - sqrt(rBC_1_2st.^2 -
((d_2st(1)/2)*cos(alpha)).^2))).^2);
[KBC_sol_2st]=mesh_stiffness(mn_2st,z_2st(1),d_2st(1),rBC_1_2st,x_i);
[KBC_sat_2st]=mesh_stiffness(mn_2st,z_2st(2),d_2st(2),rBC_2_2st,x_i);
% third stretch (two pairs of teeth in contact)
tetaCD_2st=linspace(C_2st,D_2st)  ;            % mesh angle feed vector from C to D

% stiffness with a pair of teeth in contact (BC)
Keq_1cop_2st= (b_2st/1000).*((KBC_sol_2st.*KBC_sat_2st)./(KBC_sol_2st + KBC_sat_2st));

% planet-ring
R_sat_inf_2st=sqrt(((Int_2st*sin(alpha)) - sqrt((-mn_2st + (d_2st(3)/2))^2 -(((d_2st(3)/2)+
(1.25*mn_2st))^2))^2 + ((d_2st(2)/2)*cos(alpha))^2));
Apr_2st=0;                                          % start of the contact segment
Bpr_2st=(eps_rp_2st-1)*2*pi/z_2st(2);
Cpr_2st=2*pi/z_2st(2);
Dpr_2st=eps_rp_2st*2*pi/z_2st(2);
% second stretch (a pair of teeth in contact)
tetaBCpr_2st=linspace(Bpr_2st,Cpr_2st) ;                    % mesh angle feed vector from B to C
rBC_1_pr_2st=sqrt((((d_2st(2)/2)*cos(alpha)).^2) + (sqrt((R_sat_inf_2st.^2)-(((d_2st(2)/2)*cos(alpha)).^2)) +
(d_2st(2)/2)*cos(alpha).*tetaBCpr_2st).^2);
rBC_2_pr_2st=sqrt((((d_2st(3)/2)+ (1.25*mn_2st)).^2) + ((Int_2st*sin(alpha) - sqrt(rBC_1_pr_2st.^2 -
((d_2st(2)/2)*cos(alpha)).^2))).^2);
[KBC_sat_pr_2st]=mesh_stiffness(mn_2st,z_2st(2),d_2st(2),rBC_1_pr_2st,x_i);
[KBC_ring_pr_2st]=mesh_stiffness(mn_2st,z_2st(3),d_2st(3),rBC_2_pr_2st,x_i);
```

```
 % stiffness with a pair of teeth in contact (BC)
Keq_1cop_pr_2st= (b_2st/1000).*((KBC_sat_pr_2st.*KBC_ring_pr_2st)./(KBC_sat_pr_2st + KBC_ring_pr_2st));

 % constant stiffness and damping
Keq_1cop_const_2st=mean(Keq_1cop_2st);
Keq_1cop_const_pr_2st=-mean(Keq_1cop_pr_2st);
ksp_2st=(0.75*eps_sp_2st + 0.25)*Keq_1cop_const_2st*(b_2st/1000);
krp_2st=(0.75*eps_rp_2st + 0.25)*Keq_1cop_const_pr_2st*(b_2st/1000);
damp_ratio=(0.03+0.17)/2;

 % %Varying mesh stiffnesses over time
pb_2st=4.4;                                    %basic step 2 stage
psi_n_2st=pb_2st*(2*pi)/(z_2st(1)*z_2st(3));
gammasol_sat_2st=-(z_2st(1)/(2*pi))*psi_n_2st;
gammaring_sat_2st=(z_2st(3)/(2*pi))*psi_n_2st;

% speed loss coefficients
ks0 = 3.5E-10;                  % [Nms2/mm2rad2] speed loss parameter @40°C -10
ks_2st = ks0*K_ks;                  % [Nms2/mm2rad2]speed loss parameter
% cs coefficients computation
cs_2st= ks_2st*((((d_2st(1)*1000))^2+3*(z_2st(1)/z_2st(2))^3*((d_2st(2)*1000))^2);
% tare losses
ktl0 = 0.001;                % [Nm/mm] tare losses coefficient @40°C
TLPIF = 2.15;                % tare losses increase factor (breakout)
ktl_TLPIF = ktl0*TLPIF*K_ktlTLPIF; % tare losses coefficient breakout
TtlBO_2st = ktl_TLPIF*(((d_2st(1)*1000))+3*(z_2st(1)/z_2st(2))*((d_2st(2)*1000)));

Tfg_st_2st = TtlBO_2st;
c_g_2st = cs_2st;

% %% contact segment SOLAR-PLANET
% % length of solar-planet contact segments
s_acc_2st=sqrt((rtp_2st^2)-(rbp_2st^2)) - (d_2st(2)/2)*sin(alpha);
s_rec_2st=sqrt((rts_2st^2)-(rbs_2st^2)) - (d_2st(1)/2)*sin(alpha);
s_base_2st=(rbs_2st+rbp_2st)*tan(alpha);

teta_rif_A_2st=atan((rbs_2st*tan(alpha) - s_acc_2st)/rbs_2st);
teta_rif_B_2st=atan((rbs_2st*tan(alpha) + s_rec_2st)/rbs_2st);
teta_rif_2st=linspace(teta_rif_A_2st,teta_rif_B_2st,300);
ldc_length_deg_2st=teta_rif_2st(end)-teta_rif_2st(1);      % the rotation of the solar corresponding to the
total length of the segment of the path contacts
pho1_2st=rbs_2st.*tan(teta_rif_2st);         % [m] radii of the equivalent circles
pho2_2st=s_base_2st-pho1_2st;
pho_eq_2st=(pho1_2st.*pho2_2st)./(pho1_2st+pho2_2st);

%% load splitting along the contact line
F_spAB_2st=linspace(F_sp_2st/3,(2/3)*F_sp_2st,length(tetaAB_2st));
F_spBC_2st=(2/3)*F_sp_2st*ones(1,length(tetaBC_2st));
F_spCD_2st=linspace((2/3)*F_sp_2st,F_sp_2st/3,length(tetaCD_2st));
F_sp_lin_2st=[F_spAB_2st F_spBC_2st F_spCD_2st];


%%% RING-PLANET contact segment
% length of solar-satellite contact segments
s_cont_pr_2st=Int_2st*sin(alpha)+ sqrt((rtp_2st^2)-(rbp_2st^2)) - sqrt((rtr_2st^2)-(rbr_2st^2));
s_acc_pr_2st=rbr_2st*tan(alpha) - sqrt((rtr_2st^2)-(rbr_2st^2));
s_rec_pr_2st=s_cont_pr_2st - s_acc_pr_2st;
teta_rif_A_pr_2st=atan((rbp_2st*tan(alpha) - s_acc_pr_2st)/rbp_2st);
teta_rif_B_pr_2st=atan((rbp_2st*tan(alpha) + s_rec_pr_2st)/rbp_2st);
teta_rif_pr_2st=linspace(teta_rif_A_pr_2st,teta_rif_B_pr_2st,300);
ldc_length_deg_pr_2st=teta_rif_pr_2st(end)-teta_rif_pr_2st(1);
N2B2_2st=sqrt((rtr_2st^2)-(rbr_2st^2))-Int_2st*sin(alpha);
pho1_pr_2st=N2B2_2st+rbp_2st.*tan(teta_rif_pr_2st);
pho2_pr_2st=Int_2st*sin(alpha)+pho1_pr_2st;

%%% friction coefficient estimate ISO/TR 14179-2
% SOLAR-PLANET
sigma=(0.2+0.2)/(2*(10^6));
r_curv_2st=1/((d_2st(1))/2) + 1/((d_2st(2))/2);
v_per_2st=omega_s_2st*(d_2st(1)/2);
v_sw_2st=2*v_per_2st*sin(alpha);

f_att2_2st=0.48.*(((F_sp_lin_2st./(b_2st./1000))./(v_sw_2st.*r_curv_2st)).^0.2).*((nu_din).^(-
0.05))*(sigma.^0.25);
f_att_average_2st=mean(f_att2_2st);
```

```
%%% PLANET-RING
r_curv_r_2st=1/((d_2st(2))/2) - 1/((d_2st(3))/2);
v_per_r_2st=omega_p_2st*(d_2st(2)/2);
v_sw_r_2st=2*v_per_r_2st*sin(alpha);

f_att2_r_2st=0.48.*(((F_rp_2st./(b_2st./1000))./(v_sw_r_2st.*r_curv_r_2st)).^0.2).*((nu_din).^(-
0.05))*(sigma.^0.25);
f_att_average_r_2st=mean(f_att2_r_2st);

%%% Friction and lubricating film
hmin_centro_2st=((1/(d_2st(1)/2))+(1/(d_2st(2)/2))).*1.714.*(((F_sp_2st./((b_2st).*((1/(d_2st(1)/2))+(1/(d_2s
t(2)/2))).*1000.*(E_eq*10^3))).^-
0.128).*(((v_per_2st.*1000.*nu_din_rif)./(((1/(d_2st(1)/2))+(1/(d_2st(2)/2))).*1000.*(E_eq*10^9))).^0.694).*(
(alpha_lub.*(E_eq*10^9)).^0.568)); %lubricant film thickness
a_2st=((3.*F_sp_lin_2st.*pho_eq_2st)./(2*E_eq.*10^9)).^(1/3);
A_eff_2st=2*a_2st.*s_dente_2st; %apparent contact area
P_0_vec_2st=sqrt((F_sp_lin_2st.*pho_eq_2st.*(E_eq.*10^9))./(2*pi.*(s_dente_2st))); %contact pressures


%% ************************* ELECTRIC MOTOR DATA **********************************
%%% electrical data
Zp_RH_WT = 5;%10;                          % [-] number of poles couples
R_RH_WT = 0.94;                            % [Ohm] Phase resistance
L_RH_WT = 0.0038;                          % [H] Phase inductance (both mutual and not)
RR_RH_WT=1e6;                              % [Ohm] insulation resistance IPOTESI
LR_RH_WT= L_RH_WT/10;                      % [H] insulation inductance IPOTESI
RG_RH_WT=1e6;                              % [Ohm] grounded resistance IPOTESI
LG_RH_WT= L_RH_WT/10;                      % [H] grounded inductance IPOTESI
k_t_RH_WT = 0.661*sqrt(2);                 % [Nm/A] torque constant on Iq
k_e_RH_WT = 40/(1000*pi/30)/sqrt(3);       % [Vs/rad] speed constant (single phase)
imax_RH_WT = 9.56*sqrt(2);                 % [A] maximum allowed current
Trifw = 20;                                % [°C] Reference temperature for R,L dependencies on T
alpha_Tw_R_RH_WT = 0;%0.00393;             % [1/°C] Resistance variation on temperature
alpha_Tw_L_RH_WT = 0;                      % [1/°C] Resistance variation on flux linkage, se si vuole inserire
bisgona tener conto di una variaizione che sia piccola (es: del 10% tra -54 e 40)

%%% mechanical data
Tfm_st_RH_WT = 0.165;                % [Nm] Breakout torque
c_m0 = 1.89*10^(-4);                   % [Nms/rad] viscous friction coefficent @40°C
Jm_RH_WT = 0.00024;                  % [kgm2] Rotor inertia
w_max = 6000*pi/30;                      % [rad/s] maximum mechanical speed


%%% thermal data
m_em=3.72;                              %[kg]frameless motor mass
Cth_w_RH_WT =387*m_em ;                 % [J/K] windings thermal capacity   (calore specifico del rame per la
massa frameless)
Cth_housing_RH_WT =880*m_em/3;          % [J/K] housing thermal capacity    (calore specifico alluminio per la
massa dell'alloggiamento ipotizzata 1/3 della massa del motore)
Hth_w_RH_WT =1/0.56; % Cth_w_RH_WT/50.66;       % [W/K] motor thermal conductance windings-housing   ??
Hth_housing_RH_WT =1/0.09; % Hth_w_RH_WT/5;     % [W/K] motor thermal conductance housing-ext      ??

%%************************* ELECTRONIC POWER UNIT DATA ***************************
%%% EPU data
f_switch_RH_WT = 16;                          % [kHz] switch frequency
T_switch_RH_WT = 1/(f_switch_RH_WT*1000);       % [s] switch time (PWM)

%%% Supply data
VDCL=240*3/2; %360;  % [V] the DC-link voltage $Vdclink$, supplied as a constant value and equal to 3/2 the
motor voltage chosen

%% ************************ SAMPLING SYSTEM/CONTROL DATA ***************************
%%% Acquisition system data
Vel_RH_WT = 20;                            % [V] Voltage tension range
n_bit_RH_WT = 14;                          % [-] bit number
Tsampl_pos_RH_WT = 1/1000;                 % [s] sampling period for position control
Tsampl_w_RH_WT = 1/4000;                   % [s] sampling period for speed control
Tsampl_f_RH_WT = Tsampl_w_RH_WT;                % [s] sampling period for force-fighting compensator
%%% Microprocessor data
Tc_pos_RH_WT = 0.0002;          % [s] position loop refresh and computation time
Tc_w_RH_WT = 0.00001;           % [s] speed loop refresh and computation time
Tc_f_RH_WT = Tc_w_RH_WT;
```

```
%% ************************* SENSOR/TRANSDUCERS DATA ******************************
%%% Current measure filter
Hi_RH_WT = 1;                                    % [A/A] filter gain
tau_i_RH_WT =4/(f_switch_RH_WT*2*pi*1000);   % [s/rad] filter time constant

%%% RVDT parameters
Hrvdt_RH_WT = 0.705;                    % [Vrms/rad] RVDT gain
Vrvdt_endstop = 0.261;                  % [Vrms] Output voltage
S_rvdt_RH_WT = 1257;                    % [rad/s] filter natural frequency
zeta_rvdt_RH_WT = 1;                    % [-] damping coefficient for RVDT


%%% resolver parameters
Hres_RH_WT = 1;                                % [Vrms*s/rad] resolver gain
S_res_RH_WT = w_max*Zp_RH_WT*100;              % [rad/s] filter natural frequency
zeta_res_RH_WT = 1;                            % [-] damping coefficient for resolver


%% ###########################################################################################
%************************** CONTROL LOOPS GAINS ***********************************#
%###########################################################################################
%%% current loop
Kp_id_RH_WT = 5000;%0.900;
Ki_id_RH_WT = 1000;%0;
Kp_iq_RH_WT = 5000;%0.900;
Ki_iq_RH_WT = 1000;0;

%%% speed loop
kp_w_RH_WT = 40;%0.46;
ki_w_RH_WT = 15;%12;


%%% position loop
kp_p_RH_WT = 4000;
ki_p_RH_WT = 25;


T_EXT = Trif;
T_0_RH_WT = T_EXT;
```

# Bibliography


[1] Roger W. Pratt. «Flight Control Systems - Practical Issues in Design and implementation-IET». In: (2000), p. 4 (cit. on pp. 2, 6, 7).

[2] I. Moir and A. Seabridge. *Aircraft Systems: Mechanical, electrical and avionics subsystems integration*. Ed. by John Wiley Sons. Third. 2008 (cit. on pp. 2, 12).

[3] Guan Qiao- Geng Liu- Zhenghong Shi Yawen Wang- Shangjun Ma and Teik C Lim. «A review of electromechanical actuators for More/All Electric aircraft systems». In: *J Mechanical Engineering Science* 232 (2018), pp. 4128–4151 (cit. on p. 10).

[4] *Catalogue-EN-2018-Rollvis SA [online]*. URL: `http://rollvis.com/wp-content/uploads/2021/09/Catalogue-EN-2018-compressed.pdf` (cit. on pp. 20, 23).

[5] *Thrust ball bearings SKF [online]*. URL: `https://www.skf.com/it/products/rolling-bearings/ball-bearings/thrust-ball-bearings/productid-51205` (cit. on p. 25).

[6] *Kollmorgen. KBM Series Brushless Motors – Selection Guide. [online]*. URL: `https://www.kollmorgen.com/sites/default/files/public_downloads/kbm_e.pdf` (cit. on pp. 40–42).

[7] *Brushless resolvers(Smartsyn)/ R/D converters (Smartcoder) catalog - TAMAGA SEIKI CO, LTD*. URL: `https://www.tamagawa-seiki.com/products/resolver-synchro/brushless-resolver-smartsyn-builtin.html` (cit. on pp. 43, 44).

[8] *R30A-AC Operated, Light Weight RVDT- Althen Sebsors*. URL: `https://www.althensensors.com/media/25708/r30a-rvdt-en.pdf` (cit. on pp. 45, 46).

[9] Bertolino A. De Martin A. Nesci A.and Sorli M. *Meccatronica: Analisi, progettazione e modellazione di servosistemi*. Ed. by CLUT. 2021 (cit. on pp. 67, 94, 97).

[10] F. Sulaiman E. Amin and Soomro H.A. «Field oriented control principles for synchronous motor.» In: *International Journal of Mechanical Engineering and Robotics Research* 8 (2019), pp. 284–288 (cit. on p. 92).

[11] Fan L. Wang S. Wang X. Han F. Lyu H. «Nonlinear dynamic modeling of a helicopter planetary gear train for carrier plate crack fault diagnosis.» In: *Chinese Journal of Aeronautics* (2016) (cit. on p. 108).